Dalton Transactions

ARTICLE

Highly Luminescent 2-Phenylpyridine-Free Diiridium Complexes with Bulky 1,2-Diarylimidazole Cyclometalating Ligands

Received 00th January 20xx,
Accepted 00th January 20xx

DOI: 10.1039/x0xx00000x

www.rsc.org/

Daniel G. Congrave*, Andrei S. Batsanov and Martin R. Bryce*

While a number of highly emissive dinuclear Ir(III) complexes have been reported, they have generally been restricted to structures based on 2-phenylpyridine (Hppy) cyclometalates. We now present a series of new hydrazide-bridged diiridium complexes (**5**–**8**) which incorporate bulky 1,2-diarylimidazole cyclometalating ligands in the place of Hppy. Complexes **6**–**8** are strongly emissive when doped into poly(methyl methacrylate) (PMMA), displaying the highest PLQYs yet reported for ppy-free diiridium emitters (Φ_{PL} = 47–55 ± 10%). Notably, complex **8** has an emission peak at 452 nm and CIE_{xy} colour coordinates in the sky-blue region (0.18, 0.27), which is competitive with state-of-the-art monoiridium analogues**.** X-ray crystallography and solution-state ^{19}F NMR spectra reveal the presence of rigidifying intramolecular π–π interactions for complexes **6**–**8**, which explains their improved photophysical performance compared to **5** which does not have these interactions. Structure-property relationships are further rationalised through density functional theory (DFT) and cyclic voltammetry (CV) data. All the complexes studied in this work display aggregation induced phosphorescent emission (AIPE). This series of compounds increases the structural diversity of highly luminescent dinuclear Ir(III) complexes to include luminophoric ligands that are not restricted to Hppy-type fragments. The colour range accessible to AIPE-active diiridum complexes has also been substantially broadened.

Introduction

Iridium(III) complexes have been extensively studied over the last 30 years.[1] The metal-ligand based photochemistry has enabled their emission colour to be tuned across the entire visible spectrum through modular synthesis.[2] They typically feature high luminescence quantum efficiencies (Φ), microsecond-scale phosphorescence lifetimes (τ) and good electrochemical stabilities. These properties are advantageous for applications[3] such as photocatalysis,[4] biological labelling,[5] sensing,[6] and phosphorescent organic light-emitting devices (PhOLEDs)[7,8]

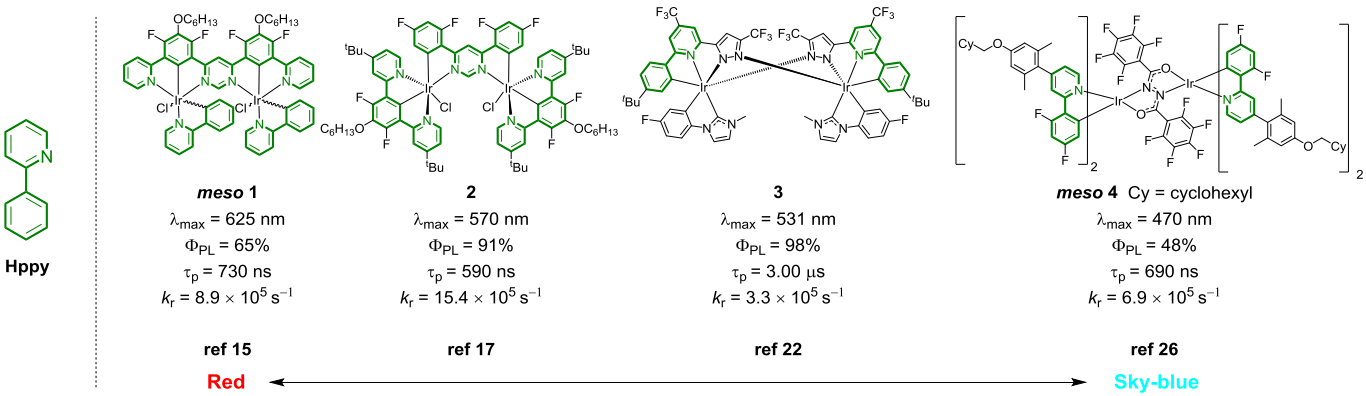

Figure 1. Representative highly emissive diiridium complexes containing 2-phenylpyridine (Hppy) fragments with selected solution photoluminescence parameters (all obtained in degassed DCM). 2-Phenylpyridine fragments are highlighted in green.

Interest in phosphorescent dinuclear Ir(III) complexes has recently increased. Unlike their mononuclear analogues, they feature ligands which bridge the two metal centres. A wide variety of bridging ligands has been explored, and they can heavily influence the photophysical properties of the complexes.[9–22] For example, flexible bridges impart aggregation-induced phosphorescent emission (AIPE) to

Department of Chemistry, Durham University, South Road, Durham DH1 3LE, UK.
Electronic Supplementary Information (ESI) available: synthetic details, NMR spectra, X-ray data (CCDC 1871136 for **7**, and CCDC 1871137 for **8**), electrochemistry, thermal gravimetric analysis; computations and photophysics.

Please do not adjust margins

orange/ red-emitting complexes,[14] which have been employed in sensing applications.[23,24] Complementarily, bridging ligands can lead to rigid complexes, either covalently through the incorporation of rigid polyaromatic structures (complexes **1**, **2** and **3**, Figure 1),[15,17,18,22,25] or non-covalently through promoting intramolecular perfluoroaryl-aryl π–π interactions with peripheral ligands (complex **4**, Figure 1).[26] This has allowed the development of diiridium complexes that exhibit high solution photoluminescence quantum yields (PLQYs) (> *ca.* 50%) from the red to the sky-blue regions of the visible spectrum (e.g. complexes **1**–**4**). Diiridium complexes have also demonstrated advantages over their mononuclear counterparts. For example, sub-microsecond phosphorescence lifetimes are obtained alongside high PLQYs (complexes **1** and **2**) due to high radiative rate constants (k_r), which is likely due to an improved spin-orbit coupling (SOC) effect exerted by two proximal heavy metal atoms.[15,17,25] Chang and co-workers have also recently reported sky-blue diiridium phosphors with unity PLQY that are sublimable.[22]

2-Phenylpyridine (Hppy)-based cyclometalating ligands (Figure 1) are popular for Ir(III) phosphors due to their synthetic versatility, well-understood structure-property relationships, and because they reliably afford complexes with high PLQYs.[27–29] Consequently, Hppy-type fragments that form 5-membered cyclometalates have been incorporated into the bridging or peripheral ligands of almost all the significantly emissive diiridium complexes (PLQY > *ca.* 30%) reported in the literature (e.g. complexes **1**–**4**).[8,9,14,16,18,20,23,25] In contrast, non-Hppy components have been seldom explored in diiridium complexes. We know of only a single structural type that does not contain a Hppy fragment and is significantly emissive at room temperature: namely, cationic AIPE complexes featuring 2-(phenyl)pyrazole (Hppz) cyclometalating ligands which exhibit orange/ red emission with PLQYs ≤ 31%.[23,31] This lack of structural diversity is restrictive, especially considering that Hppy-based cyclometalating ligands have some drawbacks. For example, the synthesis of Hppy-based ligands often requires expensive transition metal-catalysed routes.[32] Also Hppy-derived sky-blue/ blue emissive Ir(III) complexes suffer from poor excited state stability, particularly under PhOLED operation.[27]

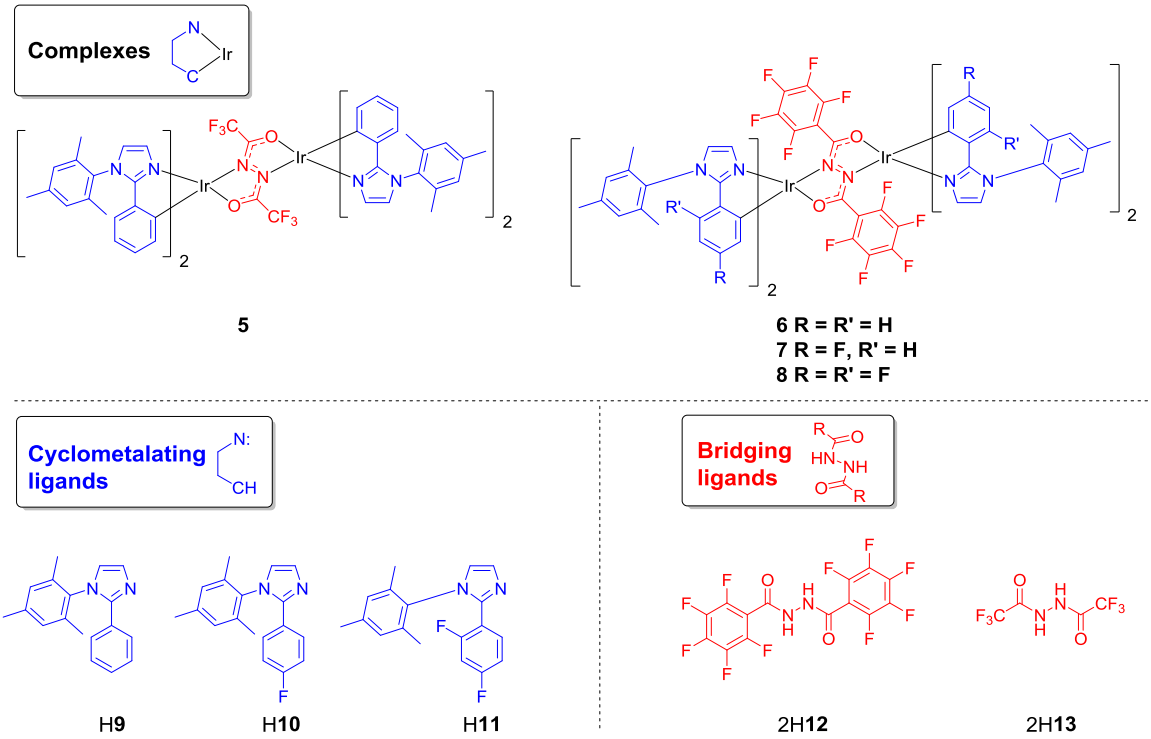

Figure 2. Structures of the complexes and ligands studied in this work.

Bulky 1,2-diarylimidazole ligands which form 5-membered cyclometalates are very topical as they have afforded highly emissive sky-blue mononuclear Ir(III) complexes that are notably more stable under PhOLED operating conditions than Hppy-functionalised analogues.[27,30,33–38] They have also been incorporated into heteroleptic mononuclear Ir(III) complexes that show promising preferential dipole alignment in solution-processed films.[30] Beneficially, 1,2-diarylimidazole ligands can also be synthesised from readily available starting materials through condensation chemistry, avoiding transition metal catalysis.[39] Despite this promise, while 1,2-diarylimidazoles have been studied as cyclometalating ligands in homo- and heteroleptic monoiridium complexes,[38,40–42] to the best of our knowledge they have not previously been applied to phosphorescent diiridium systems.

The aim of the present work is to diversify phosphorescent dinuclear Ir(III) complexes to include structures that are not restricted to Hppy-based ligands. We present a series of new diiridium complexes (**5**–**8**) (Figure 2) which feature bulky 1,2-diarylimidazole cyclometalating ligands alongside hydrazide

bridging ligands. Density functional theory (DFT) calculations, X-ray crystallography and electrochemical data provide further insight into their structural and optoelectronic properties.

Results and discussion

Design, synthesis and characterisation

The structures of the complexes **5**–**8** are shown in Figure 2. The complexes are of the formula $[(Ir(C^N)_2)_2(O^N^N^O)]$ with C^N = **9**–**11** and O^N^N^O = **12** and **13**. The conjugate acids of the ligands in the complexes (H**9**–H**11** and 2H**12** and 2H**13**) are also shown in Figure 2. The mesityl-functionalised 1,2-diarylimidazole cyclometalating ligand H**9** was selected due to the favourable photophysical properties of its homoleptic complex,[30,34] and because the steric bulk of the mesityl group should impart solubility and rigidity without inhibiting the formation of the complexes **5**–**8.** The bridging ligands 2H**12** and 2H**13** were employed in complexes **5** and **6** to target sky-blue emission and study the effect of intramolecular π–π stacking between the perfluoroaryl groups of **12** and the peripheral cyclometalating ligands.[26] Due to the enhanced photophysical performance of **6** compared to **5** (discussed below) the perfluoroaryl bridge 2H**12** was incorporated into complexes **7** and **8**, where incremental fluorination of their cyclometalating ligands (H**10** and H**11**) blue shifts their emission through HOMO stabilisation.

The bridging ligands 2H**12** and 2H**13** were synthesised as reported.[26] The cyclometalating ligands H**9**–H**11** were accessible on a multi-gram scale following Strassner's one-pot transition metal-free procedure.[39] The diiridium complexes **5**–**8** were then synthesised by cleaving the corresponding μ-Cl dimers with the bridging ligands 2H**12** or 2H**13** under basic conditions.[12,13,19,26] Complexes **6**–**8** were obtained in ≥ *ca.* 50% yields as diastereomeric mixtures which were not separated, apart from complex **5**, which was isolated as a single diastereomer. This follows literature precedent, where incorporation of the bis-trifluoromethyl bridge 2H**13** affords diastereoselectivity.[26]

Complexes **5**–**8** show good thermal stability with decomposition temperatures (T_d corresponding to 5% weight loss) of > 400 °C by thermal gravimetric analysis (TGA) (Figures S6–S9).

Expansions of the C_6F_5 regions of the ^{19}F $\{^1H\}$ NMR spectra of complexes **6**–**8** are shown in Figure 3.

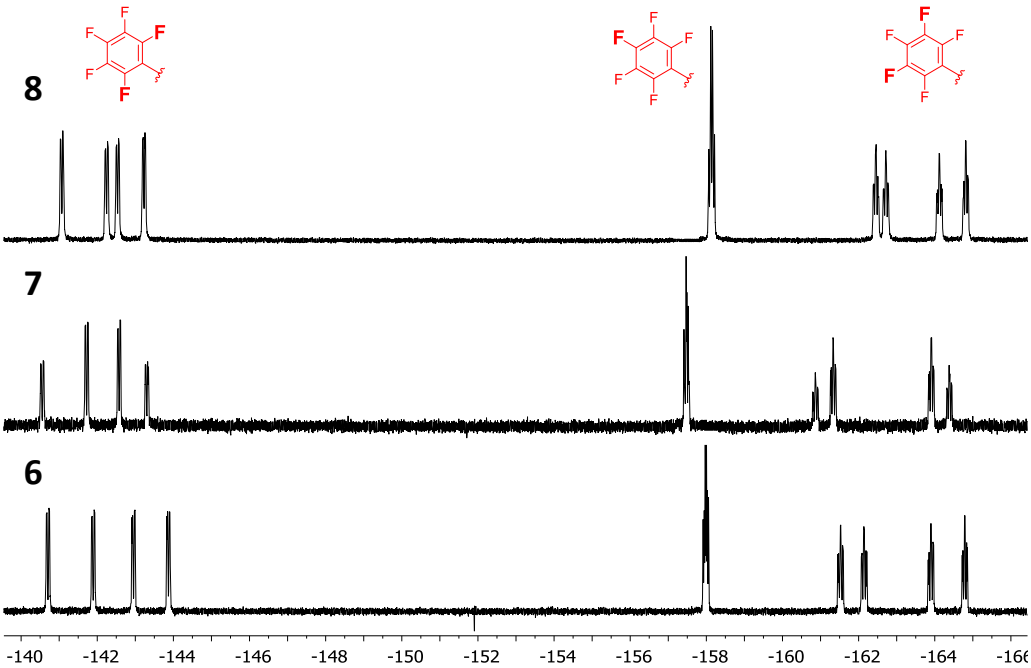

Figure 3. Expansions of the C_6F_5 regions of the 376 MHz ^{19}F $\{^1H\}$ spectra of **6**–**8** recorded in $CDCl_3$ at 298 K. Diastereomeric ratios from integration: **6** *ca.* 1:1, **7** *ca.* 1:0.6, **8** *ca.* 1:0.9.

The ^{19}F NMR spectra for the diastereomeric mixtures of **6**–**8** each display 10 environments in the C_6F_5 region (5 per diastereoisomer). This is greater than the 6 environments that would be expected (3 per diastereoisomer) for mono-substituted perfluorophenyl groups, and is due to a lowering of molecular symmetry. This is ascribed to restriction of rotation of the bridge C_6F_5 groups due to intramolecular π–π interactions with peripheral cyclometalating ligands (seen in the solid state for **7** and **8** in the X-ray diffraction data below).[26,43]

X-ray crystal structures

The single-crystal X-ray crystal structures of the *meso* diastereomers of **7** and **8** are displayed in Figure 4. Relevant parameters are listed in Table 1. Presumably, the *meso* diastereomers preferentially crystallised from solutions of diastereomeric mixtures due to their inversion centre

symmetry. *Meso* **7** crystallised as a DCM hexasolvate whereas *meso* **8** crystallised as a MeOH disolvate.

Table 1. Selected geometrical parameters of **7** and **8** (bond distances in Å).

	meso **7** •6CH_2Cl_2	*meso* **8** •2MeOH
Space group	*C2/c*	*Pbca*
Mol. symmetry	C_i	C_i
Ir centres	ΔΛ	ΔΛ
Ir---Ir, Å	5.022	5.065
Ir–C (*trans*-O)	2.003(4)	2.003(3)
Ir–C (*trans*-N)	2.012(4)	2.016(3)
Ir–N, stacked	2.020(3)	2.018(2)
Ir–N, non-stacked	2.019(3)	2.040(2)
Bridge geometry		
OCNNCO folding, °	planar	planar
Ir displacement, Å	0.086	0.208
Ir–O	2.119(3)	2.130(2)
Ir–N	2.144(3)	2.159(2)
N–N	1.434(4)	1.437(3)
N–C	1.306(6)	1.305(4)
C–O	1.279(4)	1.287(3)
Intramolecular stacking (π–π)		
Θ, °[a]	3.5	3.0
D, Å[b]	3.30	3.26
Centroid–centroid, Å	3.35	3.41

[a] Interplanar angle between ring *A* of the bridging ligand and ring *B* of the cyclometalating ligand (see Figure 4); [b] distance between the plane of ring *B* and the centroid of ring *A*.

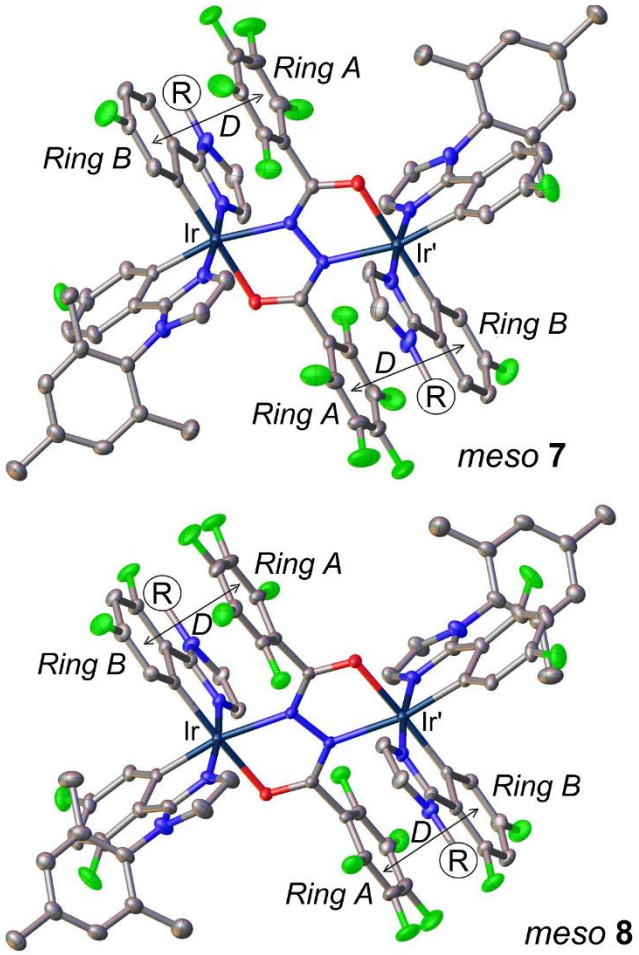

Figure 4. X-ray molecular structures of *meso* **7** and *meso* **8**. R = mesityl. Thermal ellipsoids are drawn at the 50% probability level, H atoms, solvent of crystallisation and some mesityl groups are omitted for clarity. Primed atoms are generated by a crystallographic inversion centre. Vector *D* identifies intramolecular π–π interactions (see Table 1).

The Ir centres in both structures display distorted octahedral coordination. The N atoms of the two C^N cyclometalating ligands occupy axial positions with respect to the bridge plane, and are *trans* to one another.[8,12] The central hydrazide moieties of *meso* **7** and *meso* **8** are planar, and the aryl substituents (*A*) on the bridging ligands are oriented approximately perpendicular to the hydrazide planes and are stacked face-to-face (π–π) with the phenyl ring (*B*) of a cyclometalating ligand (Figure 4). The stacking is closer and more parallel in *meso* **8** compared to *meso* **7** (*Θ* = 3.0 vs. 3.5° Θ *D* = 3.26 vs. 3.30 Å). However, the slightly larger centroid–centroid distance for *meso* **8** (3.41 Å vs. 3.35 Å for *meso* **7**) indicates greater slippage of the stacked rings.

Electrochemical study

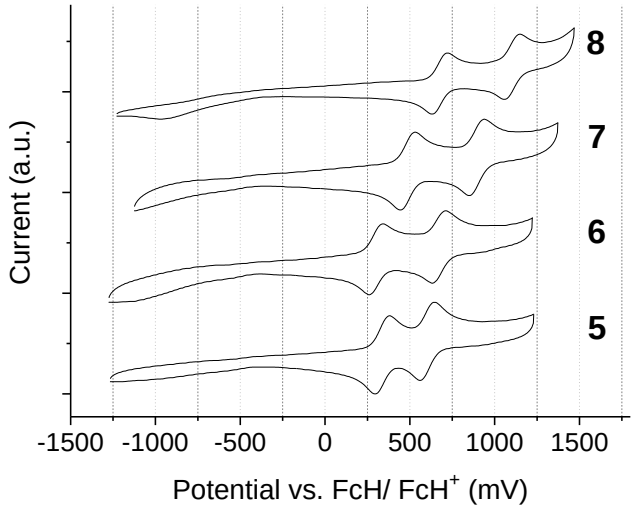

Figure 5. Cyclic voltammograms in 0.1 M *n*-Bu_4NPF_6/ DCM showing the oxidation processes for complexes **5**–**8**. The current range for each voltammogram is 10 – −10 μA.

Table 2. Electrochemical data for complexes **5–8** referenced to $E_{1/2}$ FcH/FcH^+ = 0.00 V.

Complex	$E^{ox(1)}$ /V E_{pa}/E_{pc} [$E_{1/2}$]	$E^{ox(2)}$ /V E_{pa}/E_{pc} [$E_{1/2}$]	$\Delta E_{1/2}$ /V[a]	E^{red}_{onset} /V[b]	HOMO /eV[c]	LUMO /eV[d]
5	0.38/ 0.29 [0.34]	0.65/ 0.55 [0.60]	0.26	–2.82	–5.14	–1.98
6	0.33/ 0.24 [0.30]	0.73/ 0.62 [0.67]	0.37	–2.95	–5.10	–1.85
7	0.55/ 0.43 [0.49]	0.95/ 0.84 [0.89]	0.40	–2.89	–5.29	–1.91
8	0.72/ 0.63 [0.68]	1.18/ 1.05 [1.12]	0.44	–2.76	–5.48	–2.04

[a]Peak splitting between $E^{ox(1)}$ and $E^{ox(2)}$. [b]All reductions are electrochemically irreversible. [c]HOMO levels calculated from CV potentials by HOMO = –4.8 + ($-E_{1/2}^{ox(1)}$), using ferrocene as the standard. [d]LUMO levels calculated from CV potentials by LUMO = –4.8 + ($-E^{red}_{onset}$), using ferrocene as the standard.

The oxidation and reduction processes for **5–8** were studied by cyclic voltammetry (CV). The data are listed in Table 2. The oxidative waves are presented in Figure 5 and the reductive processes are included in Figure S1. All complexes display two oxidation waves.

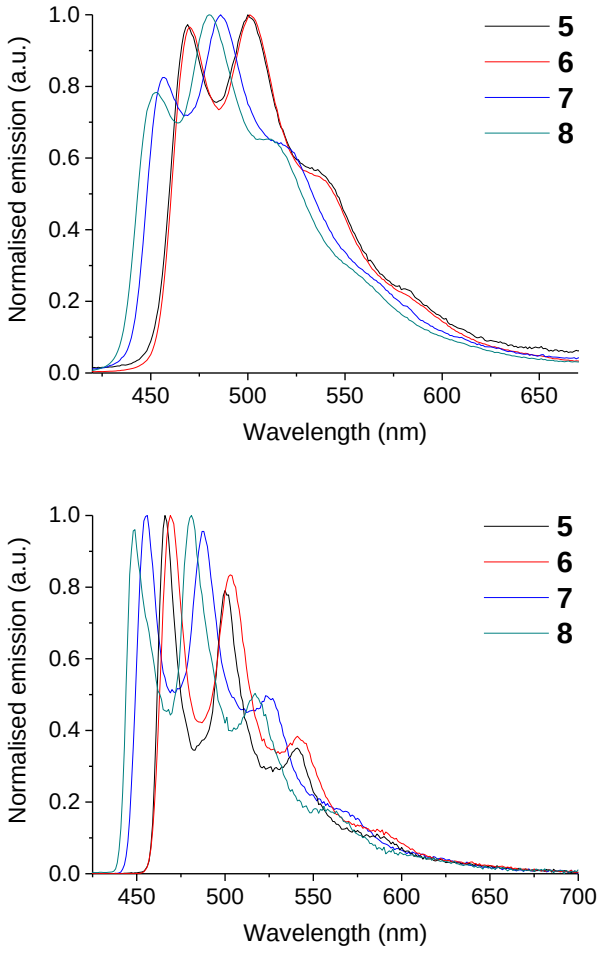

Figure 6. Emission spectra for complexes **5–8**. (Top) spectra of complexes doped into PMMA at 1 wt.% at room temperature. (Bottom) spectra of complexes in 2-MeTHF glasses at 77 K (λ_{exc} 355 nm).

They are assigned to sequential Ir^{3+}/Ir^{4+} redox couples and are indicative of electronic communication between the two centres. Both oxidations are electrochemically reversible for **5–8** based on the equal magnitudes of the coupled oxidation and reduction peaks. All reduction processes are electrochemical irreversible.

The first oxidation potential of **5** is more positive than for **6** (by 0.04 V). This suggests that the complexed bis(trifluoromethyl) bridge 2H**13** is more electron withdrawing than the bis(pentafluorophenyl) bridge 2H**12**.[44] Sequential fluorination of the cyclometalating ligands in **6–8** leads to successive increases in the first oxidation potentials, as expected. The peak splitting between the first and second oxidations ($\Delta E_{1/2}$) for the series **6–8** also increases incrementally, suggesting that the bridge HOMO contribution increases along the series. Complex **5** displays the lowest $\Delta E_{1/2}$. This is because the complexed bridge 2H**13** has a shorter conjugation length than 2H**12** and therefore is expected to feature a larger energy gap, decreasing its contribution to the HOMO of **5**. These conclusions are corroborated by the DFT data below.

The reduction onsets for **5–8** are comparable to the values for heteroleptic mononuclear complexes functionalised with 2-arylimidazole ligands.[41] While the irreversible nature of the reductions hinders their accurate determination, there are two clear qualitative trends in the data. (i) The reduction potential for **5** is less negative than for **6**, i.e. **5** is easier to reduce, in-line with the more electron-withdrawing complexed bridge 2H**13** and the higher first oxidation potential of **5**. (ii) Sequential fluorination in the series **6–8** leads to consecutively less negative reduction potentials as the complexes become more electron poor. However, the LUMO energies do not drop as significantly as the HOMO energies upon fluorination, leading to sequentially larger electrochemical bandgaps in the order **6** < **7** < **8**.

Photophysical properties

Table 3. Summary of the key photoluminescence data for complexes **5–8**.

	Doped into PMMA 1% wt.[a]					2-MeTHF glass[b]	
Complex	$\lambda_{max\ em}$ /nm [CIE_{xy}]	PLQY /% (± 10%)	τ /µs	k_r /× 10^5 s^{-1}	k_{nr} /× 10^5 s^{-1}	$\lambda_{max\ em}$ /nm ($\lambda_{10\%\ em}$ /nm)[c] [E_T /eV][d]	τ /µs
5	469sh, 500 [0.20, 0.40]	11	1.82	0.60	4.89	466 (458) [2.71]	3.88
6	470sh, 501 [0.20, 0.39]	55	2.80	1.96	1.61	469 (459) [2.70]	4.02
7	456sh, 486 [0.18, 0.31]	47	4.15	1.13	1.28	456 (442) [2.81]	5.35
8	452sh,	52	4.55	1.14	1.05	449sh, 480	5.21

	480 [0.18, 0.27]	(440) [2.82]

sh = Shoulder. [a]Measured in an integrating sphere under air using an excitation wavelength of 355 nm. [b]Measured at 77 K using an excitation wavelength of 355 nm. [c]Wavelength at 10% intensity on the blue edge of the spectrum obtained at 77 K. [d]Estimated using $E_T = hc/\lambda_{10\%\ em}$. $\tau = 1/k_{nr} + k_r$.

The absorption spectra of **5**–**8** are shown in Figure S2 and the data are listed in Table S1. The spectra display features typical of cyclometalated iridium complexes: There are intense bands below *ca.* 300 nm which correspond to population of LC states, while the weaker bands extending to *ca.* 450 nm are assigned to ^{1}MLCT and ^{3}MLCT transitions.[45,46] The extinction coefficients are higher than for similar mononuclear 2-phenylimidazole complexes,[41] ascribed to a larger number of cyclometalating ligands and Ir atoms per complex. An increase in the intensity of the ^{3}MLCT bands compared to mononuclear analogues may be due to improved spin-orbit coupling in dinuclear complexes.[15,17]

The emission spectra for **5**–**8** doped into poly(methyl methacrylate) (PMMA) at room temperature, and in 2-MeTHF at 77 K are shown in Figure 6. Photoluminescence data are tabulated in Table 3. Complexes **5**–**8** are non-emissive in DCM solution at room temperature with PLQYs ≤ 0.05%. In contrast, they are emissive (PLQY = 11–55 ± 10%) in the blue-green/ sky-blue regions at room temperature in dilute PMMA films (1 wt% complex). To the best of our knowledge, complexes **6**–**8** exhibit the highest PLQYs yet reported for ppy-free diiridium complexes (PLQY = 47–55 ± 10%).[23,31] Sequential fluorination of the cyclometalating ligands in the series **6**–**8** leads to incremental blue shifts in their emission, as expected. We note that complex **8** has an emission peak (452 nm) and CIE_{xy} coordinates (0.18, 0.27) that are competitive with the bluest monoiridium analogues that contain arylimidazole ligands.[35,38] The comparatively broad emission of **5**–**8** is reminiscent of mononuclear analogues.[27,30,33–38] While we cannot completely disregard any effects of diastereomeric mixtures on the optoelectronic properties of **6**–**8**, there are literature precedents that diiridium diastereomers display very similar photophysical properties.[15,25]

The matrix-dependent emission properties of **5**–**8** are ascribed to non-radiative emission quenching in solution. As this is suppressed in a PMMA matrix, it is evident that the dominant pathway for non-radiative decay in solution likely involves significant molecular motion, rather than any other process, for example C–C bond stretching.[47] There are examples of homo- and heteroleptic monoiridium complexes functionalised with bulky 1,2-diarylimidazole ligands that are highly emissive in solution,[34,37,41] which indicates that the bridging ligands of **5**–**8** are likely to be the structural feature responsible for their non-emissive behaviour in solution. Therefore, we conclude that non-radiative decay through motion of the bridging ligand is responsible for the quenching of solution phosphorescence, which is reinforced by literature precedents.[13,14] There is precedent from work on other diiridium complexes that a rigid polymer matrix such as the cycloolefin polymer zeonex could also lead to a similar emission enhancement.[17]

This property could be anticipated for complex **5** which does not feature rigidifying intramolecular interactions to restrict bridge motion.[13,26,48,49] However, it is more surprising for **6**–**8**, for which intramolecular π–π interactions are observed in their solution ^{19}F NMR spectra (Figure 3) (similar to complex **4**, Figure 1). The non-emissive nature of complexes **6**–**8** in solution could be related to their high triplet energies (E_T) (≥ 2.70 eV), as we have previously noted that intramolecular π–π interactions become less effective at

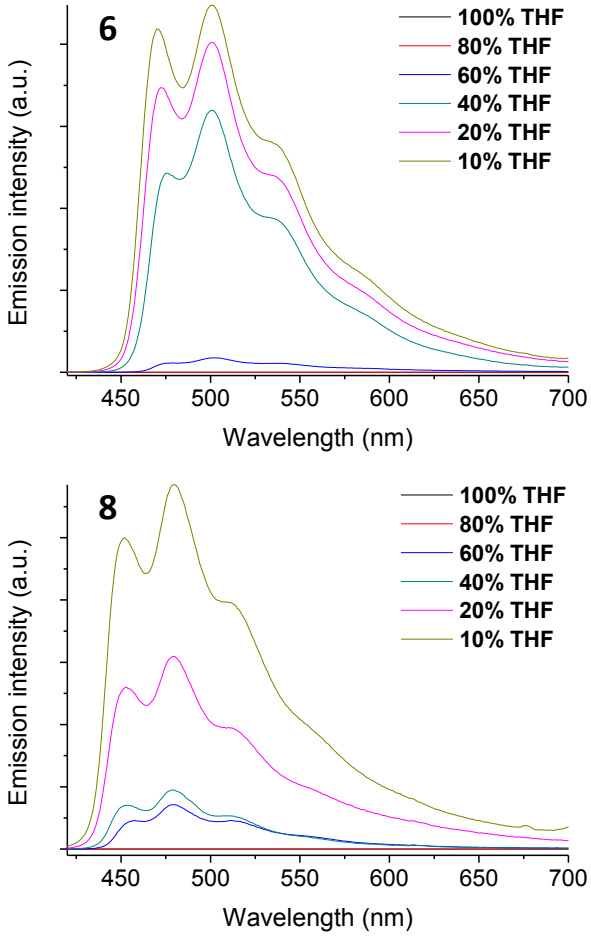

suppressing the non-radiative decay of hydrazide-bridged diiridium complexes in solution as their emission energies increase.[26]

Figure 7. Emission spectra for THF solutions of complexes **6** and **8** upon incremental titration of water to induce precipitation (λ_{exc} 355 nm). THF fraction is percentage volume.

The emission spectra of **5**–**8** at 77 K in 2-MeTHF are relatively broad and show distinct vibronic features. Minimal rigidochromic shifts are observed on cooling (≤ 3 nm) compared to the room temperature emission spectra recorded in PMMA. This implies a strong LC contribution to the excited states of **5**–**8**.[50] The Huang-Rhys factors (S_M) (estimated from the ratio of the $v_{0,0}$ and $v_{0,1}$ band intensities[51,52]) are also large: **5** = 0.8, **6** = 0.8, **7** = 1.0 and **8** > 1.0 (1 s.f.). These values imply

that the excited states of **5**–**8** are highly distorted compared to their ground states,[45] and are related to their non-emissive properties in solution. Comparing these data with those obtained for previous complexes,[13,26] there is a rational inverse relationship between the Huang-Rhys factor and the solution PLQY for hydrazide-bridged diiridium complexes. Complexes with S_M values of < 0.5 (e.g complex **4**) tend to be highly emissive (PLQY = ≥ 50%), those that are non-emissive in solution (e.g. **5**–**8**) have S_M values ≥ 0.7, and those that are weakly emissive (PLQY = *ca.* 1–5%) have intermediary S_M values of 0.5–0.7.

The PLQY of **5** in PMMA is notably lower than for **6**–**8** (11 ± 10% vs. *ca.* 50 ± 10%). This is ascribed to an absence of rigidifying intramolecular π–π interactions in **5** as its k_{nr} value is notably large (4.89 vs. 1.61 × 10^5 s^{-1} for **6**). The phosphorescence lifetimes of **6**–**8** are long for blue-green iridium phosphors.[53–57] For example, while **6** has a very similar E_T to the Hppy-derived complex **4** (2.70 vs. 2.72 eV) and a similar PLQY in PMMA (55 vs. 65 ± 10%), its τ is over twice as long (2.80 μs for **6** vs. 1.19 μs for **4**). This is related to the substantially lower k_r of **6** (1.96 × 10^5 s^{-1} vs. 5.46 × 10^5 s^{-1} for **4**) which is likely a consequence of a lower MLCT contribution to the excited state of **6**. Therefore, the long phosphorescence lifetimes and low radiative rates of **5**–**8** are likely to stem from high LC contributions to their excited states. This is evident from the well-resolved vibronic features in their emission spectra recorded in PMMA at room temperature: the $v_{0,0}$, $v_{0,1}$, $v_{0,2}$ and $v_{0,3}$ bands are all reasonably well-resolved. This conclusion is also supported by minimal rigidochromic shifts in the emission spectra of **5**–**8** upon cooling (mentioned above). Blue shifting the emission in the series **6**–**8** through fluorination of the cyclometalating ligands of **7** and **8** also leads to incremental increases in τ (i.e. for **8** τ = 4.55 μs and k_r = 1.96 × 10^5 s^{-1}). This fits a typical trend in Ir(III) phosphors, where the LC character of the excited state increases upon blue shifting the emission.[29,58,59]

Complexes **5**–**8** are emissive under UV irradiation (365 nm) in the solid state as powders. Typical aggregation-induced phosphorescent emission (AIPE) behaviour[47,60] is observed by titrating water into THF solutions of the complexes to induce precipitation/ aggregation, which promotes emission. The emission intensity increases as the THF fraction decreases. Spectra for complexes **6** and **8** are shown in Figure 7. Spectra for **5** and **7** are included in Figure S3. The mechanism which results in solid state emission from **5**–**8** is, in principle no different from that which promotes emission in dilute PMMA films, as evident from near-identical spectral profiles. In the solid state intramolecular motion is restricted due to interactions between neighbouring complexes, rather than between the complexes and a PMMA host. This property is enabled by the bulky (and ancillary – see DFT below) mesityl groups. In the solid state they increase the distances between the emissive 'cores' of the complexes, suppressing triplet-triplet annihilation as a quenching pathway (which dominates for unshielded diiridium complexes[13,61,62]). Complexes **5**–**8** greatly extend the spectral range of diiridium AIPE emitters – the most prominent literature examples are orange/ red[14,23] while **8** is sky-blue (CIE_{xy} = 0.18, 0.27 in PMMA).

Computational study

Electronic structure calculations were carried out on **5**–**8** at the B3LYP/LANL2DZ:3–21G* level[12,13,19,26] to gain insight into the photophysical properties of the complexes. In the optimised structures of **5**–**8** the central hydrazide fragments are predicted to be close to planar for both the *meso* and *rac* diastereomers. This contrasts with previously reported analogues,[12,13,26] for which the *rac* forms tend to be folded, and is assigned to the highly congested nature of the structures. The optimised structures of *meso* **7** and *meso* **8** are in good agreement with the X-ray data. However, the optimised geometries of the *rac* forms of **5**–**8** cannot be compared with X-ray data as no *rac* structures have been solved. Such similar optimised geometries for the *rac* and *meso* diastereomers of **6**–**8** may explain why they could not be separated.

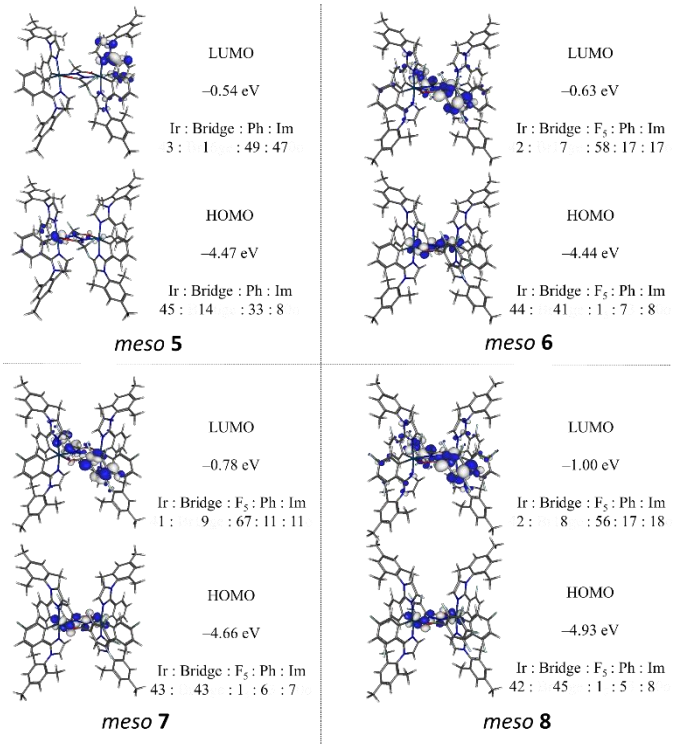

Figure 8. Molecular orbital compositions for *meso* **5**–**8**. The orbital contributions are percentages and the HOMO and LUMO energies were calculated at B3LYP/LANL2DZ:3–21G*. Bridge = central bridge OCNNCO fragment; F_5 = fluorinated bridge aryl rings; Ph = cyclometalating ligand phenyl groups; Im = cyclometalating ligand imidazolyl groups.

The predicted frontier molecular orbital (FMO) contributions are listed in Tables S2 and S3. Generally, there is a good agreement between diastereomers, and so FMO plots for *meso* **5**–**8** are presented in Figure 8. (The FMO plots for the *rac* diastereomers are included in Figures S4 and S5). For the diastereomers of **5**, the HOMOs are primarily localised on the Ir centres and the cyclometalating ligands, with some

contribution from the central hydrazide fragments of the bridging ligands, while the LUMOs are cyclometalating ligand-based. The spatial separation of the FMOs on the cyclometalating ligands is less defined than for typical Hppy-based complexes,[45,52,63] i.e. the LUMO contribution is split nearly equally between the phenyl and imidazole moieties. This is in good agreement with studies on mononuclear complexes with similar 1,2-diarylimidazole cyclometalating ligands.[40–42]

For **6–8** the HOMOs are mainly localised on the Ir centres and the central hydrazide fragments of the bridging ligands. Interestingly, rather than being based on the cyclometalating ligands, the LUMOs are primarily localised on the bridge pentafluorophenyl groups for **6–8**. This contrasts with the data reported for Hppy-based analogues such as **4**, for which the pentafluorophenyl groups are ancillary.[26] Presumably, this is due to the more electron rich nature of the imidazole heterocycles compared to pyridine, which forces the LUMO onto the strongly electron accepting pentafluorophenyl groups. As a result, the cyclometalating ligands of **6–8** are not major FMO contributors (their HOMO and LUMO contributions are ≤ 20%). Nevertheless, complexes **6–8** are emissive despite their unusual FMO distributions, highlighting the versatility of hydrazide bridges as a platform for obtaining emissive diiridium complexes.

To determine the significance of the unusual FMO distributions of **6–8**, a time-dependent density functional theory (TD-DFT) study was carried out to gain insight into the nature of their lowest energy excited states. This is because a simple consideration of the FMOs is not necessarily sufficient to predict the localisation of the lowest energy triplet states of Ir(III) complexes.[64–66] The data for both diastereomers of the least (**6**) and most (**8**) fluorinated derivatives are presented in Table 4 (the data for **7** show the same trends and are included in Table S4). The two largest contributing transitions to each state (≥ *ca*. 20%) are included. The TD-DFT data for **5** are included in Table S4.

Table 4. Summary of the TD-DFT data for complexes **6** and **8**.

Transition	6				8			
	meso		*rac*		*meso*		*rac*	
	Main orbital contribution	**λ/ nm**	**Main orbital contribution**	**λ/ nm**	**Main orbital contribution**	**λ/ nm**	**Main orbital contribution**	**λ/ nm**
$S_0 \rightarrow T_1$	HOMO → LUMO	429	HOMO-1 → LUMO+3, HOMO → LUMO+1	426	HOMO → LUMO	420	HOMO-1 → LUMO+3	409
$S_0 \rightarrow T_2$	HOMO-2 → LUMO+3, HOMO → LUMO+1	425	HOMO-1 → LUMO+1, HOMO → LUMO+3	425	HOMO → LUMO+1	410	HOMO-1 → LUMO+2, HOMO → LUMO+3	409
$S_0 \rightarrow T_3$	HOMO → LUMO+3, HOMO-2 → LUMO+2	423	HOMO-1 → LUMO+4, HOMO-2 → LUMO+1	417	HOMO → LUMO+3, HOMO-2 → LUMO+1	408	HOMO-1 → LUMO+4, HOMO-2 → LUMO+5	403
$S_0 \rightarrow T_4$	HOMO-1 → LUMO+2	416	HOMO-2 → LUMO+4	417	HOMO-1 → LUMO+4, HOMO-2 → LUMO+2	402	HOMO-2 → LUMO+4	403
$S_0 \rightarrow T_5$	HOMO-1 → LUMO+4	415	HOMO → LUMO+17	413	HOMO-1 → LUMO+2, HOMO-2 → LUMO+4	401	HOMO → LUMO+8	402

Both diastereomers of **6–8** feature 5 triplet states that are relatively close in energy (≤ 20 nm). A number of these states may, therefore, be relevant when considering their emissive states.[64] Such a large number of near-degenerate states, many of which have significant contributions from multiple transitions, complicates detailed analysis of the data. However, it can be noted that as well as a HOMO → LUMO transition, many of the relevant transitions in Table 4 involve contributions from higher energy unoccupied (LUMO+1 – LUMO+3), and lower energy occupied (HOMO−1 and HOMO−2) orbitals. Contributions for the HOMO−5 – LUMO+5 orbitals are tabulated in Tables S2 and S3. Particularly, while the LUMO+2 and LUMO+3 orbitals of **6–8** generally include a degree of pentafluorophenyl character, their cyclometalating ligand character is much higher than for the LUMOs (≥ 50%, as high as 100%). Also, the HOMO−1 and HOMO−2 orbitals for **6–8** are almost exclusively distributed between the Ir atoms and cyclometalating ligands (*ca.* 50:50 in all cases), in contrast to the HOMO orbitals that are mainly Ir and hydrazide based. Therefore, while it is likely that the pentafluorophenyl substituents are somewhat involved in the excited states of **6–8**, TD-DFT predicts that the cyclometalating ligands are more involved in their emitting states than is implied by a simple FMO analysis.[35,40] This analysis is in agreement with the photophysical data above. For example, the observation that the profiles of the PL spectra for **6–8** are very similar to those of homoleptic 2-phenylimidazole complexes[30,33–38] (which do not feature bridging ligands) signifies that their excited states should possess a high degree of LC character on the cyclometalating ligands.

Conclusions

A new family of hydrazide-bridged diiridium complexes **5–8** based on bulky 1,2-diarylimidazole cyclometalating ligands has been studied in detail.

The complexes **6–8** are strongly emissive when doped into PMMA. Significantly emissive ppy-free diiridium complexes are rare, and of these **6–8** exhibit the highest PLQYs yet reported (Φ_{PL} = 47–55 ± 10%).[23,31] They display emission peaks as blue shifted as 452 nm and complex **8** has CIE_{xy} colour coordinates in the sky-blue region (0.18, 0.27)**.** Prior to this work there have been only two reports of sky-blue diiridium complexes,[22,26] both containing Hppy ligands. We have shown, therefore, that Hppy is not essential for obtaining highly emissive diiridium complexes, and also Hppy is not required for the challenging task of shifting their emission into the sky-blue region. Moreover, complex **8** is as blue as the bluest mono-Ir complexes yet reported based on arylimidazole ligands.[35,38]

X-ray crystallography and solution-state ^{19}F NMR spectra reveal the presence of rigidifying intramolecular π–π interactions for complexes **6–8**, which explains their improved PLQYs compared to **5**. The rather long phosphorescence lifetimes of **6–8** have been attributed to the high ^{3}LC character of their excited states, which is corroborated by TD-DFT.

The complexes also display AIPE behaviour. This substantially broadens the colour range that can now be accessed by AIPE diiridium emitters towards the sky-blue and should provide added versatility in applications such as anti-counterfeiting.[67] This study considerably increases the scope of dinuclear Ir(III) complexes to include luminophoric ligands that are not restricted to Hppy-type cyclometalates, and provides a foundation for further diversification of emissive diiridium complexes away from conventional Hppy architectures.

Conflicts of interest

There are no conflicts to declare.

Acknowledgements

We thank EPSRC for funding equipment used in this study (grant EP/K0394/23/1).

Notes and references

1 E. Zysman-Colman, Ed., *Iridium(III) in Optoelectronic and Photonics Applications*, John Wiley & Sons, Chichester, 2017.

2 Y. Chi and P.-T. Chou, *Chem. Soc. Rev.*, 2010, **39**, 638–655.

3 Z. Q. Chen, Z. Q. Bian and C. H. Huang, *Adv. Mater.*, 2010, **22**, 1534–1539.

4 M. S. Lowry and S. Bernhard, *Chem. Eur. J.*, 2006, **12**, 7970–7977.

5 K. K.-W. Lo, K. H.-K. Tsang, K.-S. Sze, C.-K. Chung, T. K.-M. Lee, K. Y. Zhang, W.-K. Hui, C.-K. Li, J. S.-Y. Lau, D. C.-M. Ng and N. Zhu, *Coord. Chem. Rev.*, 2007, **251**, 2292–2310.

6 R. Gao, D. G. Ho, B. Hernandez, M. Selke, D. Murphy, P. I. Djurovich and M. E. Thompson, *J. Am. Chem. Soc.*, 2002, **124**, 14828–14829.

7 X. Yang, G. Zhou and W.-Y. Wong, *Chem. Soc. Rev.*, 2015, **44**, 8484–8575.

8 C. Ulbricht, B. Beyer, C. Friebe, A. Winter and U. S. Schubert, *Adv. Mater.*, 2009, **21**, 4418–4441.

9 T. Hajra, A. J. K. Bera and V. Chandrasekhar, *Aust. J. Chem.*, 2011, **64**, 561–566.

10 A. M. Prokhorov, A. Santoro, J. A. G. Williams and D. W. Bruce, *Angew. Chemie Int. Ed.*, 2012, **51**, 95–98.

11 M. Graf, R. Czerwieniec and K. Sünkel, *Z. Anorg. Allg. Chem.*, 2013, **639**, 1090–1094.

12 Y. Zheng, A. S. Batsanov, M. A. Fox, H. A. Al-Attar, K. Abdullah, V. Jankus, M. R. Bryce and A. P. Monkman, *Angew. Chem. Int. Ed.*, 2014, **53**, 11616–11619.

13 D. G. Congrave, Y. Hsu, A. S. Batsanov, A. Beeby and M. R. Bryce, *Organometallics*, 2017, **36**, 981–993.

14 G. Li, Y. Wu, G. Shan, W. Che, D. Zhu, B. Song, L. Yan, Z. Su and M. R. Bryce, *Chem. Commun.*, 2014, **50**, 6977–6980.

15 P.-H. Lanoë, C. M. Tong, R. W. Harrington, M. R. Probert, W. Clegg, J. A. G. Williams and V. N. Kozhevnikov, *Chem. Commun.*, 2014, **50**, 6831–6834.

16 V. Chandrasekhar, T. Hajra, J. K. Bera, S. M. W. Rahaman, N. Satumtira, O. Elbjeirami and M. A. Omary, *Inorg. Chem.*, 2012, **51**, 1319–1329.

17 R. E. Daniels, S. Culham, M. Hunter, M. C. Durrant, M. R. Probert, W. Clegg, J. A. G. Williams and V. N. Kozhevnikov, *Dalton. Trans.*, 2016, **45**, 6949–6962.

18 X. Yang, Z. Feng, J. Zhao, J.-S. Dang, B. Liu, K. Zhang and G. Zhou, *ACS Appl. Mater. Interfaces*, 2016, **8**, 33874–33887.

19 A. M'hamedi, M. A. Fox, A. S. Batsanov, H. A. Al-Attar, A. P. Monkman and M. R. Bryce, *J. Mater. Chem. C*, 2017, **5**, 6777–6789.

20 M. Y. Wong, G. Xie, C. Tourbillon, M. Sandroni, D. B. Cordes, A. M. Z. Slawin, I. D. W. Samuel and E. Zysman-Colman, *Dalton. Trans.*, 2015, **44**, 8419–8432.

21 G. Li, D. G. Congrave, D. Zhu, Z. Su and M. R. Bryce, *Polyhedron*, 2018, **140**, 146–157.

22 J. L. Liao, P. Rajakannu, P. Gnanasekaran, S. R. Tsai, C. H. Lin, S. H. Liu, C. H. Chang, G. H. Lee, P. T. Chou, Z. N. Chen and Y. Chi, *Adv. Opt. Mater.*, 2018, **6**, 1800083.

23 G. Li, W. Guan, S. Du, D. Zhu, G. Shan, X. Zhu, L. Yan, Z. Su, M. R. Bryce and A. P. Monkman, *Chem. Commun.*, 2015, **51**, 16924–16927.

24 Y. Jiang, G. Li, D. Zhu, Z. Su and M. R. Bryce, *J. Mater. Chem. C*, 2017, **5**, 12189–12193.

25 X. Yang, X. Xu, J. Dang, G. Zhou, C.-L. Ho and W.-Y. Wong, *Inorg. Chem.*, 2016, **55**, 1720–1727.

26 D. G. Congrave, Y.-T. Hsu, A. S. Batsanov, A. Beeby and M. R. Bryce, *Dalton. Trans.*, 2018, **47**, 2086–2098.

27 Y. Im, S. Y. Byun, J. H. Kim, D. R. Lee, C. S. Oh, K. S. Yook and J. Y. Lee, *Adv. Funct. Mater.*, 2017, **27**, 1603007–1603031.

28 Y. Chi and P.-T. Chou, *Chem. Soc. Rev.*, 2010, **39**, 638–655.

29 J. Li, P. I. Djurovich, B. D. Alleyne, M. Yousufuddin, N. N.

Ho, J. C. Thomas, J. C. Peters, R. Bau and M. E. Thompson, *Inorg. Chem.*, 2005, **44**, 1713–1727.
30 J. Zhuang, W. Li, W. Wu, M. Song, W. Su, M. Zhou and Z. Cui, *New J. Chem.*, 2015, **39**, 246–253.
31 G. Li, X. Ren, G. Shan, W. Che, D. Zhu, L. Yan, Z. Su and M. R. Bryce, *Chem. Commun.*, 2015, **51**, 13036–13039.
32 R. Davidson, Y.-T. Hsu, T. Batchelor, D. Yufit and A. Beeby, *Dalton. Trans.*, 2016, **45**, 11496–11507.
33 J. Zhuang, W. Li, W. Su, Y. Liu, Q. Shen, L. Liao and M. Zhou, *Org. Electron.*, 2013, **14**, 2596–2601.
34 K. Udagawa, H. Sasabe, C. Cai and J. Kido, *Adv. Mater.*, 2014, **26**, 5062–5066.
35 H. Cho, J. Lee, J. I. Lee, N. S. Cho, J. H. Park, J. Y. Lee and Y. Kang, *Org. Electron.*, 2016, **34**, 91–96.
36 Y. Zhang, J. Lee and S. R. Forrest, *Nat. Commun.*, 2014, **5**, 1–7.
37 K. Udagawa, H. Sasabe, F. Igarashi and J. Kido, *Adv. Opt. Mater.*, 2016, **4**, 86–90.
38 Y. Kwon, S. H. Han, S. Yu, J. Y. Lee and K. M. Lee, *J. Mater. Chem. C*, 2018, **6**, 4565–4572.
39 M. Micksch, M. Tenne and T. Strassner, *European J. Org. Chem.*, 2013, 6137–6145.
40 T. Karatsu, M. Takahashi, S. Yagai and A. Kitamura, *Inorg. Chem.*, 2013, **52**, 12338–12350.
41 E. Baranoff, S. Fantacci, F. De Angelis, X. Zhang, R. Scopelliti, M. Grätzel and M. K. Nazeeruddin, *Inorg. Chem.*, 2011, **50**, 451–462.
42 S. Takizawa, J. Nishida, T. Tsuzuki, S. Tokito and Y. Yamashita, *Inorg. Chem.*, 2007, **46**, 4308–4319.
43 D. G. Congrave, A. S. Batsanov, M. Du, Y. Liu, D. Zhu and M. R. Bryce, *Inorg. Chem.*, 2018, **57**, 12836–12849.
44 C. Hansch, A. Leo and R. W. Taft, *Chem. Rev.*, 1991, **91**, 165–195.
45 A. B. Tamayo, B. D. Alleyne, P. I. Djurovich, S. Lamansky, I. Tsyba, N. N. Ho, R. Bau and M. E. Thompson, *J. Am. Chem. Soc.*, 2003, **125**, 7377–7387.
46 S. Lamansky, P. Djurovich, D. Murphy, F. Abdel-Razzaq, H. E. Lee, C. Adachi, P. E. Burrows, S. R. Forrest and M. E. Thompson, *J. Am. Chem. Soc.*, 2001, **123**, 4304–4312.
47 J. Mei, N. L. C. Leung, R. T. K. Kwok, J. W. Y. Lam and B. Z. Tang, *Chem. Rev.*, 2015, **115**, 11718–11940.
48 C. E. Housecroft and E. C. Constable, *Coord. Chem. Rev.*, 2017, **350**, 155–177.
49 R. D. Costa, E. Ortí, H. J. Bolink, F. Monti, G. Accorsi and N. Armaroli, *Angew. Chem. Int. Ed.*, 2012, **51**, 8178–8211.
50 E. S. Andreiadis, D. Imbert, J. Pécaut, A. Calborean, I. Ciofini, C. Adamo, R. Demadrille and M. Mazzanti, *Inorg. Chem.*, 2011, **50**, 8197–8206.
51 G. Li, T. Fleetham, E. Turner, X. C. Hang and J. Li, *Adv. Opt. Mater.*, 2015, **3**, 390–397.
52 J. Li, P. I. Djurovich, B. D. Alleyne, M. Yousufuddin, N. N. Ho, J. C. Thomas, J. C. Peters, R. Bau and M. E. Thompson, *Inorg. Chem.*, 2005, **44**, 1713–1727.
53 A. F. Henwood, A. K. Bansal, D. B. Cordes, A. M. Z. Slawin, I. D. W. Samuel and E. Zysman-Colman, *J. Mater. Chem. C*, 2016, **4**, 3726–3737.
54 C.-H. Yang, M. Mauro, F. Polo, S. Watanabe, I. Muenster, R. Frohlich and L. De Cola, *Chem. Mater.*, 2012, **24**, 3684–3695.
55 T. Duan, T.-K. Chang, Y. Chi, J.-Y. Wang, Z.-N. Chen, W.-Y. Hung, C.-H. Chen and G.-H. Lee, *Dalton. Trans.*, 2015, **44**, 14613–14624.
56 H. J. Park, J. N. Kim, H. Yoo, K. Wee, S. O. Kang and D. W. Cho, *J. Org. Chem.*, 2013, **78**, 8054–8064.
57 T. B. Fleetham, L. Huang, K. Klimes, J. Brooks and J. Li, *Chem. Mater.*, 2016, **28**, 3276–3282.
58 M. A. Baldo, S. R. Forrest and M. E. Thompson, in *Organic Electroluminescence*, ed. Z. H. Kafafi, CRC and SPIE Press, 2005.
59 L. Yang, F. Okuda, K. Kobayashi, K. Nozaki, Y. Tanabe, Y. Ishii and M.-A. Haga, *Inorg. Chem.*, 2008, **47**, 7154–7165.
60 L. Ravotto and P. Ceroni, *Coord. Chem. Rev.*, 2017, **346**, 62–76.
61 S. Reineke, K. Walzer and K. Leo, *Phys. Rev. B - Condens. Matter Mater. Phys.*, 2007, **75**, 125328.
62 N. C. Giebink and S. R. Forrest, *Phys. Rev. B - Condens. Matter Mater. Phys.*, 2008, **77**, 235215.
63 H. Benjamin, Y. Zheng, A. S. Batsanov, M. A. Fox, H. A. Al-Attar, A. P. Monkman and M. R. Bryce, *Inorg. Chem.*, 2016, **55**, 8612–8627.
64 H. J. Bolink, F. De Angelis, E. Baranoff, C. Klein, S. Fantacci, E. Coronado, M. Sessolo, K. Kalyanasundaram, M. Grätzel and M. K. Nazeeruddin, *Chem. Commun.*, 2009, 4672–4674.
65 E. Baranoff and B. F. E. Curchod, *Dalton Trans.*, 2015, **44**, 8318–8329.
66 X. Gu, T. Fei, H. Zhang, H. Xu, B. Yang, Y. Ma and X. Liu, *J. Phys. Chem. A*, 2008, **112**, 8387–8393.
67 Y. Jiang, G. Li, W. Che, Y. Liu, B. Xu, G. Shan, D. Zhu, Z. Su and M. R. Bryce, *Chem. Commun.*, 2017, **53**, 3022–3025.

Supporting Information

Highly Luminescent 2-Phenylpyridine-Free Diiridium Complexes with Bulky 1,2-Diarylimidazole Cyclometalating Ligands

Daniel G. Congrave* Andrei S. Batsanov and Martin R. Bryce*

Department of Chemistry, Durham University, Durham DH1 3LE, U.K.

Email: m.r.bryce@durham.ac.uk

Contents **Page**

Experimental Section

General

^{1}H, ^{13}C and ^{19}F NMR spectra were recorded on Bruker Avance 400 MHz, Varian Mercury 200, and 400 MHz, Varian Inova 500 MHz or Varian VNMRS 600 and 700 MHz spectrometers. All spectra were either referenced against the residual solvent signal or tetramethylsilane (TMS) and peak shifts are reported in ppm. For ^{13}C NMR assignment the labels * and # denote 2 and 3 overlapping signals, respectively. Electrospray ionisation (ESI) mass spectra were recorded on a Waters Ltd. TQD spectrometer. Atmospheric solids analysis probe (ASAP) mass spectra were recorded on a LCT premier XE spectrometer. Matrix-assisted laser desorption time-of-flight (MALDI–TOF) mass spectra were recorded on a Bruker Daltonik Autoflex II spectrometer running in positive ion reflectron mode. MALDI–TOF samples were prepared in CH_2Cl_2 (DCM) with *trans*-2-[3-(4-*tert*-butylphenyl)-2-methyl-2-propenylidene]malononitrile (DCTB) as the matrix. Elemental analyses were obtained on an Exeter Analytical Inc. CE-440 elemental analyser. Thermal analysis was run under a helium atmosphere at a rate of 10 °C min^{-1} using a Perkin-Elmer Pyris 1 instrument. Reactions requiring an inert atmosphere were carried out under argon which was first passed through a phosphorus pentoxide column. Thin layer chromatography (TLC) was carried out on silica gel (Merck, silica gel 60, F254) or alumina (Merck, neutral alumina 60 type E, F254) plates and visualised using UV light (254, 315, 365 nm). Flash chromatography was carried out using either glass columns or a Biotage® Isolera OneTM automated flash chromatography machine on 60 micron silica gel purchased from Fluorochem Ltd.

Chemicals

All commercial chemicals were of ≥95% purity and were used as received without further purification. *N*-(2,2-Diethoxyethyl)mesitylamine (**S1**),[1] bis(trifluoromethyl)hydrazide (2H**13**) and *N*,*N*′-bis(pentafluorobenzoyl)hydrazide (2H**12**)[2] were prepared by literature procedures. All solvents used were of analytical reagent grade or higher. Anhydrous solvents were dried through a HPLC column on an Innovative Technology Inc. solvent purification system or purchased from Acros (dry diglyme).

Calculations

All calculations were carried out with the Gaussian 09 package.[3] All optimised S_0 geometries of the diiridium complexes were carried out using B3LYP[4,5] with the pseudopotential (LANL2DZ)[6–8] for iridium and 3–21G* basis set for all other atoms.[9,10] All S_0 geometries were true minima based on no imaginary frequencies found. Electronic structure calculations were also carried out on the optimised geometries at B3LYP/LANL2DZ:3–21G*. The MO diagrams and orbital contributions were generated with the aid of Gabedit[11] and GaussSum[12] packages, respectively.

X-ray Crystallography

X-ray diffraction experiments were carried out at 120 K on a Bruker 3-circle diffractometer D8 Venture with a PHOTON 100 CMOS area detector, using Mo-*K*α radiation from an Incoatec IμS microsource with focussing mirrors and a Cryostream (Oxford Cryosystems) open-flow N_2 gas cryostat. The absorption correction was carried out by numerical integration based on crystal face indexing, using SADABS program.[13] The structures were solved by Patterson or direct methods using SHELXS 2013/1 software[14] and refined in anisotropic approximation by full matrix least squares against F^2 off all data, using SHELXL 2018/3 software[15] on OLEX2[16] platform. In both structures, the asymmetric unit comprises half of the complex molecule (which possesses a crystallographic inversion centre), as well as three DCM molecules (*meso*-**7**) or one methanol molecule (*meso*-**8**). Crystal data are listed in Table S5.

Electrochemistry

Cyclic voltammetry experiments were recorded using either BAS CV50W electrochemical analyzer or a a PalmSens EmStat^2 potentiostat with PSTrace software. A three-electrode system consisting of a Pt disk (Ø = 1.8 mm) as the working electrode, a Pt wire as an auxiliary electrode and an Pt wire as a quasireference electrode was used. Cyclic voltammetry experiments were conducted at a scan rate of 100 mV/s. Experiments were conducted in dry, degassed DCM with *n*-Bu_4NPF_6 (0.1 M) as the supporting electrolyte for oxidations, and in dry, degassed THF with *n*-Bu_4NPF_6 (0.1 M) as the supporting electrolyte for reductions. All experiments were referenced internally to ferrocene. Oxidation processes are assigned as being electrochemically reversible based on the equal magnitudes of corresponding oxidation and reduction peaks.

Photophysics

General. The absorption spectra were measured on either a Unicam UV2-100 spectrometer operated with the Unicam Vision software or a Thermo Scientific Evolution 220 spectrometer with the Thermo Scientific Insight software in quartz cuvettes with a path length of 20 mm. The pure solvent was used for the baseline correction. The extinction coefficients were calculated using the Beer-Lambert Law, $A = \varepsilon cl$. They were measured using a titration method, whereby a stock solution of known concentration was incrementally added using a calibrated glass pipette to a cuvette of pure solvent. A minimum of 1 mg of sample was weighed for the stock solutions, and the measurements were carried out in triplicate to minimise weighing and dilution-errors. The photoluminescence spectra were recorded on a Horiba Jobin Yvon SPEX Fluorolog 3-22 spectrofluorometer in quartz cuvettes with a path length of 10 mm. All Ir complexes were measured in degassed DCM (repeated freeze-pump-thaw cycles using a turbomolecular pump). The quantum yields of all samples were determined by the comparative method relative to quinine sulphate in 0.5 M H_2SO_4 ($\Phi = 0.546$[17]) following the literature procedure.[18] Poly(methyl methacrylate) films were prepared according to a literature procedure.[2] The quantum yields of complexes doped in PMMA thin films were recorded on a Horiba Jobin Yvon SPEX Fluorolog 3 using a calibrated Quanta-Φ integrating sphere and were calculated according to the literature method.[19] Solid state PLQY data were obtained in triplicate from three samples that were prepared in parallel: the calculated standard error values were ≤10%. Lifetime measurements were recorded using an N_2 laser (337 nm, 10 μJ, 10 Hz) as an excitation source in a custom spectrometer which produced a 1 kHz train of pulses of 20 ns duration. The luminescence was collected at 90° and focused onto the entrance slit of a monochromator (Bethan TM 300V). The emission was detected by a photon counting PMT and the arrival times of photons at the detector determined using a multichannel scaler. The data were transferred to a PC and analysed using non-linear regression. The decay data were fitted to exponential functions. Low temperature emission spectra and lifetime data were measured in a DN1704 optical cryostat (Oxford Instruments) with a ITC601 temperature controller (Oxford Instruments).

Synthesis

General procedure for the synthesis of 1,2-diarylimidazoles (H**9**–H**11).** Based on a literature procedure.[20] **Step I.** Based on *ca.* 10 mmol scale of *N*-(2,2-diethoxyethyl)mesitylamine (**S1**). Triethylamine (2.00 eq.) and the benzoyl chloride derivative (5.00 eq.) were added sequentially to a solution of *N*-(2,2-diethoxyethyl)mesitylamine (**S1**) (1.00 eq.) in DCM (20 mL) under argon at 0 °C. The mixture was warmed to room temperature and stirred overnight. The solvent was then removed under reduced pressure and the residue was dissolved in acetone/ water (9:1 v/v, 20 mL). *para*-Toluenesulfonic acid (2.10 eq.) was added and the resulting mixture was heated to reflux for 2 h. The solvent was evaporated under reduced pressure and the residue was dissolved in EtOAc (80 mL). The solution was washed with sat. aq. Na_2CO_3 (2 × 50 mL). The washings were combined and extracted with EtOAc (3 × 80 mL). All organic layers were then combined, washed with water (20 mL), dried over $MgSO_4$ and filtered. After evaporation of the solvent, the residue (**A**) was used in Step II without further purification. **Step II.** The product (**A**) from Step I was cautiously dissolved in acetic anhydride (15 mL). The solution was cooled to 0 °C and aq. HBF_4 (50%, 1.20 eq.) was added slowly. The resulting mixture was stirred overnight at room temperature. It was then added dropwise to stirred diethyl ether (100 mL) to precipitate the intermediate salt **B**. Prolonged stirring, sonication or scratching was sometimes required to induce precipitation. The solid was filtered and washed with Et_2O (2 × 10 mL). **Step III.** The product (**B**) from Step II was dissolved in MeCN (30 mL). NH_4OAc (1.70 eq.) was added and the solution was stirred at room temperature for 24 h. Next, aq. HBF_4 (50%, 1.70 eq.) was added and the reaction mixture was heated to reflux overnight. The solvent was evaporated under reduced pressure and the residue was dissolved in EtOAc (80 mL). The solution was washed with sat. aq. Na_2CO_3 (2 × 50 mL). The washings were combined and extracted with EtOAc (3 × 80 mL). All organic layers were then combined, washed with water (20 mL), dried over $MgSO_4$ and filtered. After evaporation of the solvent the residue was purified by flash chromatography on silica gel.

1-(2,4,6-Trimethylphenyl)-2-phenylimidazole (H**9).** 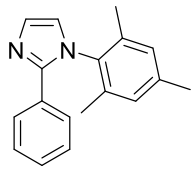 The general procedure for 1,2-diarylimidazoles was followed starting from *N*-(2,2-diethoxyethyl)mesitylamine (**S1**) (6.63 g, 26.4 mmol, 1.00 eq.) and benzoyl chloride (18.6 g, 132 mmol, 5.00 eq.). The crude product was purified by flash chromatography on silica gel (eluent: gradient 1:0–6:4 *n*-hexane/ EtOAc v/v with *ca.* 0.5% NEt_3 as additive) to obtain 1-(2,4,6-trimethylphenyl)-2-phenylimidazole (H**9**) as an off-white powder (4.40 g, 16.7 mmol, 63%). NMR analytical data were in agreement with those previously reported.[20] ^{1}H NMR (400 MHz, $CDCl_3$) δ (ppm) = 7.46 – 7.41 (m, 2H), 7.33 (d, *J* = 1.2 Hz, 1H), 7.26 – 7.20 (m, 3H), 6.99 – 6.96 (m, 2H), 6.91 (d, *J* = 1.2 Hz, 1H), 2.37 (s, 3H), 1.94 (s, 6H).

1-(2,4,6-Trimethylphenyl)-2-(4-fluorophenyl)imidazole (H**10).** 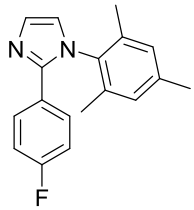 The general procedure for 1,2-diarylimidazoles was followed starting from *N*-(2,2-diethoxyethyl)mesitylamine (**S1**) (3.17 g, 12.6 mmol, 1.00 eq.) and 4-fluorobenzoyl chloride (10.0 g, 63.0 mmol, 5.00 eq.). The crude product was purified by flash chromatography on silica gel (eluent: gradient 1:0–6:4 *n*-hexane/ EtOAc v/v with *ca.* 0.5% NEt_3 as additive) to obtain 1-(2,4,6-trimethylphenyl)-2-(4-fluorophenyl)imidazole (H**10**) as an off-white powder (2.12 g, 7.56 mmol, 60%). M.pt. 107–109 °C; ^{1}H NMR (400 MHz, $CDCl_3$) δ (ppm) = 7.43 – 7.37 (m, 2H), 7.31 (d, *J* = 1.3 Hz, 1H), 6.98 (s, 2H), 6.96 – 6.88 (m, 3H), 2.37 (s, 3H), 1.93 (s, 6H); ^{13}C NMR (101 MHz, $CDCl_3$) δ (ppm) = 162.6 (d, *J* = 248.4 Hz), 145.5, 139.0, 135.2, 134.4, 129.4, 129.3, 128.6 (d, *J* = 8.2 Hz), 127.0 (d, *J* = 3.4 Hz), 121.9, 115.4 (d, *J* = 21.6 Hz), 21.1, 17.6; ^{19}F{^{1}H} NMR (376 MHz, $CDCl_3$) δ (ppm) = -113.1 (s, 1F); HRMS (ESI): *m/z* 281.1458 [MH^+]. Calcd. for $C_{18}H_{18}FN_2^+$: 281.1454.

1-(2,4,6-Trimethylphenyl)-2-(2,4-difluorophenyl)imidazole (H**11).** 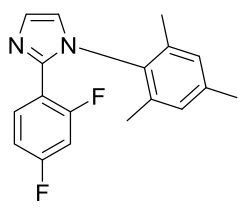 A modification of the general procedure for 1,2-diarylimidazoles was followed starting from *N*-(2,2-diethoxyethyl)mesitylamine (**S1**)

(3.33 g, 13.2 mmol, 1.00 eq.) and 2,4-difluorobenzoyl chloride (9.30 g, 66.0 mmol, 5.00 eq.) where aq. PF_6 (65%, 1.20 eq.) was used instead of aq. HBF_4 in step II. The crude product was purified by flash chromatography on silica gel (eluent: gradient 1:0–4:6 *n*-hexane/ EtOAc v/v with *ca*. 0.5% NEt_3 as additive) to obtain 1-(2,4,6-trimethylphenyl)-2-(2,4-difluorophenyl)imidazole (H**11**) as an off-white powder (2.22 g, 7.39 mmol, 56%). M.pt. 80.5–82 °C; ^{1}H NMR (400 MHz, $CDCl_3$) δ (ppm) = 7.37 (d, *J* = 1.3 Hz, 1H), 7.32 (td, *J* = 8.5, 6.4 Hz, 1H), 7.00 (d, *J* = 1.3 Hz, 1H), 6.89 (s, 2H), 6.82 (dddd, *J* = 8.7, 7.8, 2.5, 0.7 Hz, 1H), 6.74 (ddd, *J* = 10.2, 8.9, 2.5 Hz, 1H), 2.31 (s, 3H), 1.96 – 1.93 (m, 6H); ^{13}C NMR (101 MHz, $CDCl_3$) δ (ppm) = 163.1 (dd, *J* = 251.7, 12.0 Hz), 160.3 (dd, *J* = 254.4, 12.8 Hz), 142.2 (d, *J* = 2.5 Hz), 138.6, 135.1, 133.4, 132.4 (dd, *J* = 9.7, 4.1 Hz), 129.8, 129.1, 122.1, 115.6 (dd, *J* = 14.4, 3.9 Hz), 111.4 (dd, *J* = 21.3, 3.9 Hz), 104.4 (t, *J* = 25.7 Hz), 21.0, 17.6; ^{19}F{^{1}H} NMR (376 MHz, $CDCl_3$) δ (ppm) = -108.2 (dd, *J* = 8.8, 0.9 Hz, 1F), -108.4 (dd, *J* = 8.9, 1.1 Hz, 1F); HRMS (ESI): *m/z* 299.1363 [MH^+]. Calcd. for $C_{18}H_{17}F_2N_2^+$: 299.1360.

Complex 5. $IrCl_3 \cdot 3H_2O$ (250 mg, 0.71 mmol, 1.00 eq.) and 1-(2,4,6-trimethylphenyl)-2-phenylimidazole (H**9**) (390 mg, 1.49 mmol, 2.10 eq.) were added to 2-ethoxyethanol (10 mL) and the mixture was heated to reflux under an argon atmosphere for 24 h to form the dichloro-bridged diiridium intermediate *in situ*. The reaction mixture was then cooled to room temperature before addition of *N*,*N*′-bis(trifluoromethyl)hydrazide (2H**13**) (79 mg, 0.35 mmol, 0.50 eq.) and K_2CO_3 (147 mg, 1.06 mmol, 1.49 eq.). The mixture was then heated at reflux for a further 24 h before being cooled to room temperature. The solvent was evaporated, and the residue was purified by flash chromatography on silica gel (eluent: gradient 1:1–0:1 *n*-hexane/ DCM sat. K_2CO_3). After removing the solvent under reduced pressure, the residue was dissolved in a minimal amount of DCM (*ca*. 10 mL). Addition of hexane (*ca*. 20 mL) followed by reducing the volume of the mixture to 20 mL afforded complex **5** (400 mg, 0.24 mmol, 68%) as a light yellow precipitate which was isolated via filtration and washed with pentane. It was isolated as a single diastereomer. ^{1}H NMR (700 MHz, CD_2Cl_2, TMS) δ (ppm) = 7.28 (d, *J* = 1.5 Hz, $2H_{A5}$), 7.22 (d, *J* = 1.5 Hz, $2H_{B5}$), 7.11 – 7.07 (m, $10H_{A4,\ mesAr}$), 6.89 (d, *J* = 1.5 Hz, $2H_{B4}$), 6.61 (td, *J* = 7.5, 1.4 Hz, $2H_{C4}$), 6.54 (ddd, *J* = 8.1, 7.2, 1.4 Hz, $2H_{D4}$), 6.49 (td, *J* = 7.5, 1.2 Hz, $2H_{C5}$), 6.43 – 6.41 (m, $4H_{D3,\ D5}$), 6.25 (dd, *J* = 7.5, 1.2 Hz, $2H_{C3}$), 6.14 – 6.12 (m, $4H_{C6,\ D6}$), 2.41 (s, $6H_{mesMe}$), 2.41 (s, $6H_{mesMe}$), 2.13 (s, $6H_{mesMe}$), 2.08 (s, $6H_{mesMe}$), 1.96 (s, $6H_{mesMe}$), 1.95 (s, $6H_{mesMe}$); ^{19}F NMR (376 MHz, CD_2Cl_2) δ (ppm) = -66.4 (s, 3F); ^{13}C NMR (176 MHz, CD_2Cl_2, TMS) δ (ppm) = 157.9 (C_{A2}), 157.1 (B_{B2}), 146.5 (C_{D2}), 144.3 (C_{C2}), 140.0* (C_{mesAr}), 135.8–135.7 ($C_{4\ \times\ mesAr}$), 135.7 (C_{C1}), 135.2 (C_{D1}), 133.8 (C_{D3}), 133.0 (C_{mesAr}), 132.8 (C_{mesAr}), 132.2 (C_{C3}), 129.4–129.3 ($C_{4\ \times\ mesAr}$), 127.7 (C_{C4}), 126.9* ($C_{B5,\ D4}$), 125.1 (C_{A5}), 121.0 ($C_{C6\ or\ D6}$), 120.7 (C_{C5}), 120.6 ($C_{C6\ or\ D6}$), 119.8 ($C_{A4,\ B4}$), 118.9 (C_{D5}), 20.9* (C_{mesMe}), 17.5* (C_{mesMe}), 17.0* (C_{mesMe}); MS (MALDI–TOF): *m/z* 1652.3 [M^+]. Calcd. for $C_{76}H_{68}F_6Ir_2N_{10}O_2^+$: 1652.5; Anal. Calcd. for $C_{76}H_{68}F_6Ir_2N_{10}O_2$: C, 55.26; H, 4.15; N, 8.48, Calcd. for $C_{76}H_{68}F_6Ir_2N_{10}O_2 \cdot 0.5CH_2Cl_2$: C, 54.23; H, 4.10; N, 8.27. Found: C, 54.40; H, 4.04; N, 8.34. Due to low solubility in organic solvents and coupling to ^{19}F nuclei, the quarternary bridge ^{13}C NMR signals were not observed. All signals that could be clearly identified in the ^{13}C, ^{1}H–^{13}C HSQC and ^{1}H–^{13}C HMBC NMR spectra are reported. Some of the aromatic mesityl ^{13}C environments are reported as a range due to the large number of overlapping signals.

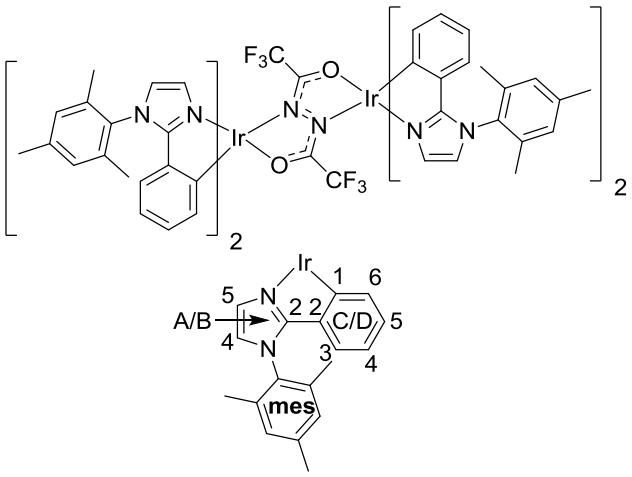

General procedure for the synthesis of the diarylhydrazide-bridged complexes (6–8). $IrCl_3 \cdot 3H_2O$ (250 mg, 0.71 mmol, 1.00 eq.) and the 1,2-diarylimidazole cyclometallating ligand (1.49 mmol, 2.10 eq.) were added to 2-ethoxyethanol (10 mL) and the mixture was heated to reflux under an argon atmosphere for 24 h to form the

dichloro-bridged diiridium intermediate *in situ*. The reaction mixture was cooled to room temperature and the solvent was evaporated under reduced pressure. The residue was then dried under high vacuum. Next, *N*,*N*′-bis(pentafluorobenzoyl)hydrazide (2H**12**) (149 mg, 0.35 mmol, 0.50 eq.) and K_2CO_3 (147 mg, 1.06 mmol, 1.49 eq.) were added and the mixture was suspended in dry diglyme (15 mL). It was then heated in a 120 °C heating mantle under argon overnight. The reaction was cooled to room temperature and the solvent was subsequently removed under reduced pressure. The residue was firstly purified by flash chromatography on silica gel (eluent: typically gradient *n*-hexane/ DCM sat. K_2CO_3) and then dissolved in minimal DCM (*ca*. 10 mL). Addition of hexane (*ca*. 20 mL) followed by reducing the volume of the mixture to 20 mL afforded the complexes as coloured precipitates which were isolated via filtration and washed with pentane.

Complex 6. Prepared according to the general procedure, complex **6** was obtained as a light yellow powder (460 mg, 0.25 mmol, 70%). The flash chromatography eluent was DCM sat. K_2CO_3. **6** was obtained as a diastereomeric mixture in a *ca.* 1:1 ratio. This complicates NMR assignment of the individual diastereomers making them very difficult to distinguish and so the overlapping spectra of the mixture are reported. ^{1}H and ^{13}C Signals are assigned based on whether they represent imidazole (A), phenyl (B) or mesityl (mes) environments. Coupling constants in ^{1}H NMR are ± 0.5 Hz. ^{1}H NMR (700 MHz, CD_2Cl_2, TMS) δ (ppm) = 7.64 – 7.62 (m, $2H_A$), 7.54 (d, *J* = 1.5 Hz, $2H_A$), 7.49 (d, *J* = 1.6 Hz, $2H_A$), 7.20 (d, *J* = 1.9 Hz, $2H_{mesAr}$), 7.17 (d, *J* = 1.9 Hz, $2H_{mesAr}$), 7.13 (d, *J* = 1.5 Hz, $2H_A$), 7.08 (dd, *J* = 9.6, 1.6 Hz, $10H_{2\times A,\ mesAr}$), 7.06 – 7.04 (m, $6H_{mesAr}$), 6.97 (d, *J* = 1.5 Hz, $2H_A$), 6.92 (d, *J* = 1.5 Hz, $2H_A$), 6.53 – 6.49 (m, $4H_{2\times B}$), 6.44 – 6.39 (m, $4H_{2\times B}$), 6.37 – 6.33 (m, $2H_B$), 6.33 – 6.28 (m, $8H_{4\times B}$), 6.18 – 6.11 (m, $10H_{5\times B}$), 6.10 (dd, *J* = 7.7, 1.3 Hz, $2H_B$), 6.07 (dd, *J* = 7.8, 1.3 Hz, $2H_B$), 2.43 – 2.42 (m, $12H_{mesMe}$), 2.40 (s, $6H_{mesMe}$), 2.40 (s, $6H_{mesMe}$), 2.37 (s, $6H_{mesMe}$), 2.27 (s, $6H_{mesMe}$), 2.08 (s, $6H_{mesMe}$), 2.06 (s, $6H_{mesMe}$), 2.01 – 2.00 (m, $18H_{mesMe}$), 1.82 (s, $6H_{mesMe}$); ^{19}F {^{1}H} NMR (376 MHz, CD_2Cl_2) δ (ppm) = -140.70 (dd, *J* = 24.7, 6.5 Hz, 2F), -141.89 (dd, *J* = 24.7, 7.2 Hz, 2F), -142.95 (dd, *J* = 24.5, 7.4 Hz, 2F), -143.87 (dd, *J* = 23.8, 7.5 Hz, 2F), -158.1 – - 157.9 (m, 4F), -161.53 (td, *J* = 24.1, 22.4, 7.5 Hz, 2F), -162.14 (td, *J* = 24.2, 7.5 Hz, 2F), -163.90 (td, *J* = 23.1, 7.6 Hz, 2F), -164.79 (td, *J* = 22.9, 7.2 Hz, 2F); ^{13}C NMR (176 MHz, CD_2Cl_2, TMS) δ (ppm) = 183.6* ($C_{C=O}$), 157.5 (C_A), 157.4 (C_A), 157.3 (C_A), 157.0 (C_A), 148.5 (C_B), 148.0 (C_B), 147.3 (C_B), 146.9 (C_B), 139.7 ($C_{4\times mesAr}$), 136.1* (C_B), 135.8 ($C_{4\times mesAr}$), 135.6 ($C_{4\times mesAr}$), 134.8 (C_B), 134.6 (C_B), 132.9 ($C_{4\times mesAr,\ 2\times B}$), 132.5 ($C_{2\times B}$) 129.5* ($C_{mesAr}$), 129.4# ($C_{mesAr}$), 129.3# ($C_{mesAr}$), 127.5 ($C_{2\times B}$), 127.2 ($C_B$), 127.0 ($C_B$), 126.7* ($C_A$), 125.5 ($C_A$), 125.4 ($C_A$), 120.9 ($C_{4\times B}$), 120.8 ($C_B$), 120.6* ($C_B$), 120.5 ($C_A$), 120.1 ($C_A$), 119.8 ($C_A$), 119.5 ($C_A$), 118.4 ($C_B$), 20.9* ($C_{mesMe}$), 20.8* ($C_{mesMe}$), 17.9* ($C_{mesMe}$), 17.3* ($C_{mesMe}$), 16.9 ($C_{mesMe}$), 16.8 ($C_{mesMe}$), 16.6 ($C_{mesMe}$), 16.5 ($C_{mesMe}$); MS (MALDI–TOF): *m/z* 1848.4 [M^+]. Calcd. for $C_{86}H_{68}F_{10}Ir_2N_{10}O_2^+$: 1848.5; Anal. Calcd. for $C_{86}H_{68}F_{10}Ir_2N_{10}O_2$: C, 55.90; H, 3.71; N, 7.58, Calcd. for $C_{86}H_{68}F_{10}Ir_2N_{10}O_2{\cdot}0.3CH_2Cl_2$: C, 55.33; H, 3.69; N, 7.48. Found: C, 55.32; H, 3.66; N, 7.46. Due to poor solubility in organic solvents and extensive coupling to ^{19}F nuclei, the ^{13}C environments corresponding to the pentafluorophenyl groups were not observed. All signals that could be clearly identified in the ^{13}C, ^{1}H–^{13}C HSQC and ^{1}H–^{13}C HMBC NMR spectra are reported.

Complex 7. Prepared according to the general procedure, complex **7** was obtained as a light yellow powder (420 mg, 0.22 mmol, 62%). The flash chromatography eluent was DCM sat. K_2CO_3. **7** was obtained as a diastereomeric mixture in a *ca.* 1:0.6 ratio. MS (MALDI–TOF): *m/z* 1920.3 [M^+]. Calcd. for $C_{86}H_{64}F_{14}Ir_2N_{10}O_2^+$: 1920.4; Anal. Calcd. for $C_{86}H_{64}F_{14}Ir_2N_{10}O_2$: C, 53.80; H, 3.36; N, 7.30, Calcd. for $C_{86}H_{64}F_{14}Ir_2N_{10}O_2 \cdot 0.3CH_2Cl_2$: C, 53.28; H, 3.35; N, 7.20. Found: C, 53.22; H, 3.27; N, 7.20.

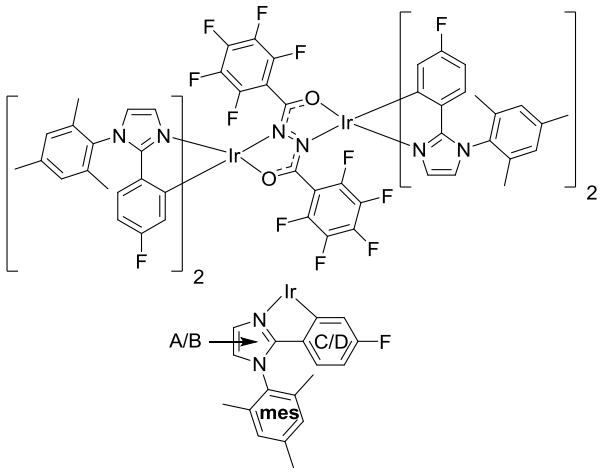

Major diastereomer: ^{1}H NMR (700 MHz, CD_2Cl_2, TMS) δ (ppm) = 7.51 (d, *J* = 1.5 Hz, $2H_A$), 7.43 (s, $2H_B$), 7.18 (s, $2H_{mesAr}$), 7.16 (d, *J* = 1.5 Hz, $2H_A$), 7.09 – 7.05 (m, $6H_{3 \times mesAr}$), 6.93 (d, *J* = 1.5 Hz, $2H_B$), 6.18 – 6.05 (m, $8H_{2 \times C, 2 \times D}$), 5.87 (dd, *J* = 10.2, 2.6 Hz, $2H_C$), 5.80 – 5.77 (m, $2H_D$), 2.43 (s, $6H_{mesMe}$), 2.39 (s, $6H_{mesMe}$), 2.24 (s, $6H_{mesMe}$), 2.07 (s, $6H_{mesMe}$), 2.01 (s, $6H_{mesMe}$), 1.81 (s, $6H_{mesMe}$); ^{19}F NMR (376 MHz, CD_2Cl_2) δ (ppm) = -113.13 (d, *J* = 1.4 Hz, 2F), -113.35 (d, *J* = 1.4 Hz, 2F), -141.74 (dd, *J* = 24.5, 7.6 Hz, 2F), -142.60 (dd, *J* = 23.4, 7.6 Hz, 2F), -157.4 – -157.5 (m, 2F), -161.29 (td, *J* = 24.5, 7.6 Hz, 2F), -163.90 (td, *J* = 22.7, 7.9 Hz, 2F); ^{13}C NMR (176 MHz, CD_2Cl_2, TMS) δ (ppm) = 162.6 (C!), 161.3 (C!), 156.7 (C_A), 156.8 – 156.4 (C!), 156.2 (C_B), 151.7 – 150.3 (C!), 139.9* (C_{mesAr}), 135.9 – 135.5 ($C_{4 \times mesAr}$), 132.5* (C_{mesAr}), 132.2 (C!), 131.0 (C!), 129.7 – 129.5 ($C_{4 \times mesAr}$), 126.4 (C_B), 125.2 (C_A), 120.8 (C_A), 119.8 (C_B), 118.6 (C_{C+D}), 108.0 – 107.5 (C!), 105.6 – 105.4 (C!), 20.9* (C_{mesMe}), 18.0 (C_{mesMe}), 17.3 (C_{mesMe}), 16.5* (C_{mesMe}).

Minor diastereomer: ^{1}H NMR (700 MHz, CD_2Cl_2, TMS) δ (ppm) = 7.57 (d, *J* = 1.5 Hz, $2H_A$), 7.21 (s, $2H_{mesAr}$), 7.09 (d, *J* = 1.5 Hz, $2H_A$), 7.09 – 7.05 (m, $6H_{3 \times mesAr}$), 7.04 (d, *J* = 1.5 Hz, $2H_B$), 6.98 (d, *J* = 1.5 Hz, $2H_B$), 6.18 – 6.05 (m, $8H_{2 \times C, 2 \times D}$), 5.80 – 5.77 (m, $2H_D$), 5.71 (dd, *J* = 10.1, 2.6 Hz, $2H_C$), 2.43 (s, $6H_{mesMe}$), 2.40 (s, $6H_{mesMe}$), 2.35 (s, $6H_{mesMe}$), 2.05 (s, $6H_{mesMe}$), 2.01 (s, $6H_{mesMe}$), 1.99 (s, $6H_{mesMe}$); ^{19}F NMR (376 MHz, CD_2Cl_2) δ (ppm) = -113.33 (s, 2F), -113.46 (s, 2F), -140.57 (dd, *J* = 24.2, 6.8 Hz, 2F), -143.33 (dd, *J* = 23.0, 6.0 Hz, 2F), -157.4 – -157.5 (m, 2F), -160.83 (td, *J* = 24.7, 8.0 Hz, 2F), -164.37 (td, *J* = 21.4, 7.3 Hz, 2F); ^{13}C NMR (176 MHz, CD_2Cl_2, TMS) δ (ppm) = 162.6 (C!), 161.3 (C!), 156.8 – 156.4 (C!), 156.7 (C_A), 156.4 (C_B), 151.7 – 150.3 (C!), 139.2* (C_{mesAr}), 135.9 – 135.5 ($C_{4 \times mesAr}$), 132.5* (C_{mesAr}), 132.2 (C!), 131.0 (C!), 129.7 – 129.5 ($C_{4 \times mesAr}$), 126.4 (C_A), 125.2 (C_B), 120.4 (C_A), 120.1 (C_B), 118.6 (C_D), 118.1 (C_C), 108.0 – 107.5 (C!), 105.6 – 105.4 (C!), 20.9* (C_{mesMe}), 18.0 (C_{mesMe}), 17.3 (C_{mesMe}), 16.8 (C_{mesMe}), 11.9 (C_{mesMe}).

Due to poor solubility in organic solvents and extensive coupling to ^{19}F nuclei, some quaternary ^{13}C environments were not observed. As many of the signals corresponding to rings C and D heavily overlap in the ^{1}H NMR spectrum of the diastereomeric mixture, their ^{13}C environments could not be unambiguously assigned to a ring or diastereomer. Such signals/ regions are labelled "!". All signals that could be clearly identified in the ^{13}C, ^{1}H–^{13}C HSQC and ^{1}H–^{13}C HMBC NMR spectra are reported. Single crystals suitable for X-ray diffraction were grown by vapour diffusion of hexane into a DCM solution of the complex.

Complex 8. Prepared according to the general procedure, complex **8** was obtained as a tan powder (334 mg, 0.17 mmol, 47%). The flash chromatography eluent was gradient 9:1–4:6 *n*-hexane/ DCM sat. K_2CO_3 v/v. During precipitation the compound gelled, implying a propensity to interact with DCM. This is evident from the CHN result and residual DCM observed in the ^{1}H NMR spectrum of the complex after drying. **8** was obtained as a diastereomeric mixture in a *ca.* 1:0.9 ratio. MS (MALDI–TOF): *m/z* 1992.1 [M^+]. Calcd. for $C_{86}H_{60}F_{18}Ir_2N_{10}O_2^+$: 1992.4; Anal. Calcd. for $C_{86}H_{60}F_{18}Ir_2N_{10}O_2$: C, 51.86; H, 3.04; N, 7.03, Calcd. for $C_{86}H_{60}F_{18}Ir_2N_{10}O_2{\cdot}1CH_2Cl_2$: C, 50.31; H, 3.01; N, 6.74. Found: C, 50.31; H, 2.92; N, 6.79.

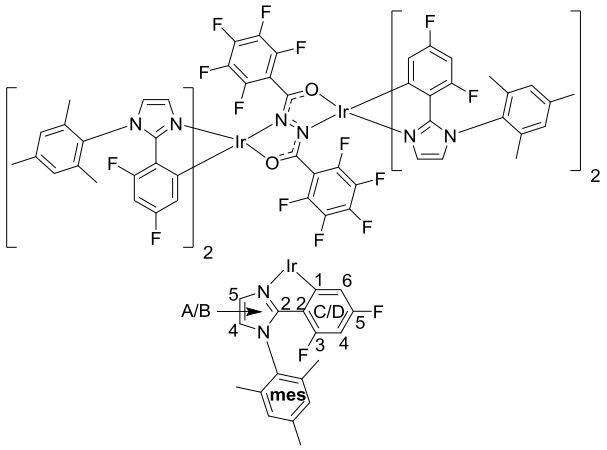

Major diastereomer: ^{1}H NMR (700 MHz, THF-d_8) δ (ppm) = 7.66 (d, *J* = 1.5 Hz, 2H_{A5}), 7.31 (d, *J* = 1.5 Hz, 2H_{A4}), 7.25 (d, *J* = 1.6 Hz, 2H_{B5}), 7.11 (d, *J* = 2.0 Hz, 2H_{mesAr}), 7.09 (d, *J* = 1.6 Hz, 2H_{B4}), 7.00 (bs, 4H_{mesAr}), 6.99 (s, 2H_{mesAr}), 6.01 (ddd, *J* = 11.3, 8.9, 2.4 Hz, 2H_{D4}), 5.96 (ddd, *J* = 11.5, 9.0, 2.4 Hz, 2H_{C4}), 5.64 (dd, *J* = 9.0, 2.4 Hz, 2H_{D6}), 5.58 (dd, *J* = 9.1, 2.4 Hz, 2H_{C6}), 2.39 (s, 6H_{mesMe}), 2.37 (s, 6H_{mesMe}), 2.34 (s, 6H_{mesMe}), 2.04 (s, 6H_{mesMe}), 2.02 –2.00 (m, 12H_{mesMe}); ^{19}F{^{1}H} NMR (376 MHz, THF-d_8) δ (ppm) = -105.78 (d, *J* = 7.9 Hz, 2F), -106.45 – -106.55 (m, 2F), -112.32 (d, *J* = 7.9 Hz, 2F), -112.70 – -112.80 (m, 2F), -141.07 (dd, *J* = 24.4, 6.4 Hz, 2F), -143.23 (dd, *J* = 24.4, 7.1 Hz, 2F), -158.18 – -158.28 (m, 2F), -162.45 (td, *J* = 24.3, 7.4 Hz, 2F), -164.82 (td, *J* = 22.0, 21.5, 7.1 Hz, 2F); ^{13}C NMR (176 MHz, THF-d_8) δ (ppm) = 164.3 (d, *J* = 250 Hz, C_{D5}), 164.0 (d, *J* = 250 Hz, C_{C5}), 159.0 (d, *J* = 247 Hz, C_{C3}), 158.2 (C_{A2}), 158.0 (d, *J* = 264 Hz, C_{D3}) 157.5 (C_{B2}), 140.5* (C_{mesAr}), 137.7 (C_{mesAr}), 137.6 (C_{mesAr}), 137.5 (C_{mesAr}), 137.0* (C_{mesAr}), 136.7 (C_{mesAr}), 130.6 (C_{mesAr}), 130.3 (C_{mesAr}), 130.2 (C_{mesAr}), 130.1 (C_{mesAr}), 128.4 (C_{A5}), 127.3 (C_{B4}), 124.1 (C_{A4}), 123.7 (C_{B5}), 121.0 (C_{D2}), 120.0 (C_{C2}), 116.3 (d, *J* = 16.9 Hz, C_{D6}), 116.0 (d, *J* = 16.7 Hz, C_{C6}), 98.0 (t, *J* = 25 Hz, C_{D4}), 96.2 (t, *J* = 25 Hz, C_{C4}), 22.0* (C_{mesMe}), 19.1 (C_{mesMe}), 18.5 (C_{mesMe}), 18.4 (C_{mesMe}), 18.2 (C_{mesMe}).

Minor diastereomer: ^{1}H NMR (700 MHz, THF-d_8) δ (ppm) = 7.56 (d, *J* = 1.5 Hz, 2H_{A5}), 7.51 (d, *J* = 1.7 Hz, 2H_{B5}), 7.39 (d, *J* = 1.5 Hz, 2H_{A4}), 7.17 (d, *J* = 1.7 Hz, 2H_{B4}), 7.12 – 7.10 (m, 2H_{mesAr}), 7.08 (s, 2H_{mesAr}), 7.00 – 6.97 (m, 2H_{mesAr}), 6.97 (s, 2H_{mesAr}), 6.02 – 5.98 (m, 2H_{C4}), 5.96 – 5.92 (m, 2H_{D4}) 5.74 (dd, *J* = 9.2, 2.3 Hz, 2H_{D6}), 5.61 (dd, *J* = 9.0, 2.4 Hz, 2H_{C6}), 2.40 (s, 6H_{mesMe}), 2.28 (s, 6H_{mesMe}), 2.08 (s, 6H_{mesMe}), 2.04 (s, 6H_{mesMe}), 2.02 – 1.99 (m, 6H_{mesMe}), 1.86 (s, 6H_{mesMe}); ^{19}F{^{1}H} NMR (376 MHz, THF-d_8) δ (ppm) = -105.71 (d, *J* = 8.0 Hz, 2F), -106.45 – -106.55 (m, 2F), -111.87 (d, *J* = 8.0 Hz, 2F), -112.70 – 112.80 (m, 2F), -142.25 (dd, *J* = 24.7, 7.7 Hz, 2F), -142.54 (dd, *J* = 24.7, 7.2 Hz, 2F), -158.18 – -158.28 (m, 2F), -162.72 (td, *J* = 23.7, 7.2 Hz, 2F), -164.12 (td, *J* = 23.7, 7.7 Hz, 2F); ^{13}C NMR (176 MHz, THF-d_8) δ (ppm) = 164.4 (d, *J* = 250 Hz, C_{D5}), 164.1 (d, *J* = 250 Hz, C_{C5}), 159.3 (d, *J* = 245 Hz, C_{C3}), 158.3 (d, *J* = 260 Hz, C_{D3}), 157.7 ($C_{A2 + B2}$), 140.6* (C_{mesAr}), 137.9 (C_{mesAr}), 137.6 (C_{mesAr}), 137.5 (C_{mesAr}), 137.0* (C_{mesAr}), 136.7 (C_{mesAr}), 130.5 (C_{mesAr}), 130.4 (C_{mesAr}), 130.3 (C_{mesAr}), 130.2 (C_{mesAr}), 128.5 (C_{B5}), 127.3 (C_{A5}), 124.4 (C_{A4}), 123.6 (C_{B4}), 120.9 (C_{C2}), 120.0 (C_{D2}), 116.3 (d, *J* = 17 Hz, C_{D6}), 116.0 (d, *J* = 16 Hz, C_{C6}), 98.0 (t, *J* = 27 Hz, C_{C4}), 96.0 (t, *J* = 26 Hz, C_{D4}), 21.90* (C_{mesMe}), 19.1 (C_{mesMe}), 18.5 (C_{mesMe}), 18.1 (C_{mesMe}), 17.8 (C_{mesMe}).

Due to poor solubility in organic solvents and extensive coupling to ^{19}F nuclei, some quaternary ^{13}C environments were not observed (bridge carbons, C1 and D1). All signals that could be clearly identified in the ^{13}C, ^{1}H–^{13}C HSQC and ^{1}H–^{13}C HMBC NMR spectra are reported. Single crystals suitable for X-ray diffraction were grown by vapour diffusion of methanol into a THF solution of the complex.

Copies of NMR Spectra

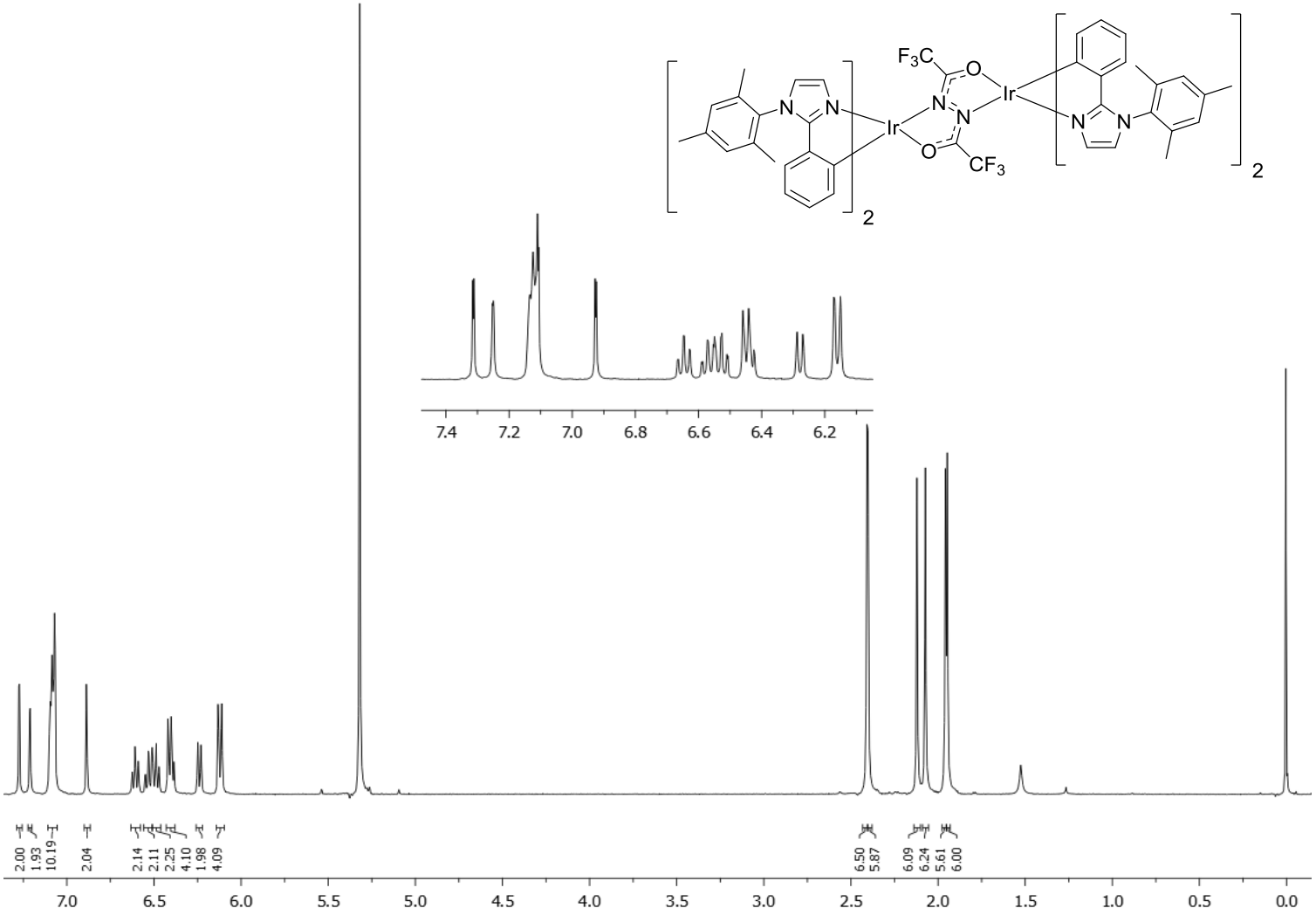

Spectrum S1. ^{1}H NMR spectrum (700 MHz) of **5** in CD_2Cl_2 (TMS).

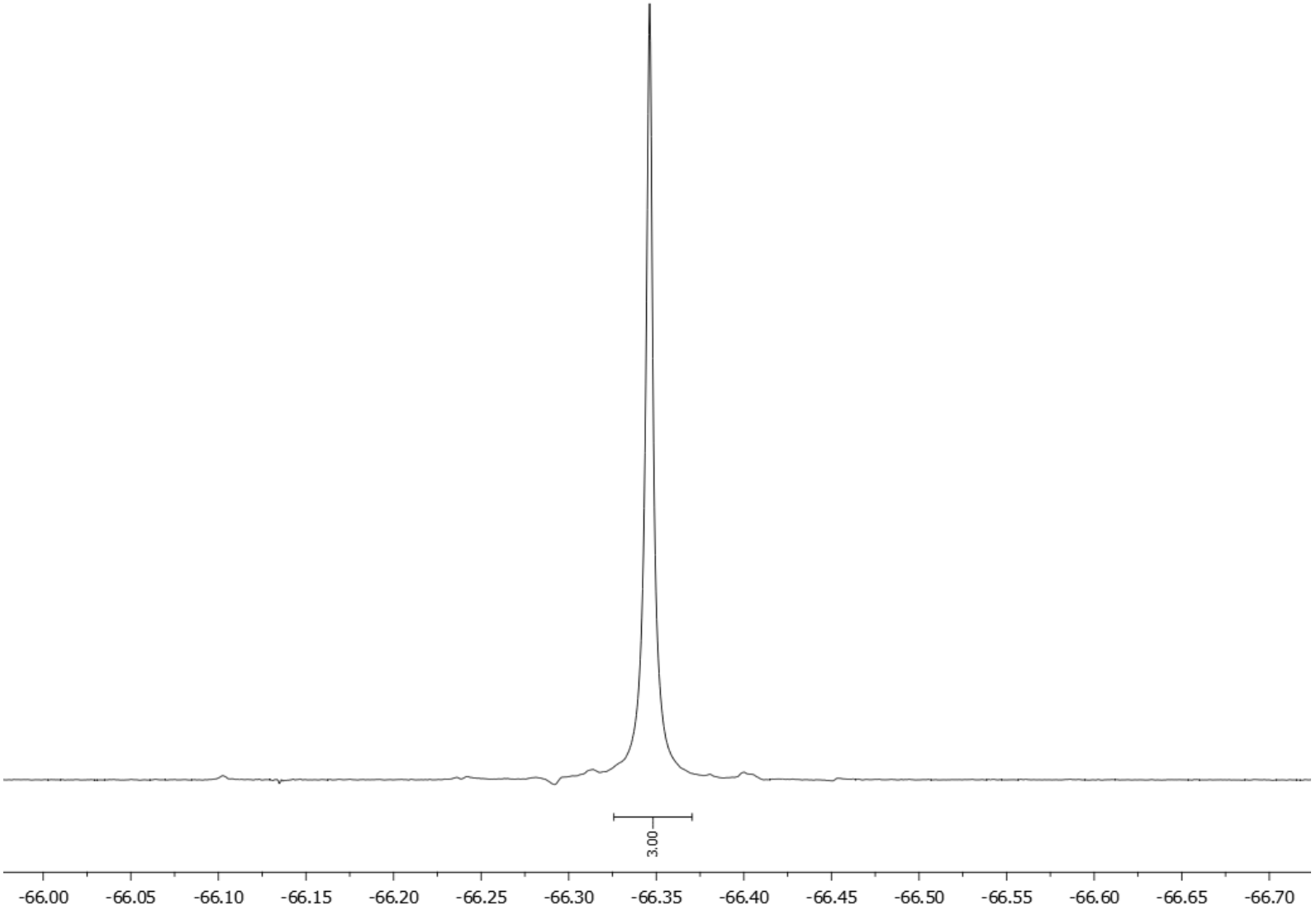

Spectrum S2. $^{19}F\{^{1}H\}$ NMR spectrum (376 MHz) of **5** in CD_2Cl_2.

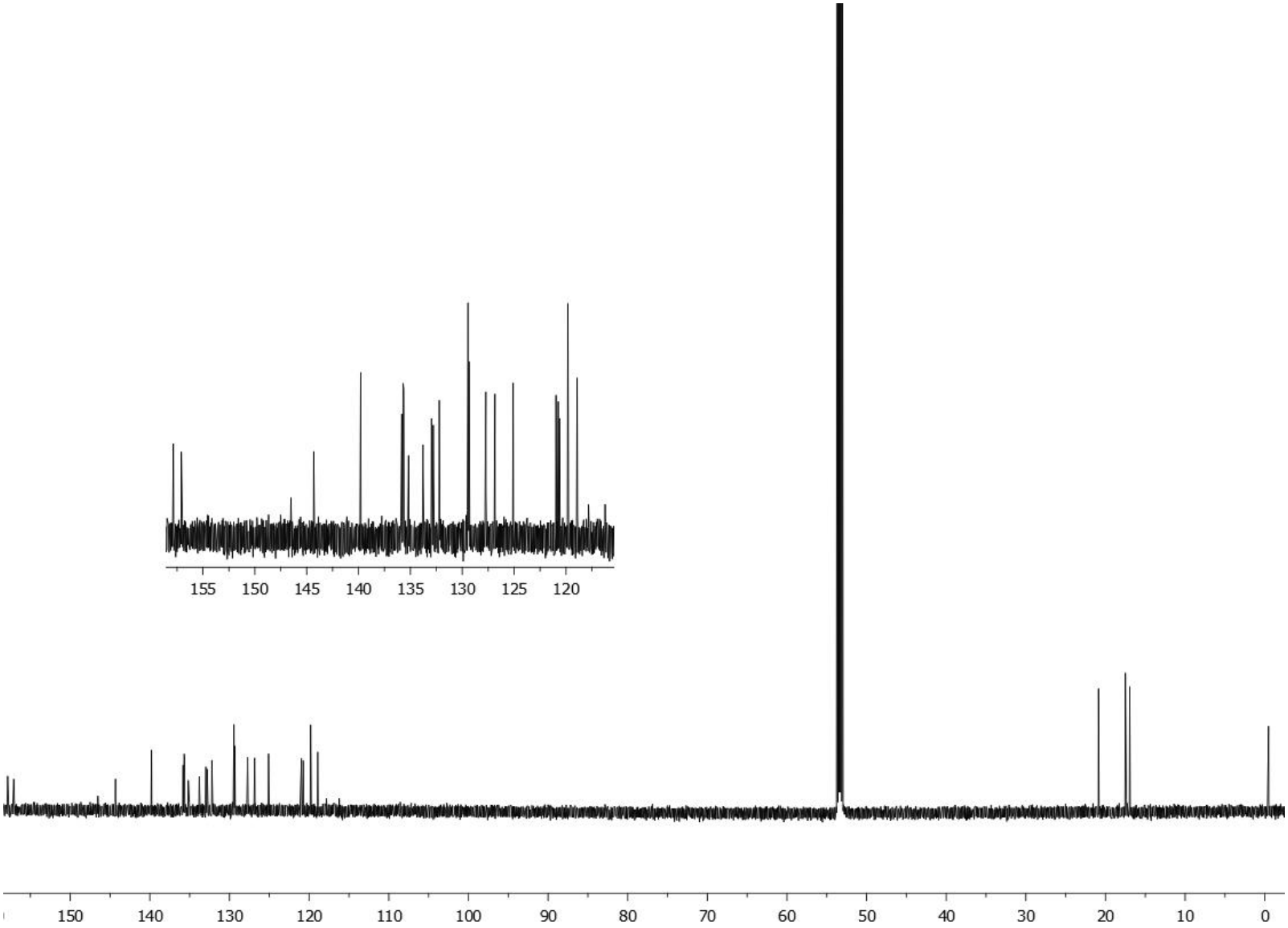

Spectrum S3. ^{13}C NMR spectrum (151 MHz) of **5** in CD_2Cl_2 (TMS).

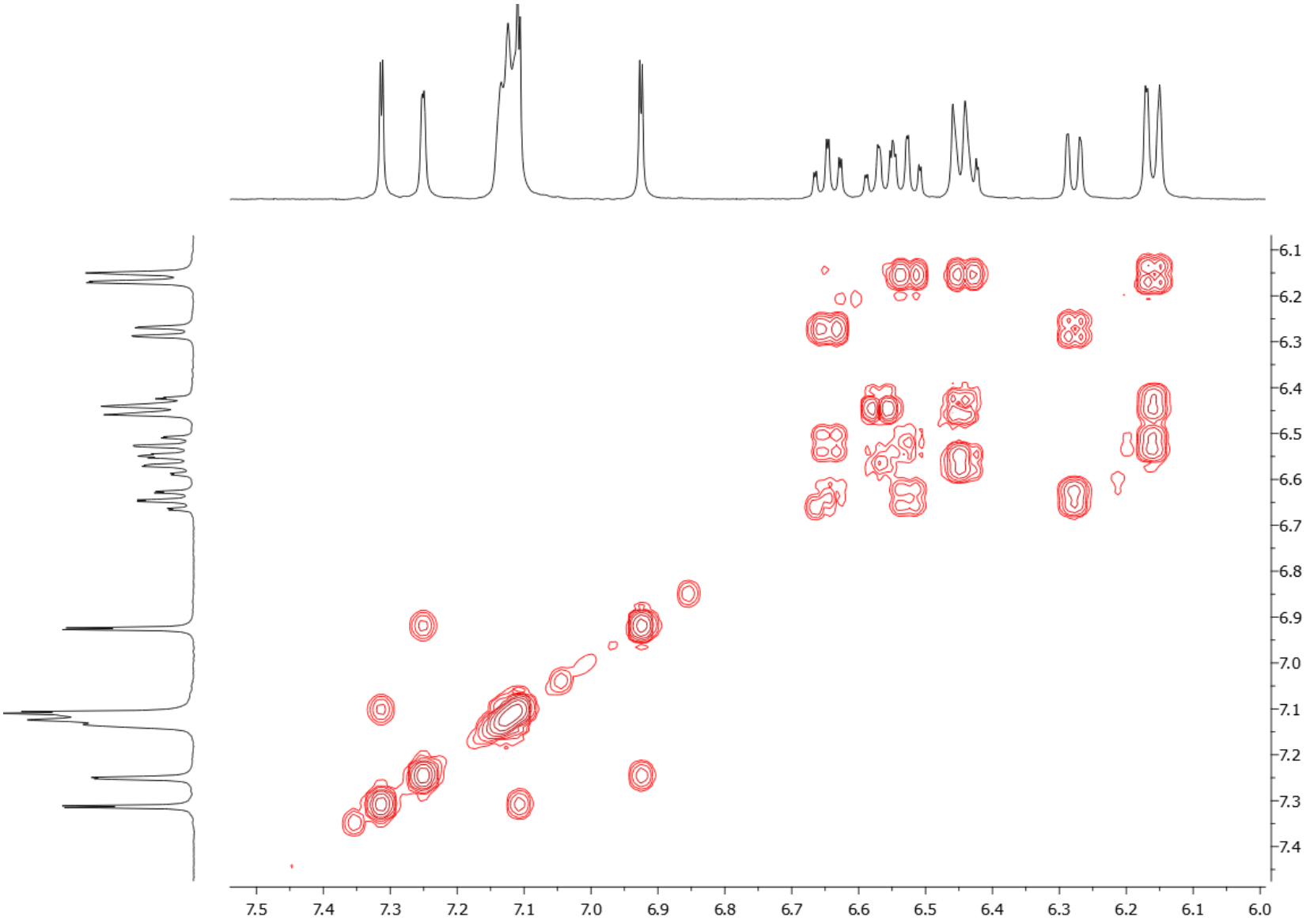

Spectrum S4. Expansion of the aromatic region of the ^{1}H–^{1}H COSY NMR spectrum of **5** in CD_2Cl_2 (TMS).

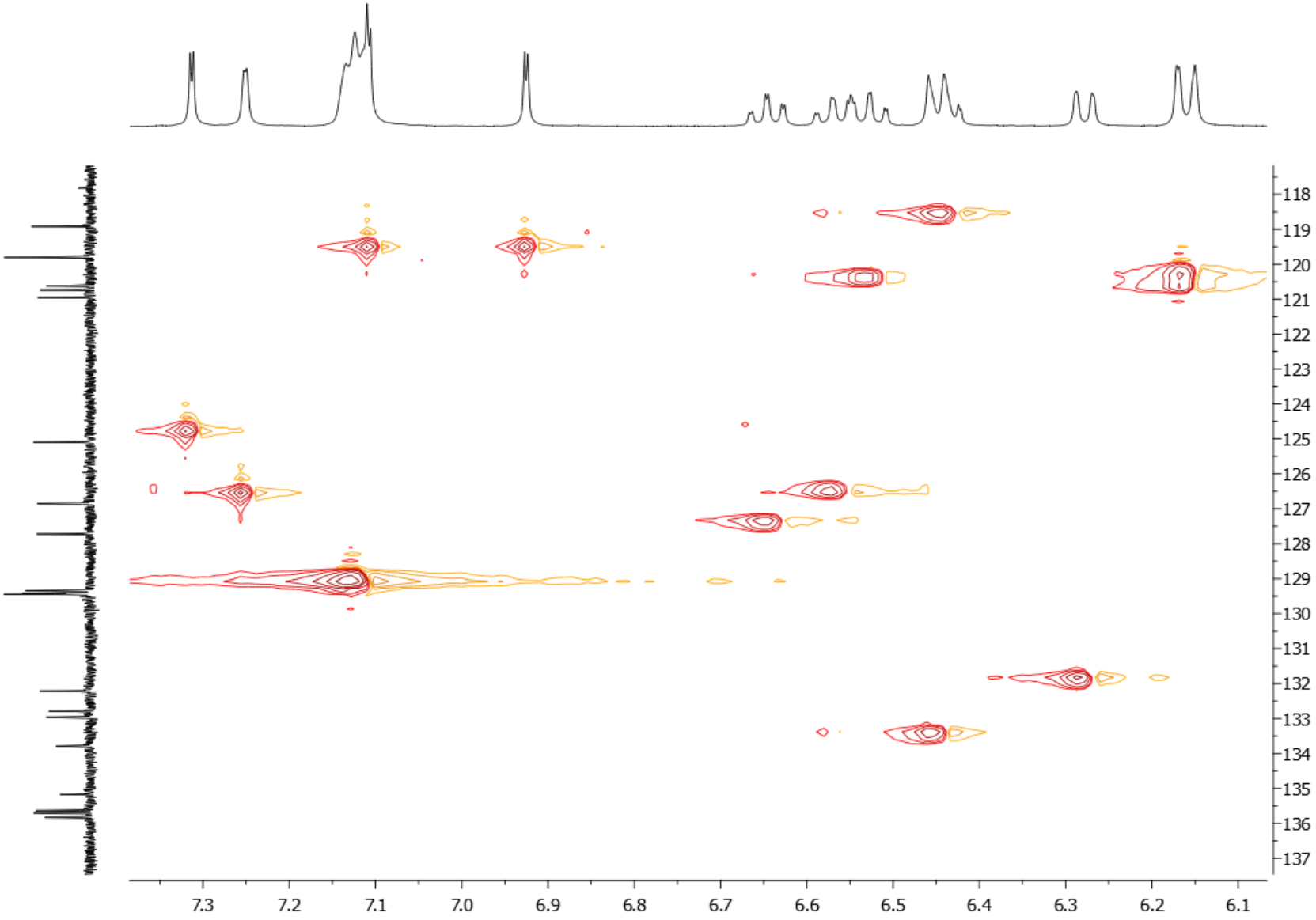

Spectrum S5. Expansion of the aromatic region of the $^{1}H–^{13}C$ HSQC NMR spectrum of **5** in CD_2Cl_2 (TMS).

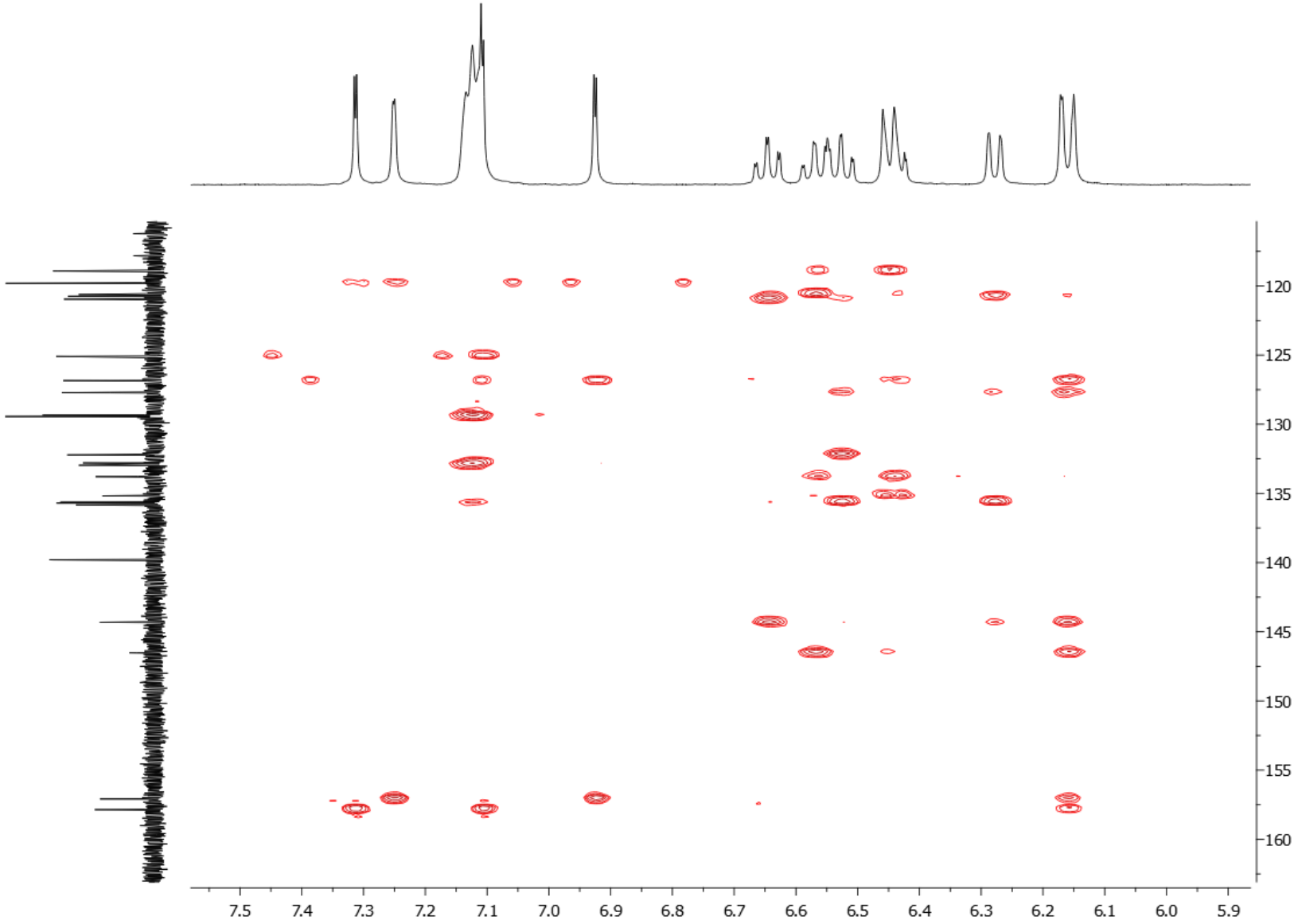

Spectrum S6. Expansion of the aromatic region of the $^{1}H–^{13}C$ HMBC NMR spectrum of **5** in CD_2Cl_2 (TMS).

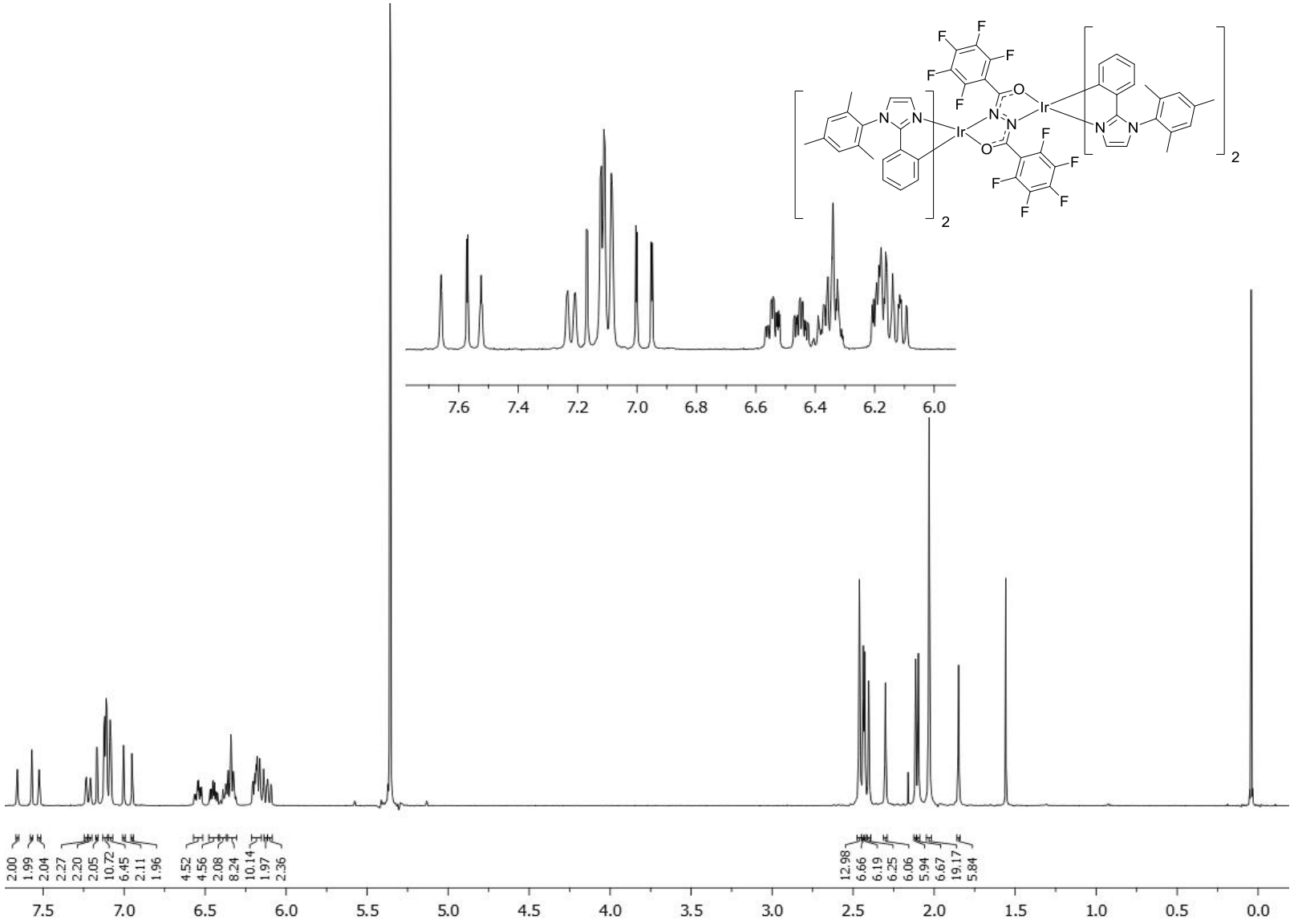

Spectrum S7. ^{1}H NMR spectrum (700 MHz) of **6** in CD_2Cl_2 (TMS).

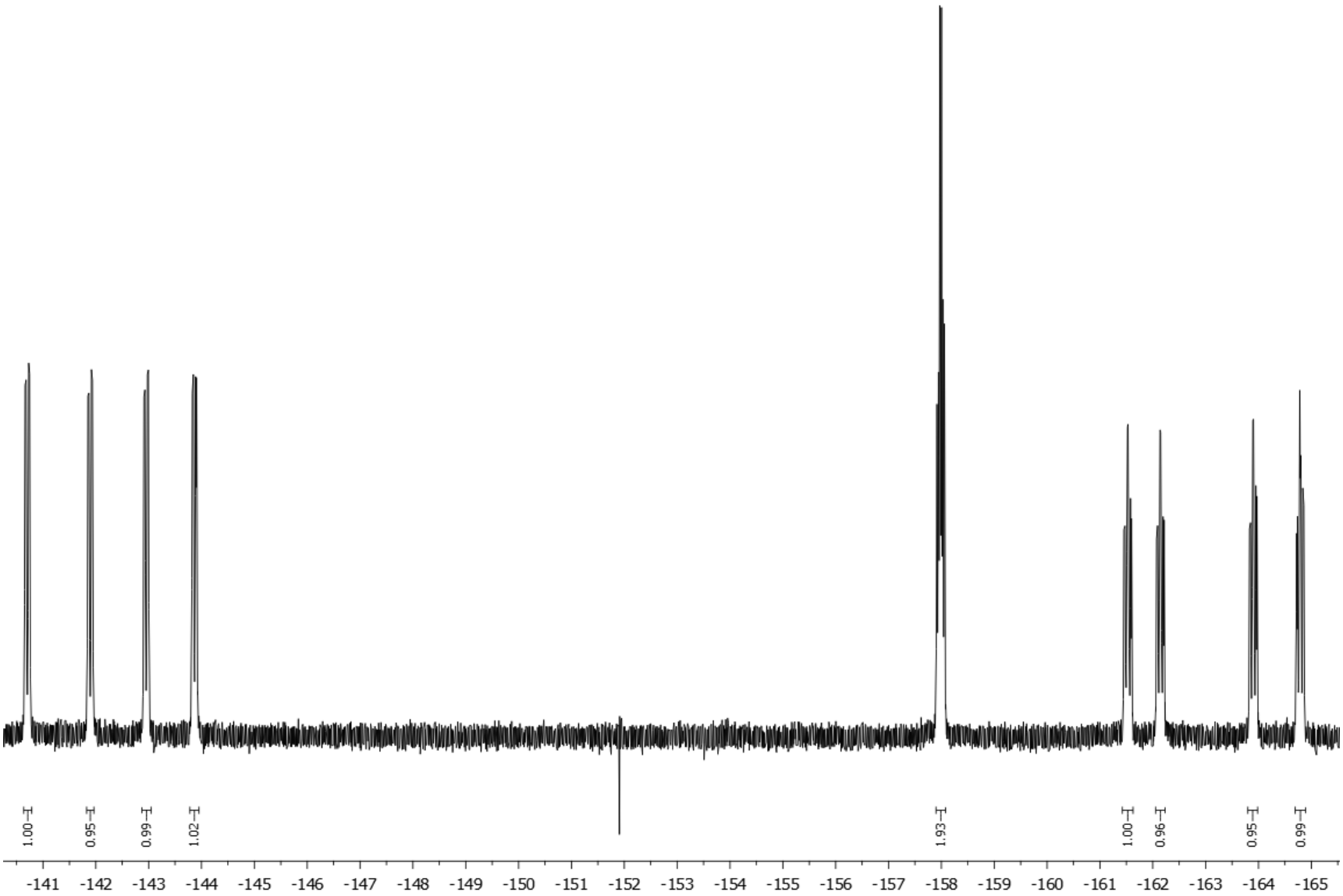

Spectrum S8. $^{19}F\{^{1}H\}$ NMR spectrum (376 MHz) of **6** in CD_2Cl_2.

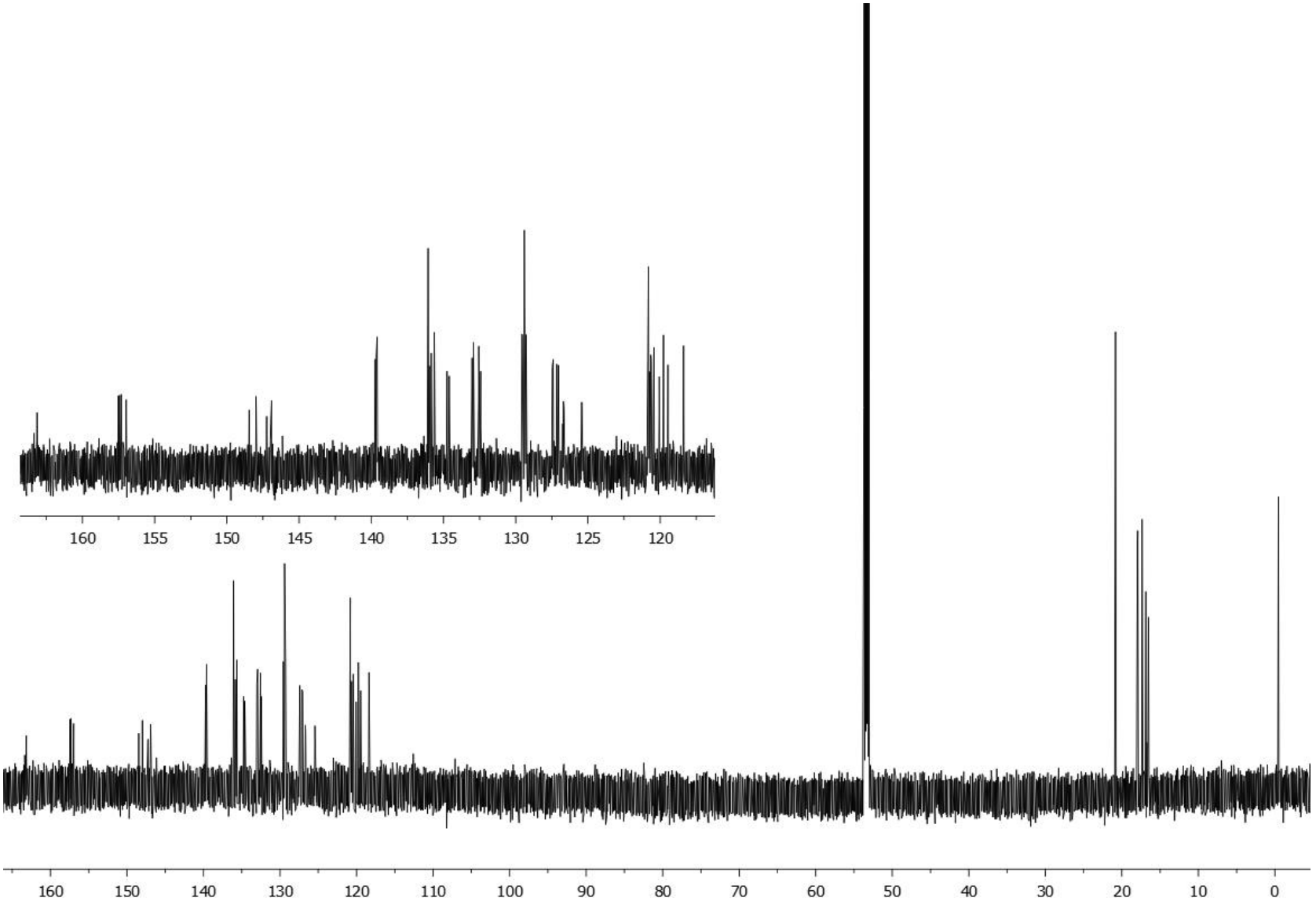

Spectrum S9. ^{13}C NMR spectrum (151 MHz) of **6** in CD_2Cl_2 (TMS).

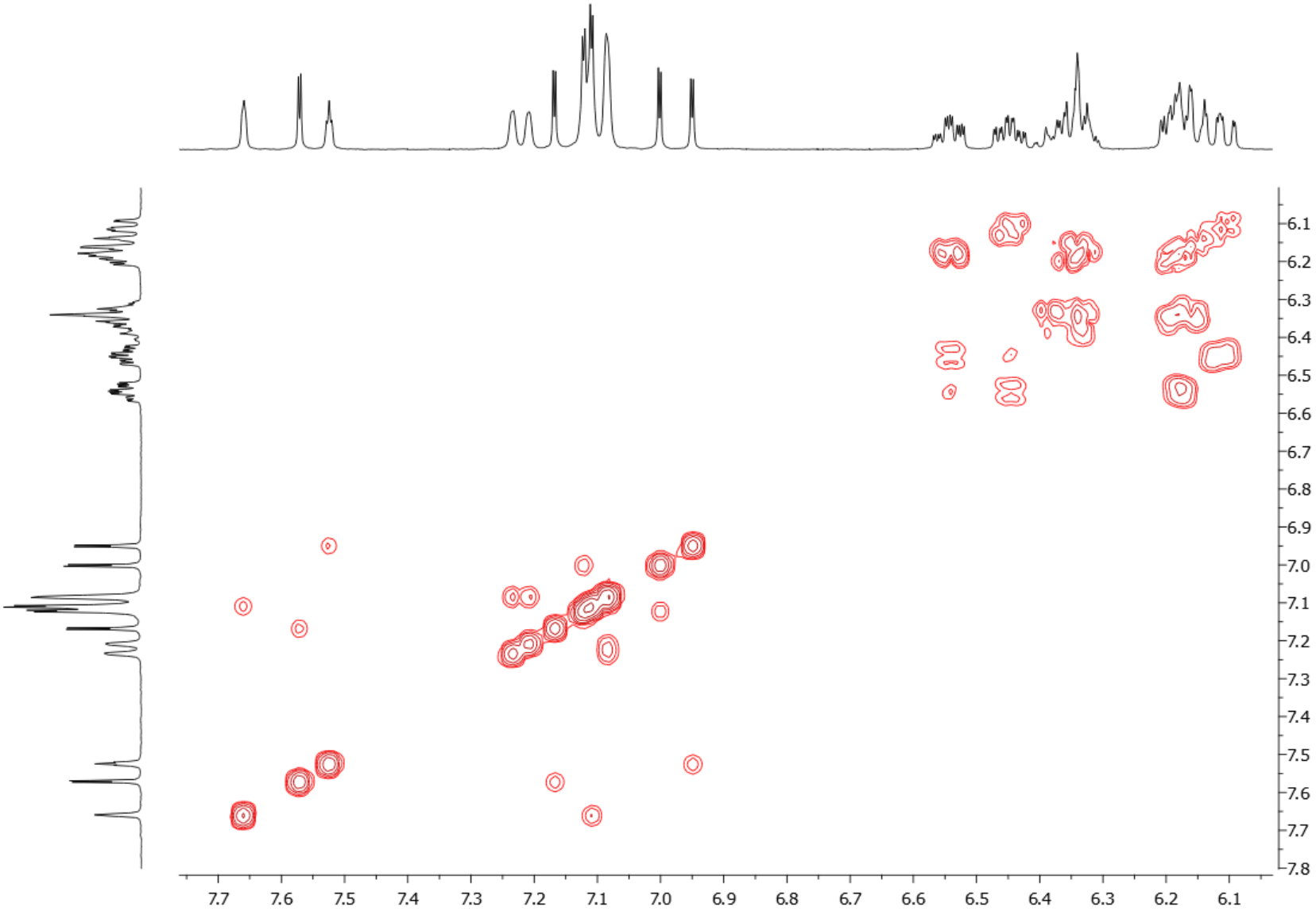

Spectrum S10. Expansion of the aromatic region of the ^{1}H–^{1}H COSY NMR spectrum of **6** in CD_2Cl_2 (TMS).

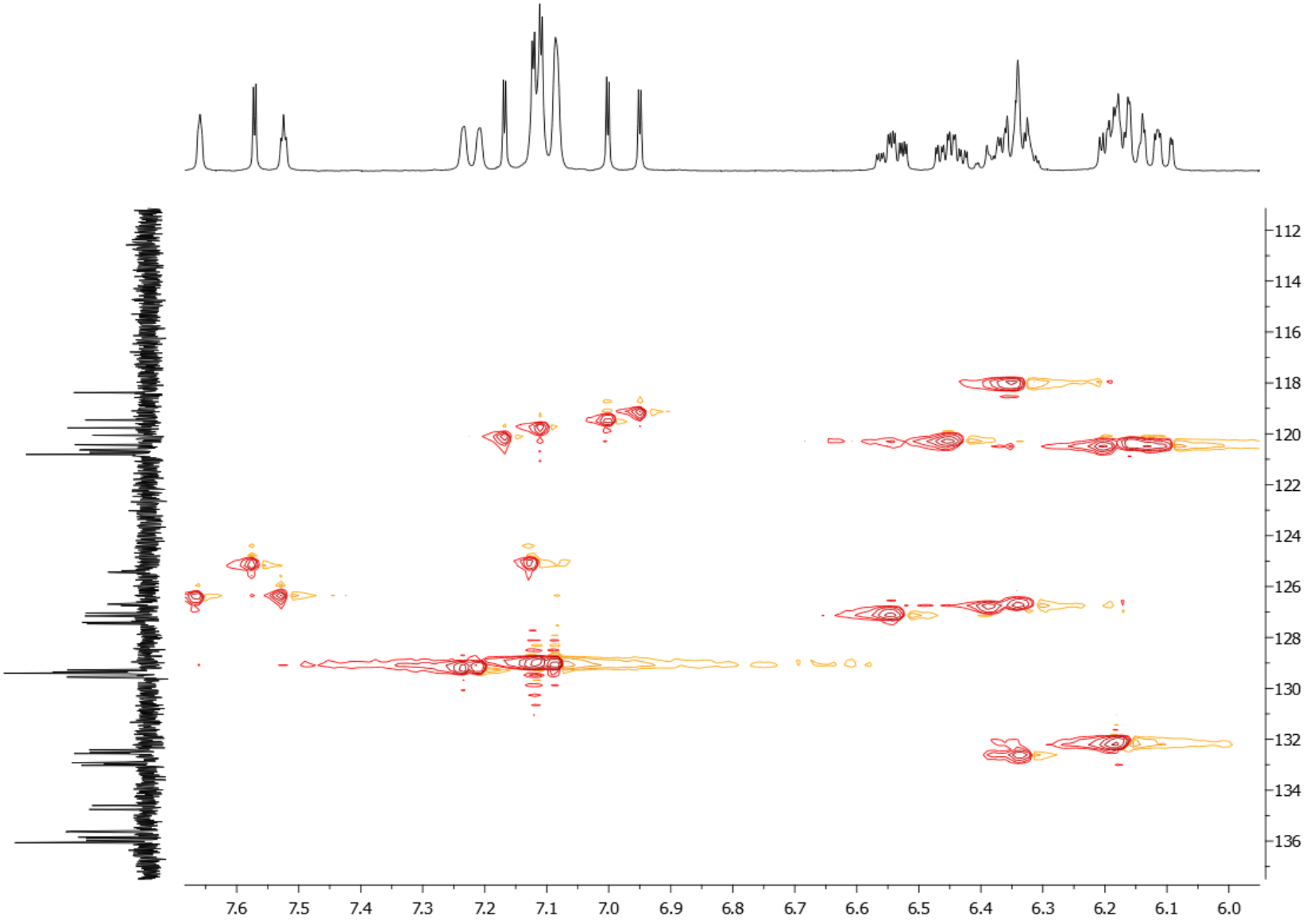

Spectrum S11. Expansion of the aromatic region of the $^{1}H–^{13}C$ HSQC NMR spectrum of **6** in CD_2Cl_2 (TMS).

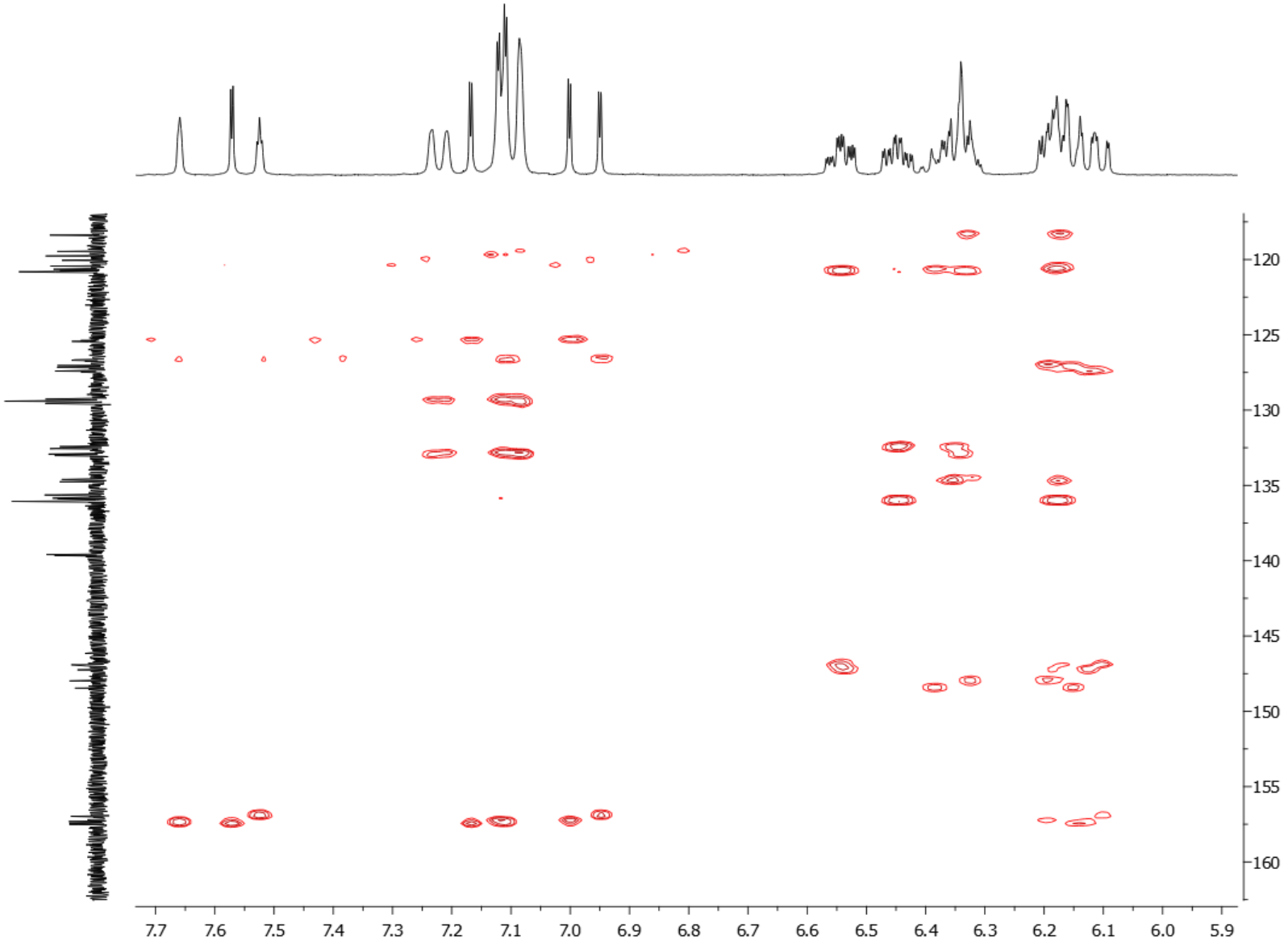

Spectrum S12. Expansion of the aromatic region of the $^{1}H–^{13}C$ HMBC NMR spectrum of **6** in CD_2Cl_2 (TMS).

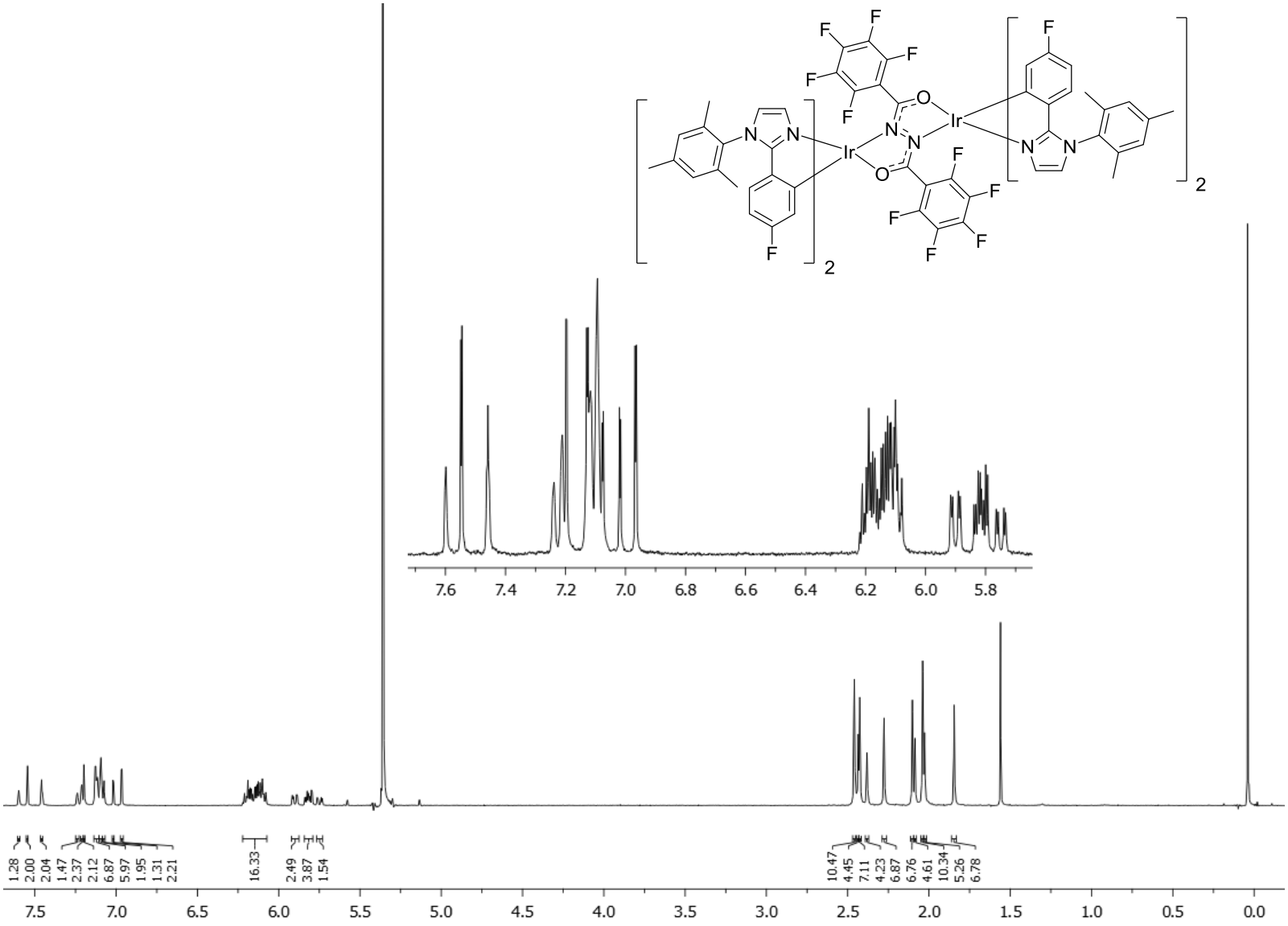

Spectrum S13. ^{1}H NMR spectrum (700 MHz) of **7** in CD_2Cl_2 (TMS).

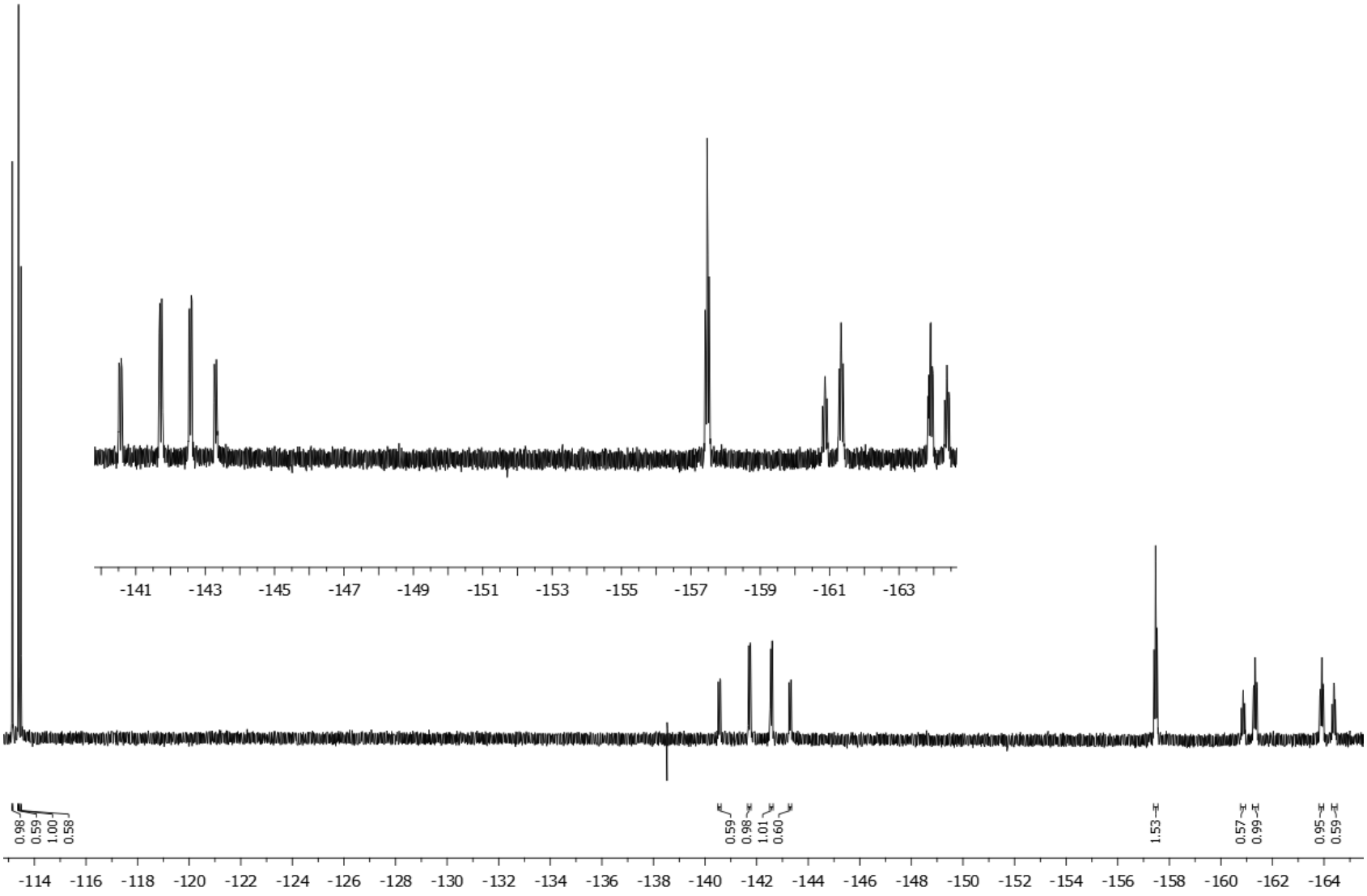

Spectrum S14. $^{19}F\{^{1}H\}$ NMR spectrum (376 MHz) of **7** in CD_2Cl_2.

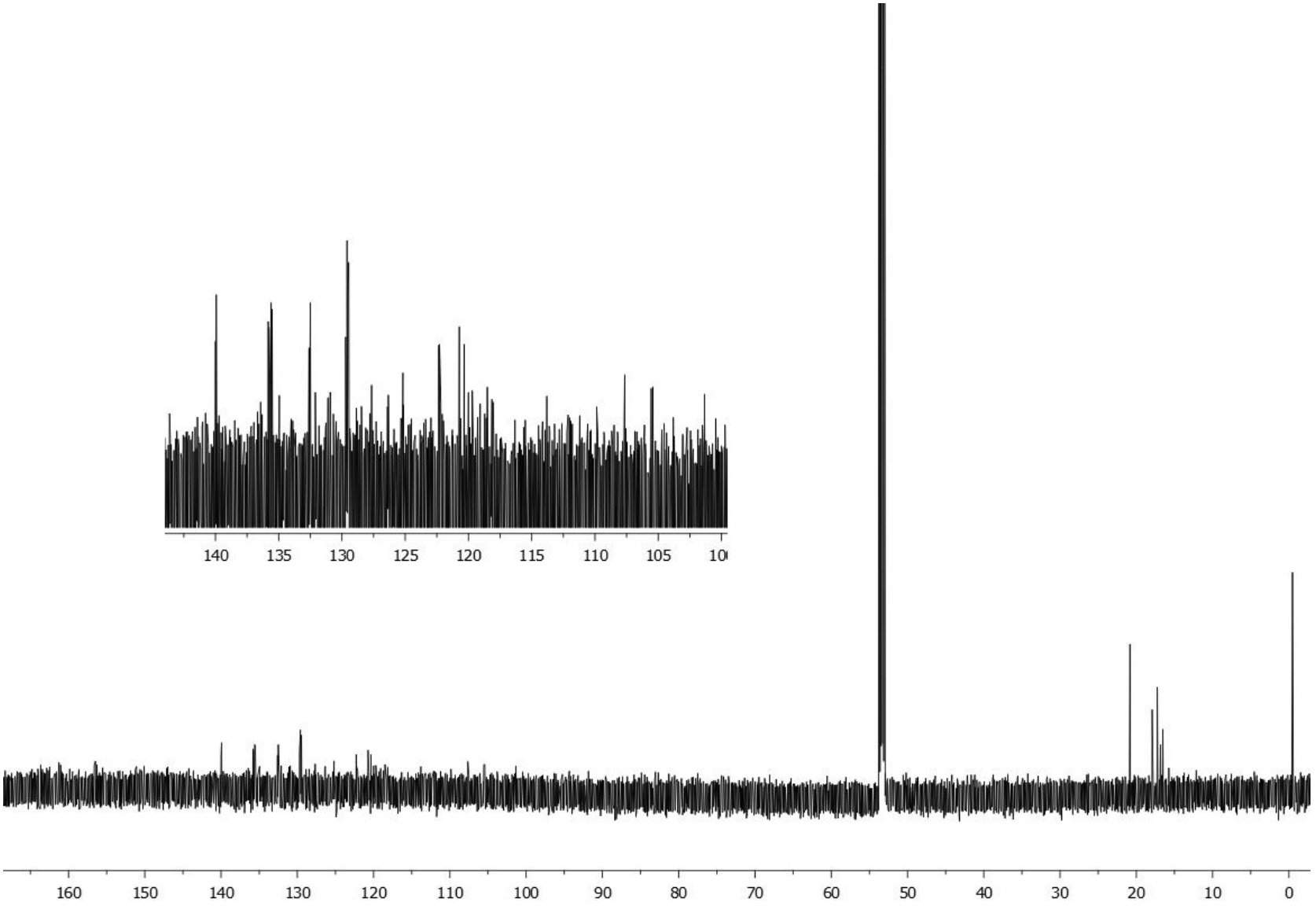

Spectrum S15. ^{13}C NMR spectrum (151 MHz) of **7** in CD_2Cl_2 (TMS).

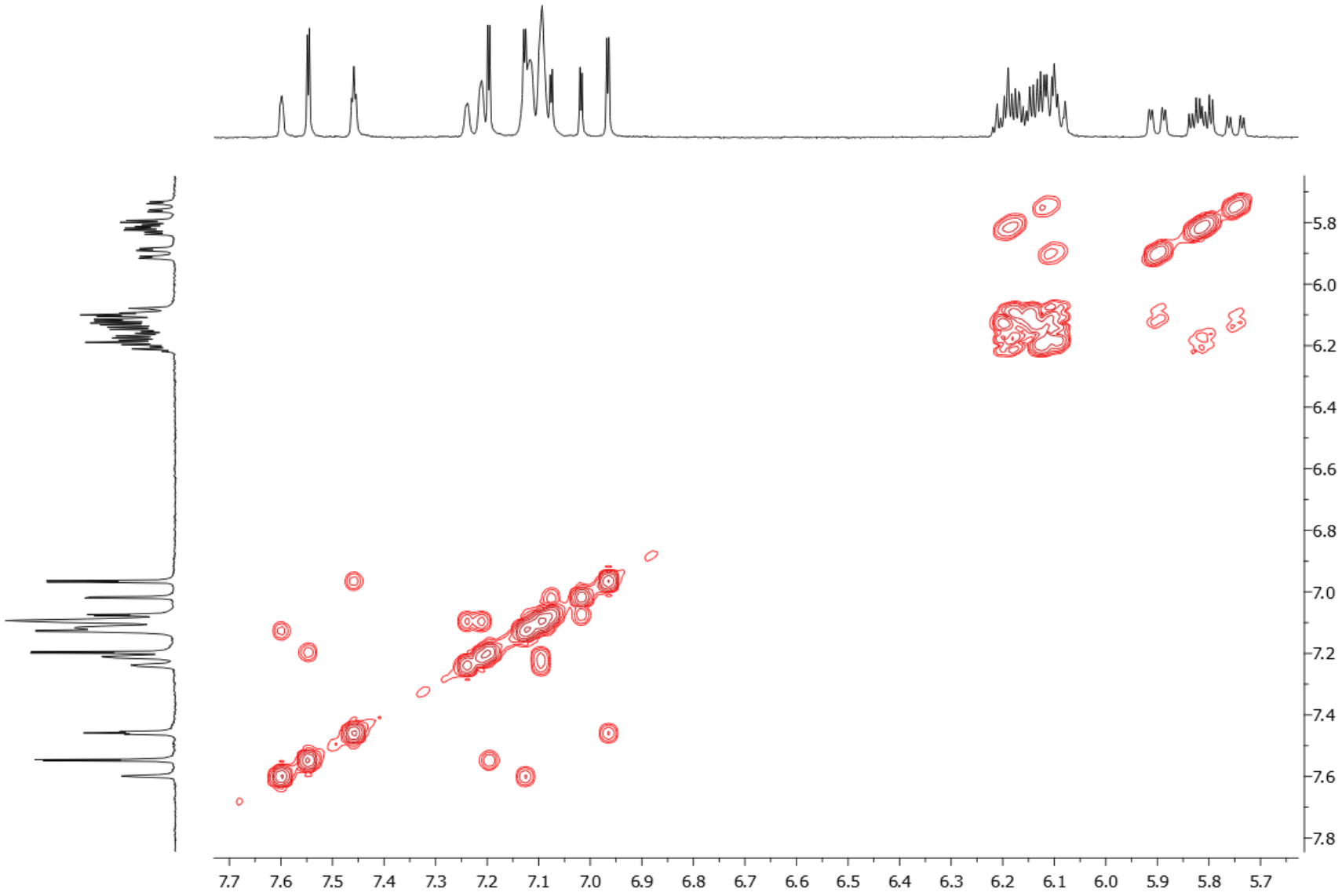

Spectrum S16. Expansion of the aromatic region of the ^{1}H–^{1}H COSY NMR spectrum of **7** in CD_2Cl_2 (TMS).

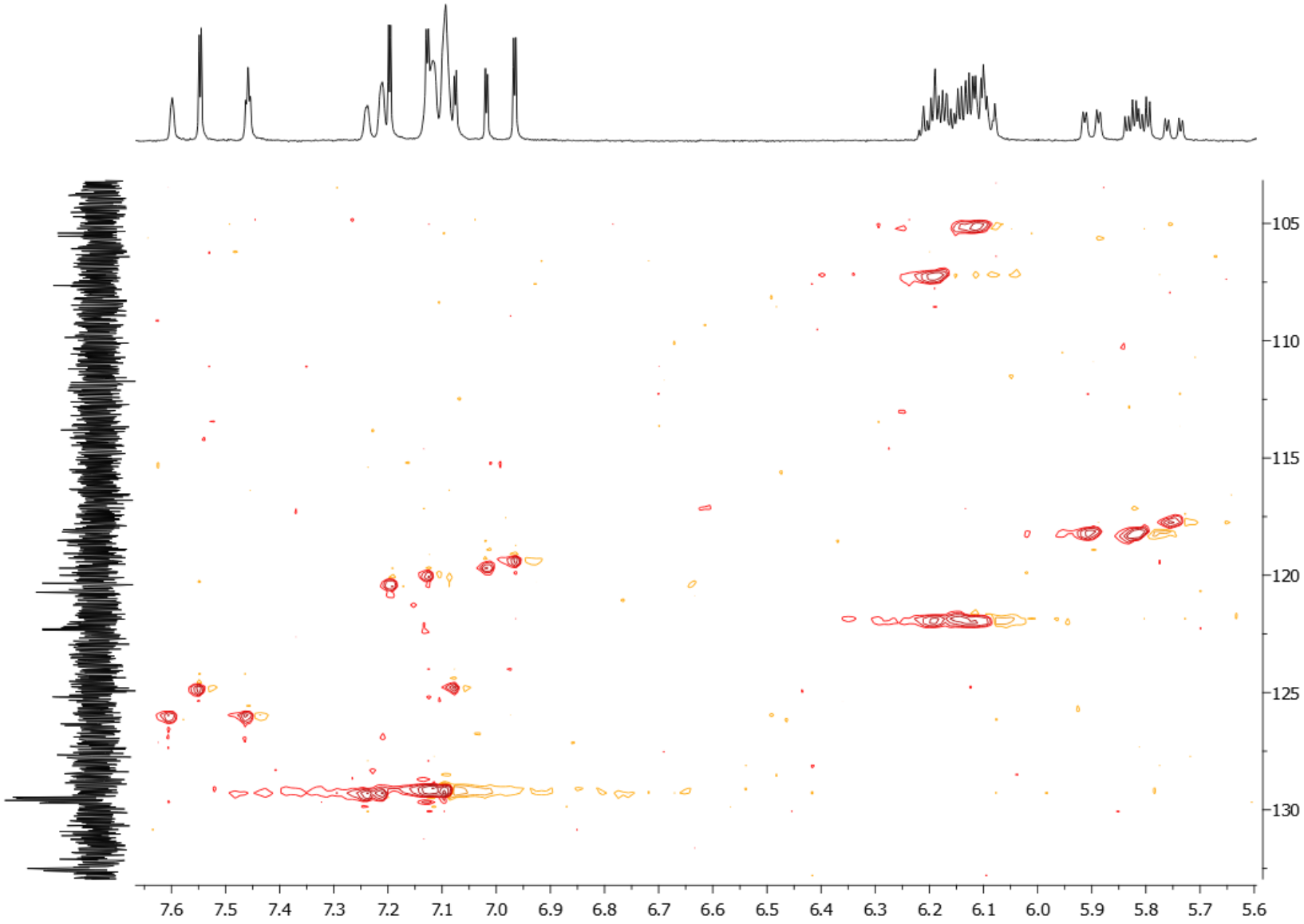

Spectrum S17. Expansion of the aromatic region of the ^{1}H–^{13}C HSQC NMR spectrum of **7** in CD_2Cl_2 (TMS).

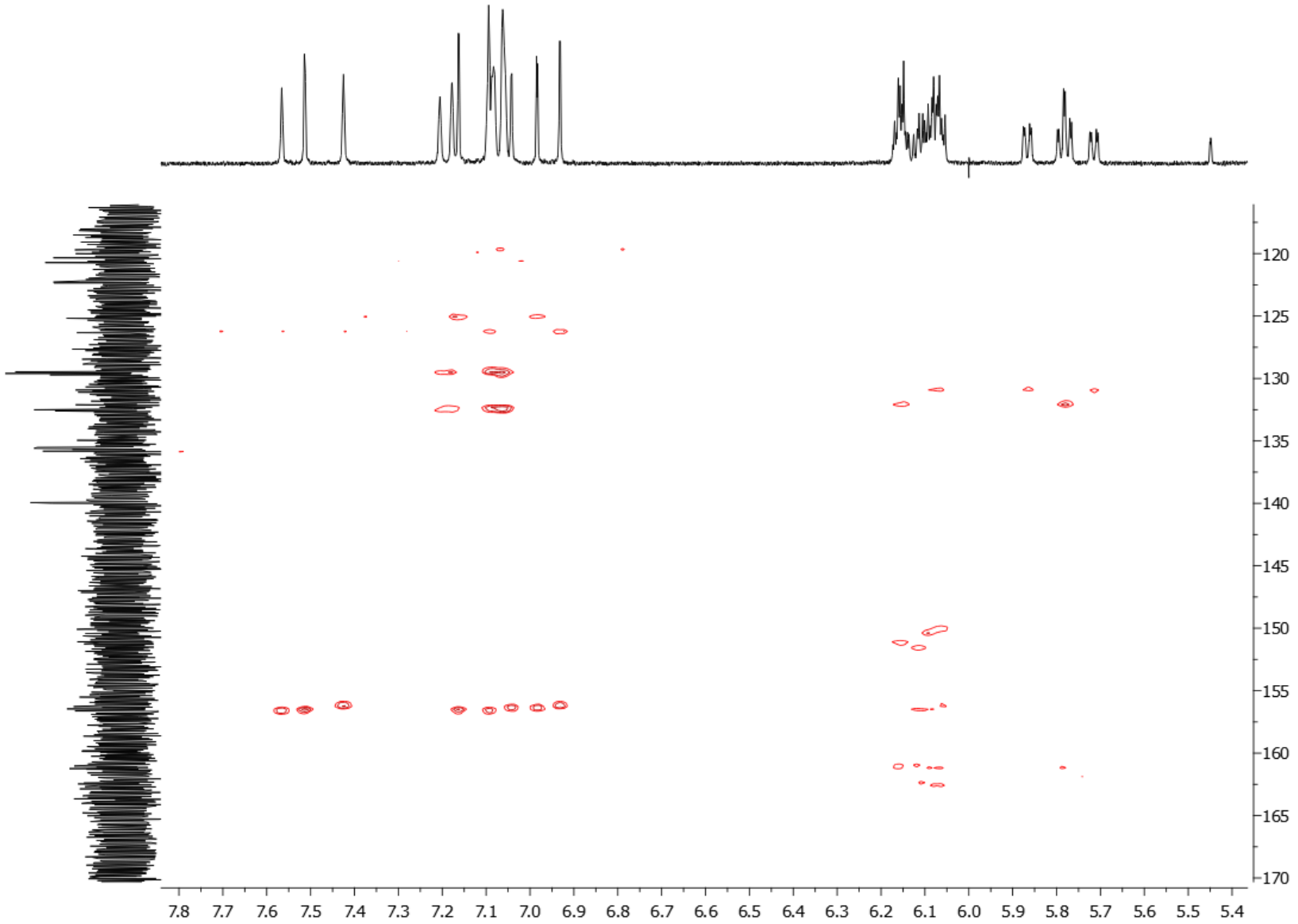

Spectrum S18. Expansion of the aromatic region of the $^{1}H–^{13}C$ HMBC NMR spectrum of **7** in CD_2Cl_2 (TMS).

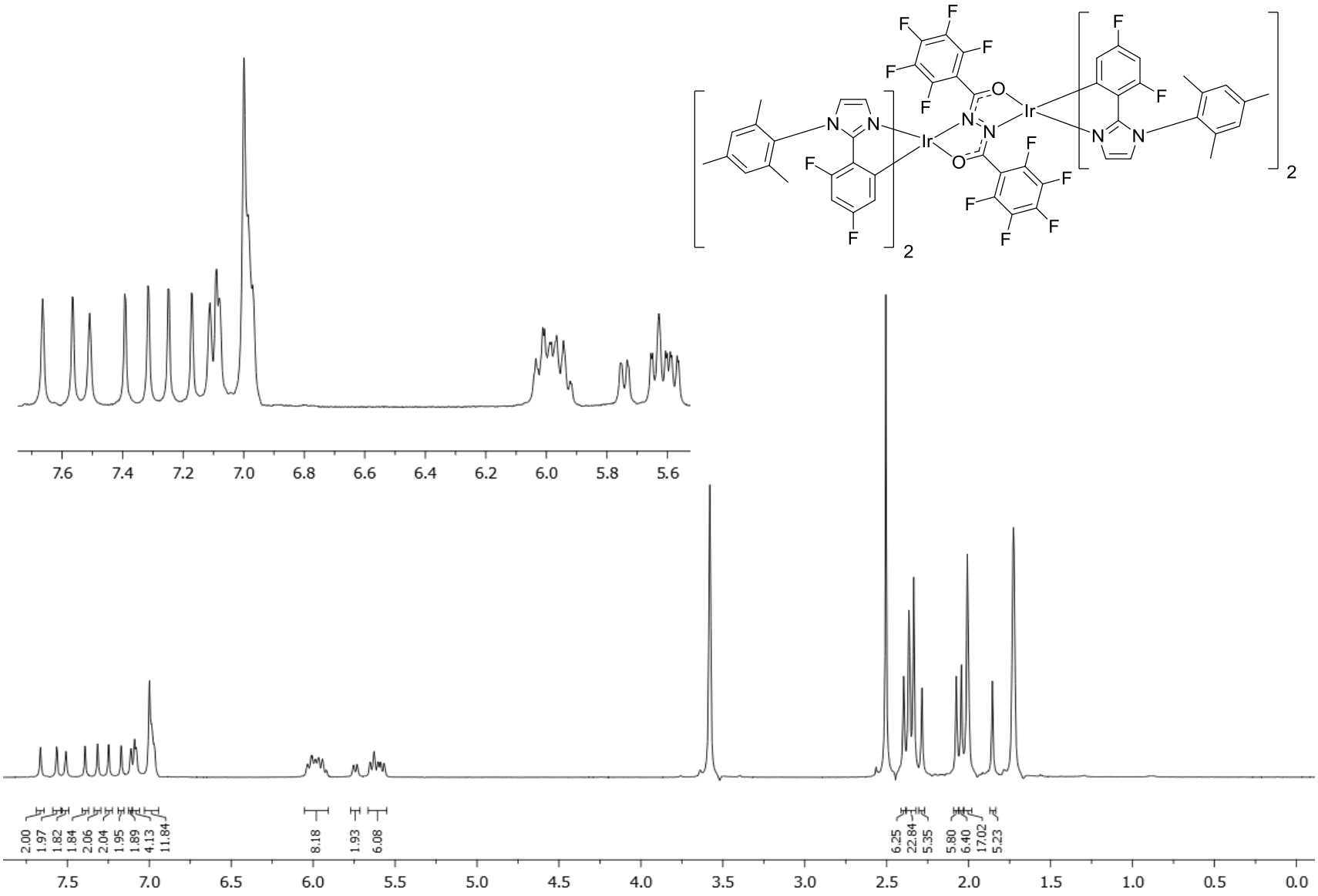

Spectrum S19. ^{1}H NMR spectrum (700 MHz) of **8** in D_8-THF.

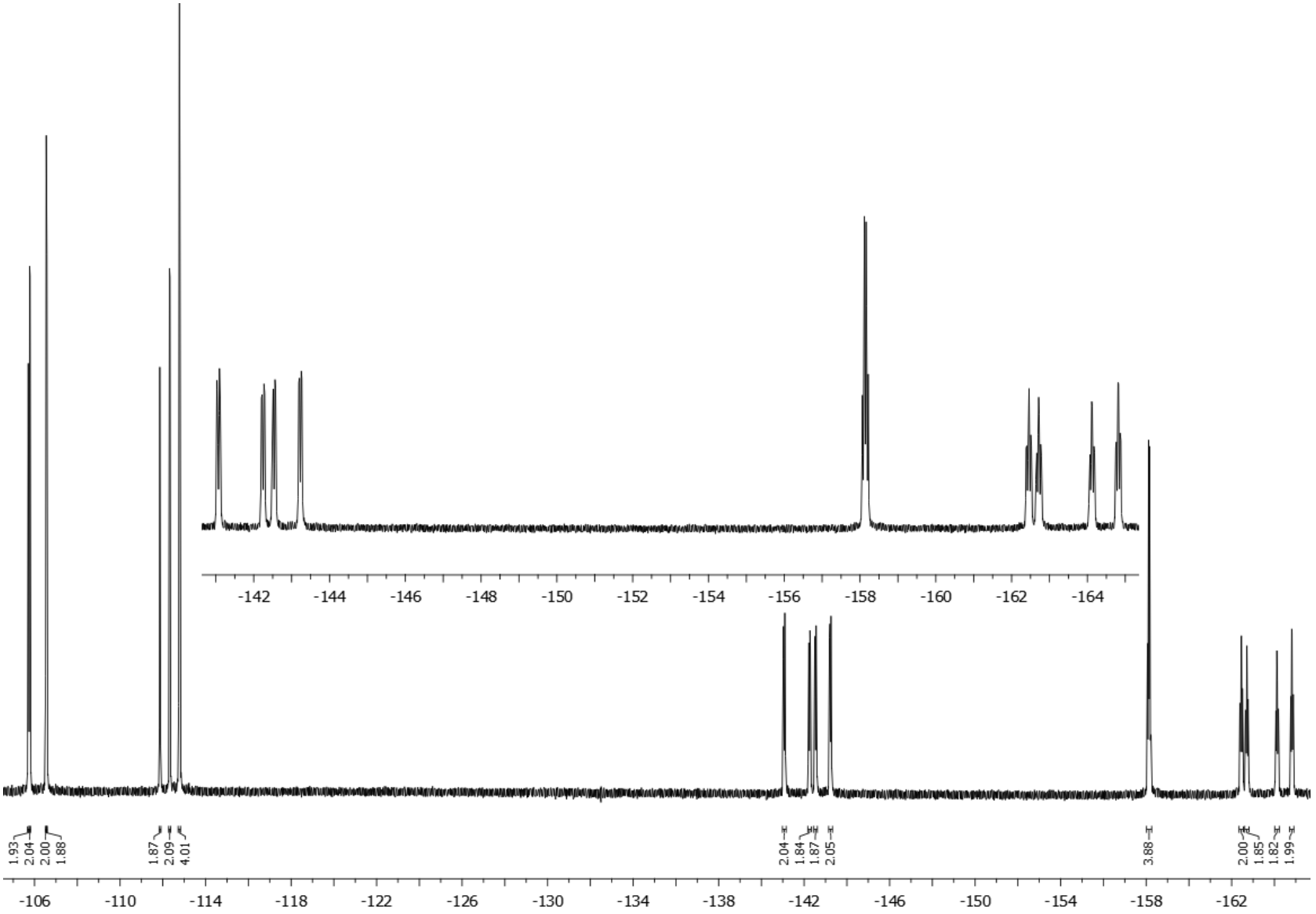

Spectrum S20. $^{19}F\{^{1}H\}$ NMR spectrum (376 MHz) of **8** in D_8-THF.

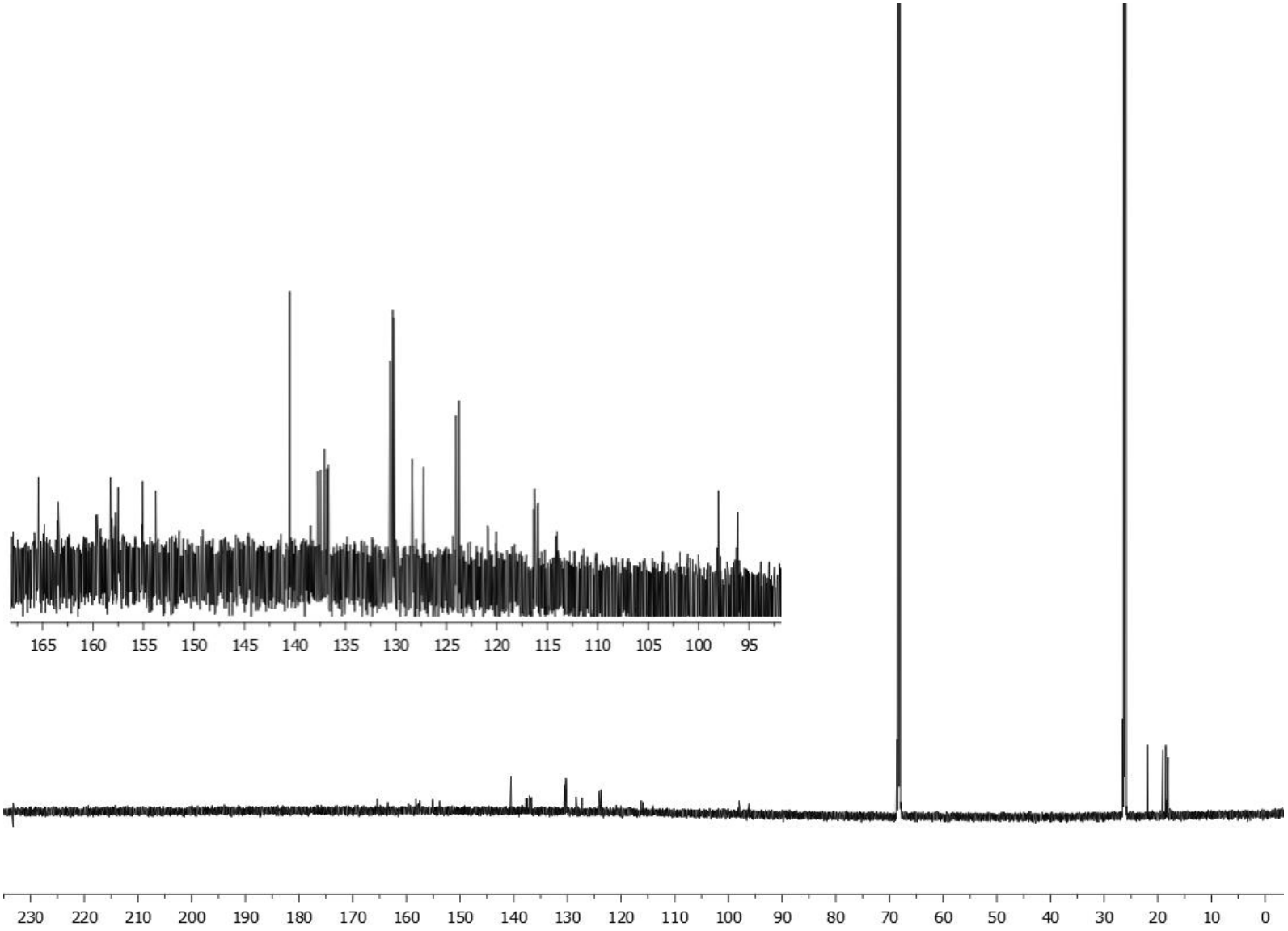

Spectrum S21. ^{13}C NMR spectrum (151 MHz) of **8** in D_8-THF.

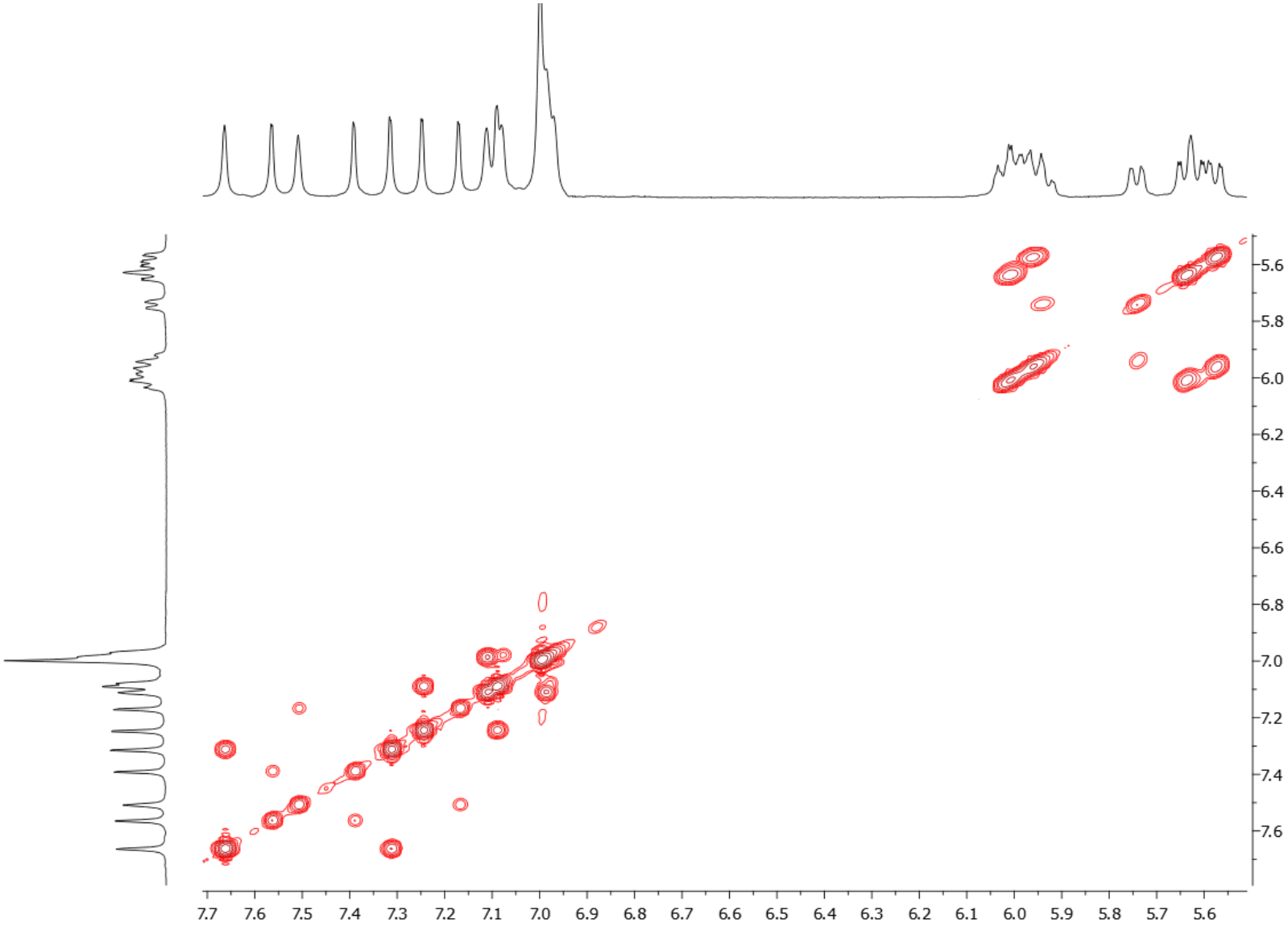

Spectrum S22. Expansion of the aromatic region of the ^{1}H–^{1}H COSY NMR spectrum of **8** in D_8-THF.

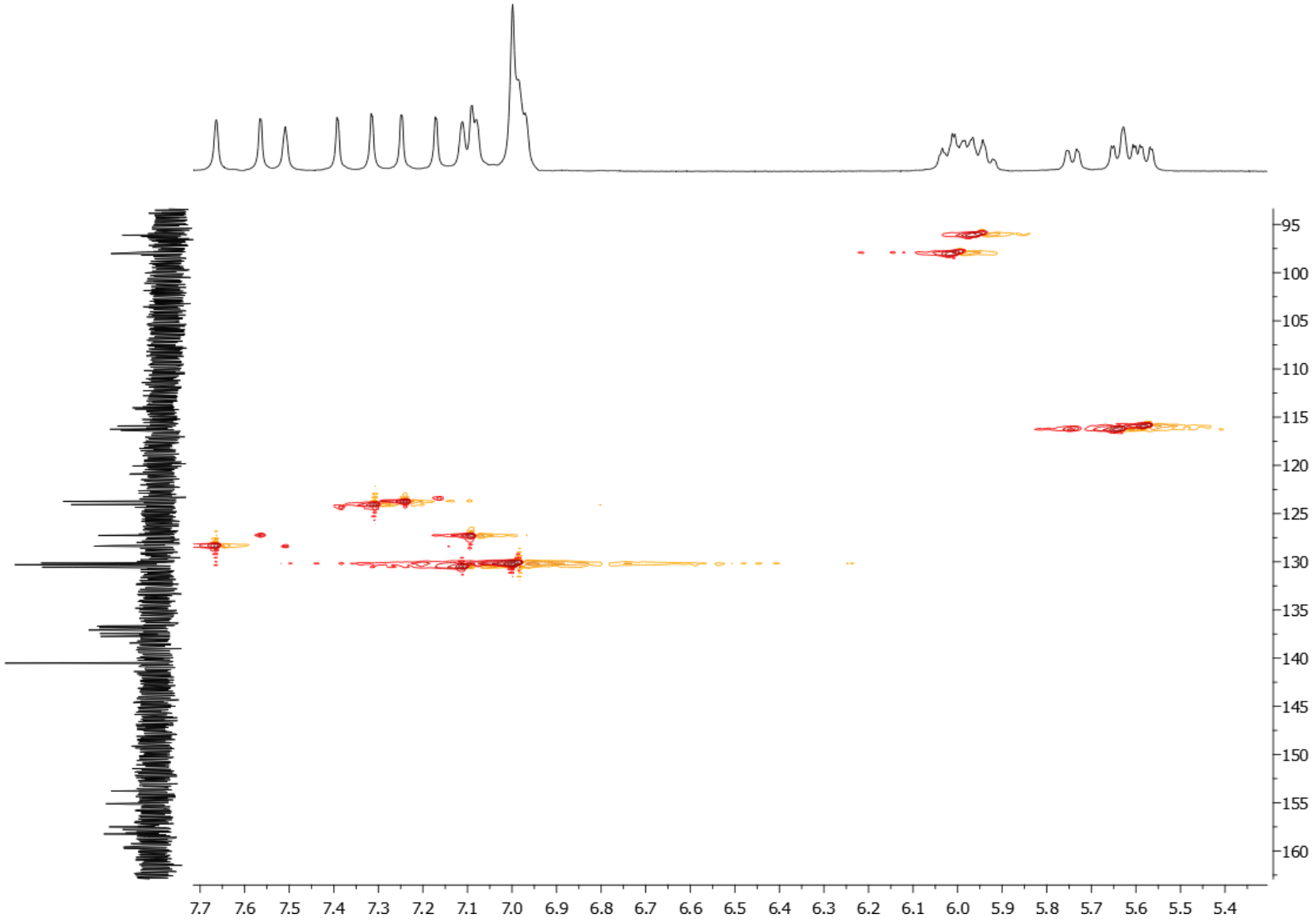

Spectrum S23. Expansion of the aromatic region of the ^{1}H–^{13}C HSQC NMR spectrum of **8** in D_8-THF.

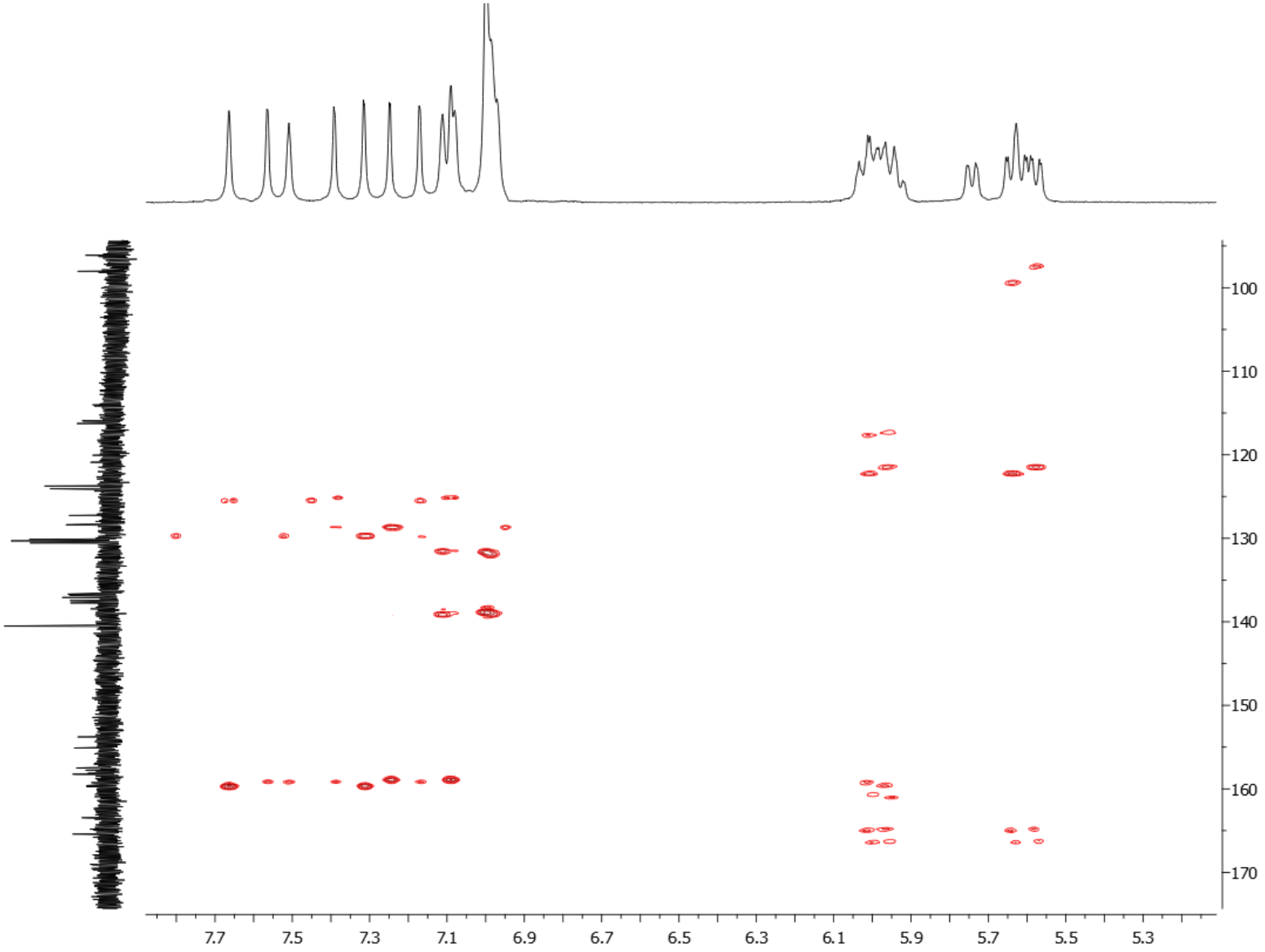

Spectrum S24. Expansion of the aromatic region of the ^{1}H–^{13}C HMBC NMR spectrum of **8** in D_8-THF.

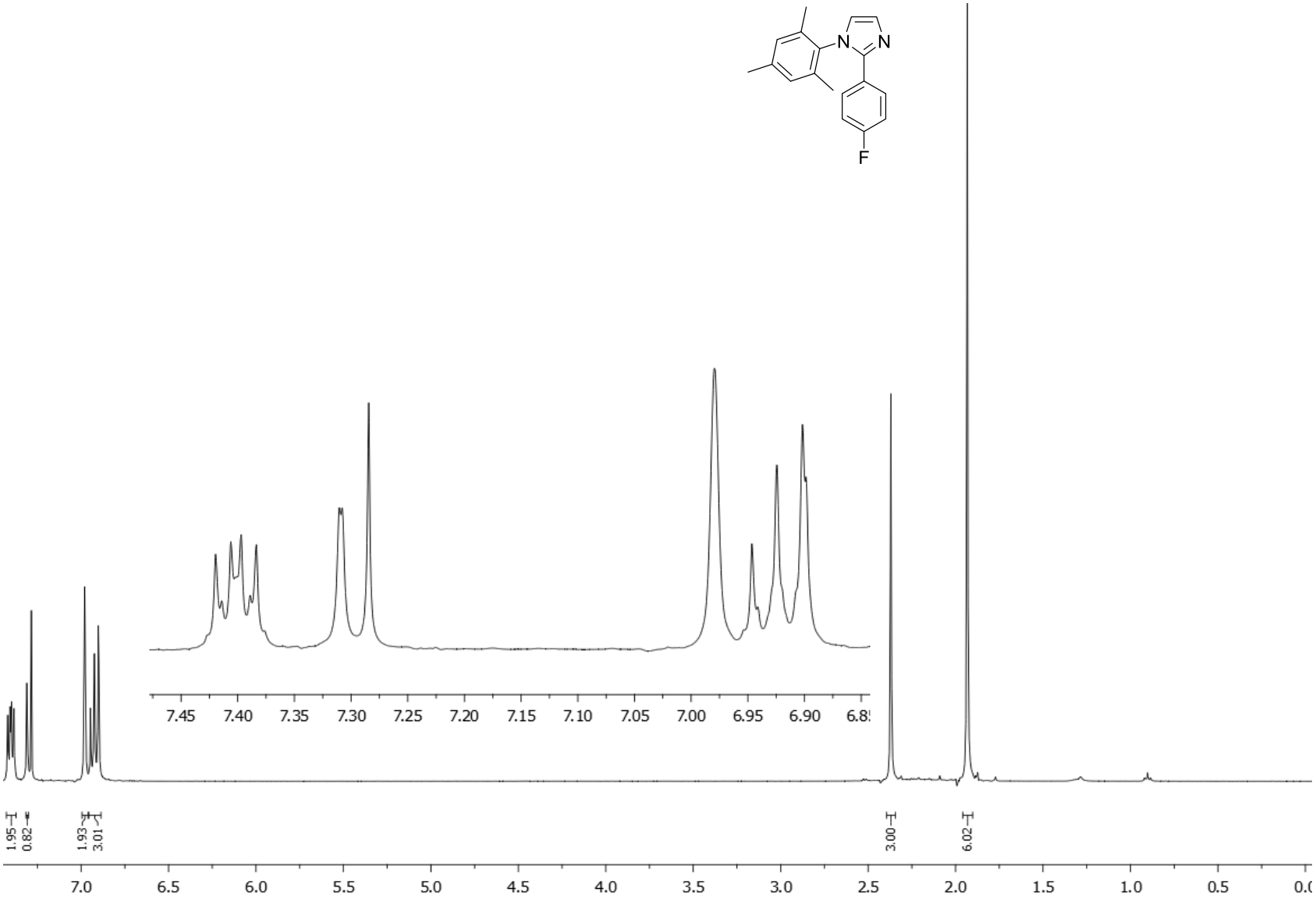

Spectrum S25. ^{1}H NMR spectrum (400 MHz) of H**10** in $CDCl_3$.

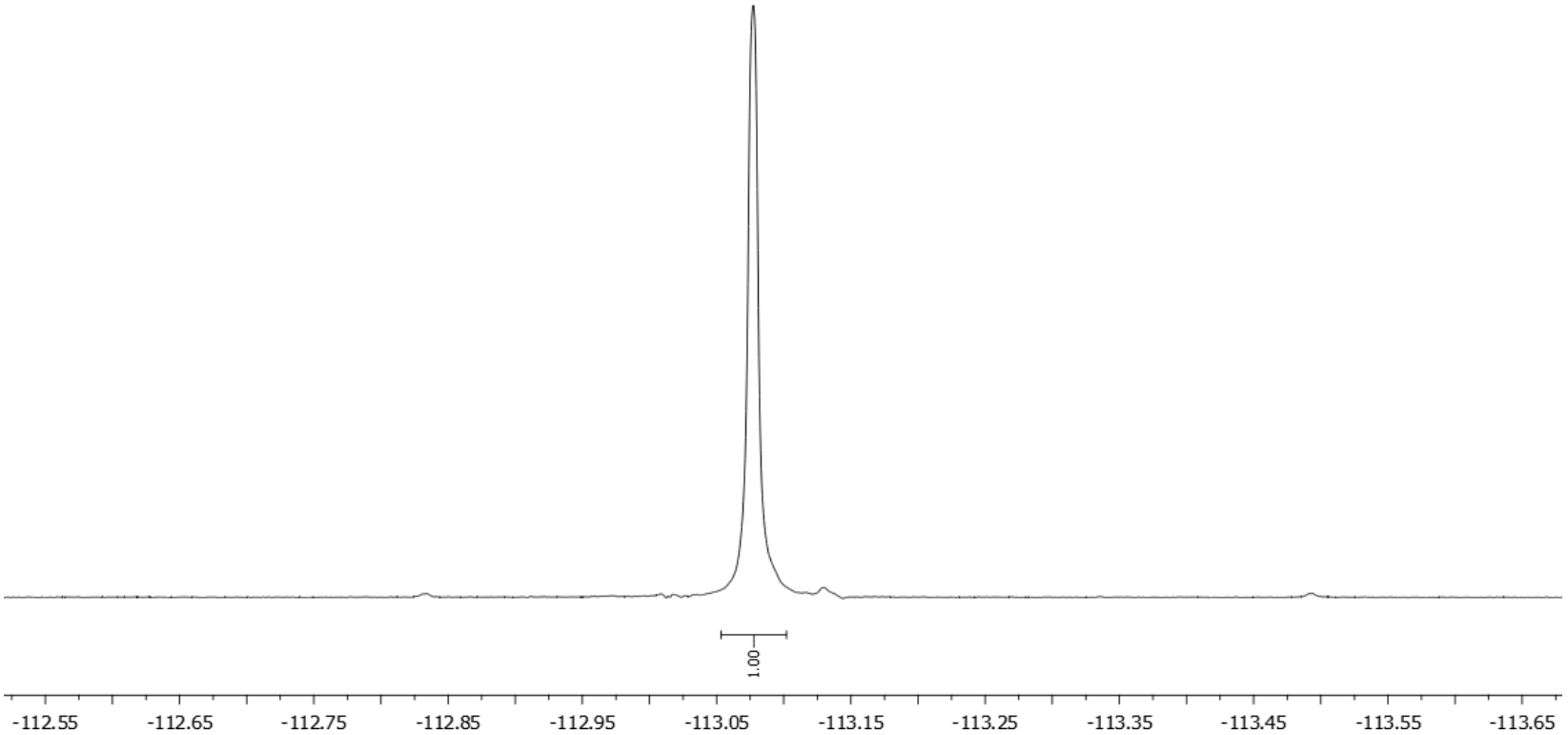

Spectrum S26. $^{19}F\{^{1}H\}$ NMR spectrum (376 MHz) of H**10** in $CDCl_3$.

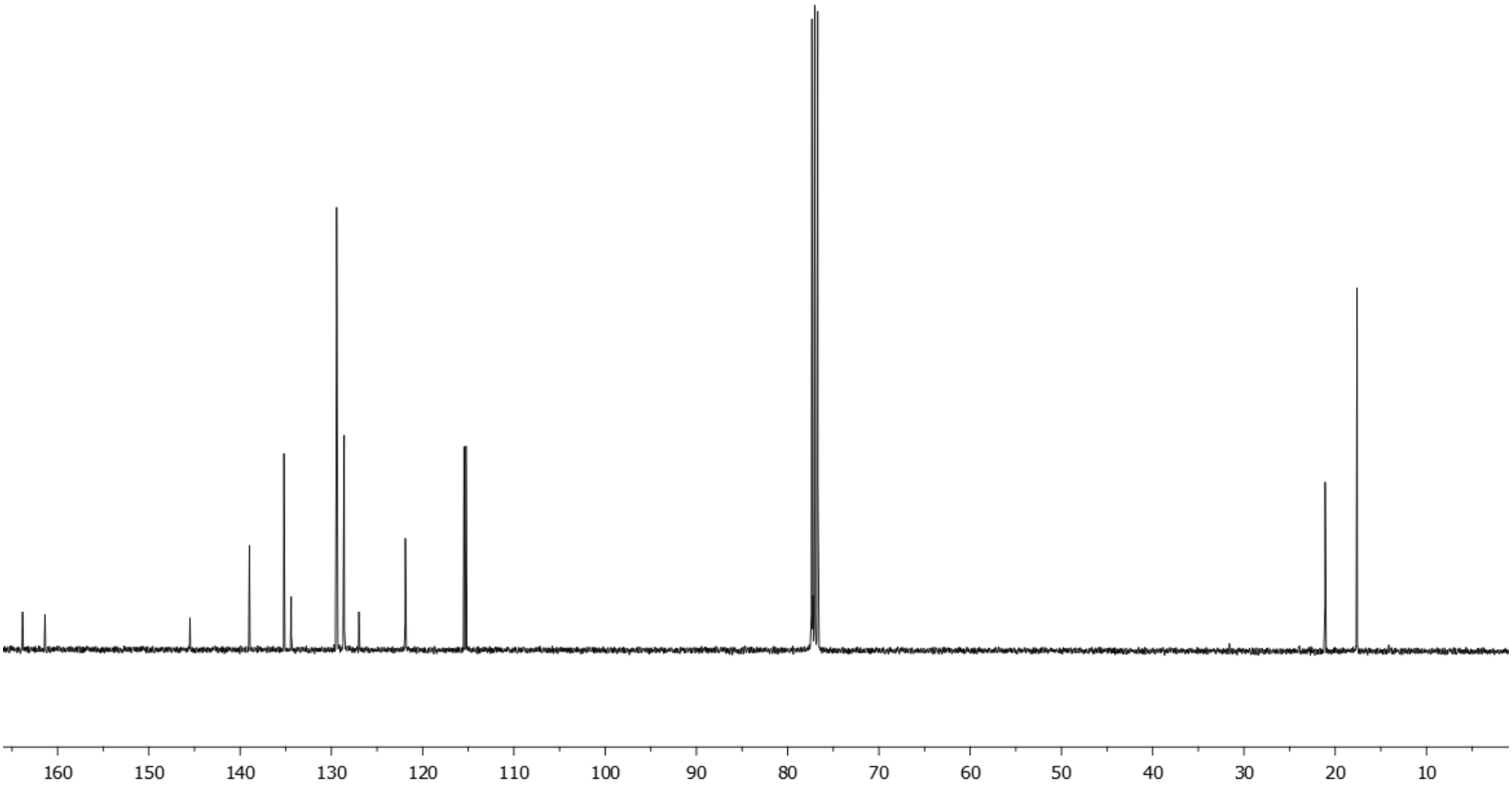

Spectrum S27. ^{13}C NMR spectrum (101 MHz) of H**10** in $CDCl_3$.

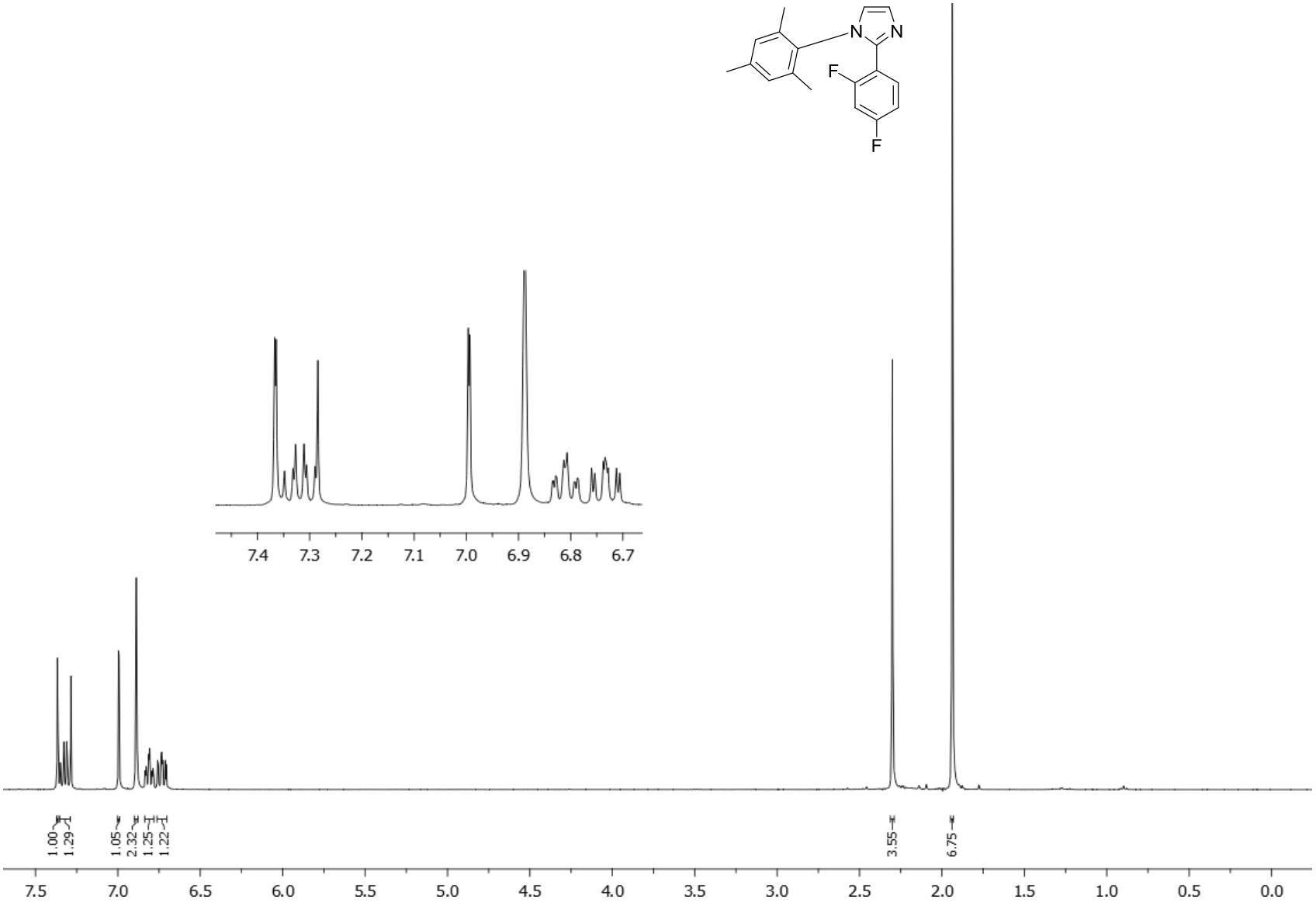

Spectrum S28. ^{1}H NMR spectrum (400 MHz) of H**11** in $CDCl_3$.

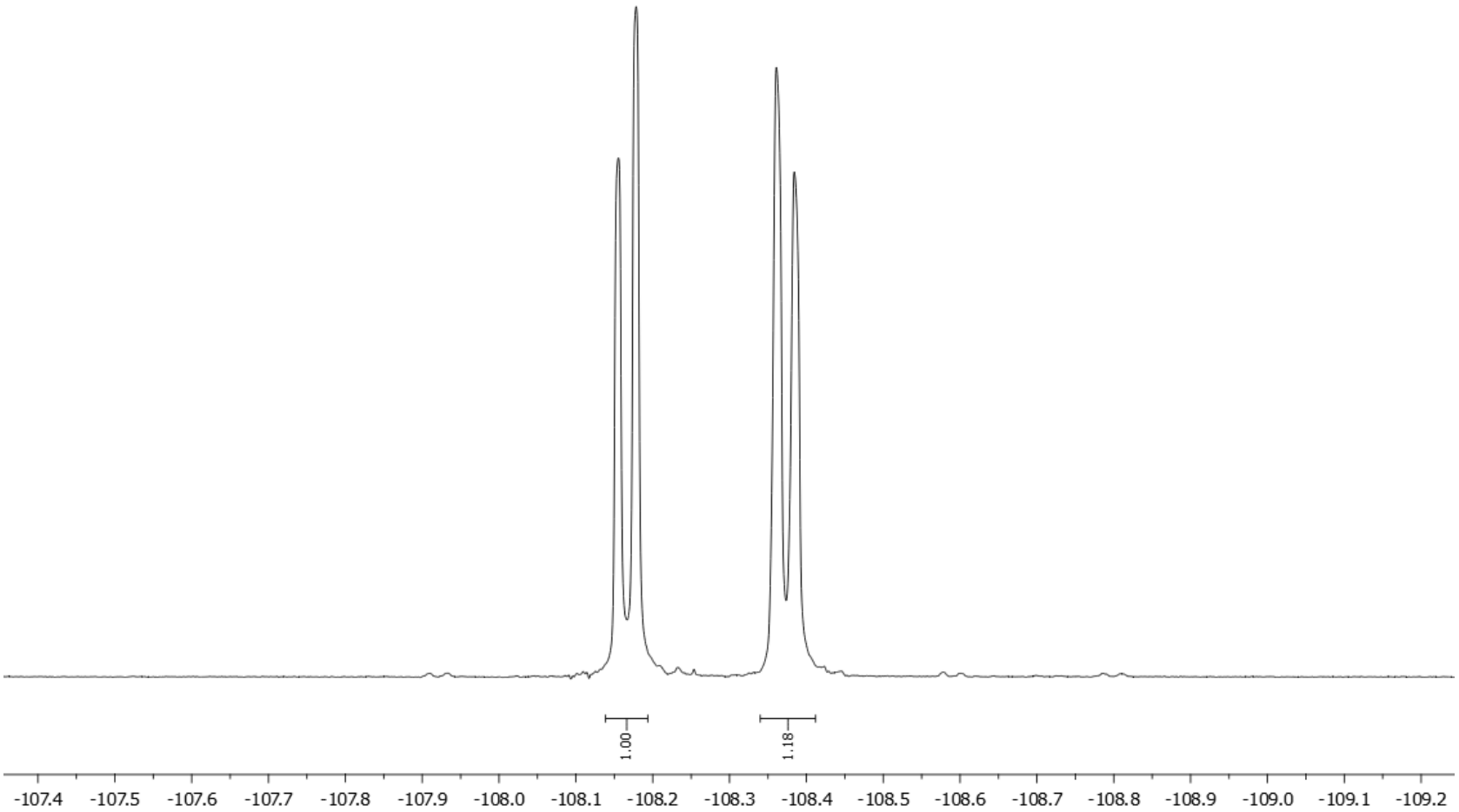

Spectrum S29. $^{19}F\{^{1}H\}$ NMR spectrum (376 MHz) of H**11** in $CDCl_3$.

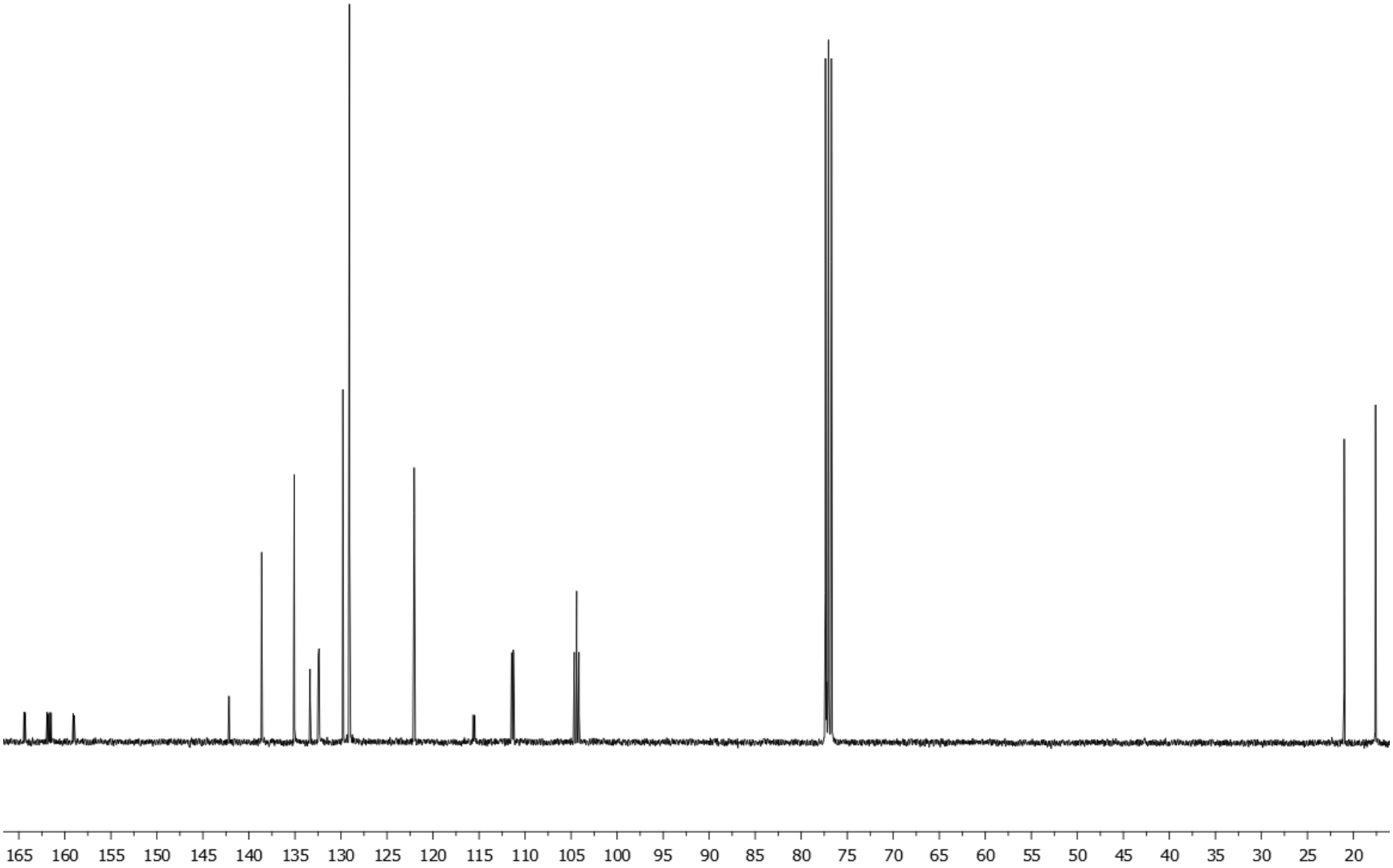

Spectrum S30. ^{13}C NMR spectrum (101 MHz) of H**11** in $CDCl_3$.

Electrochemistry

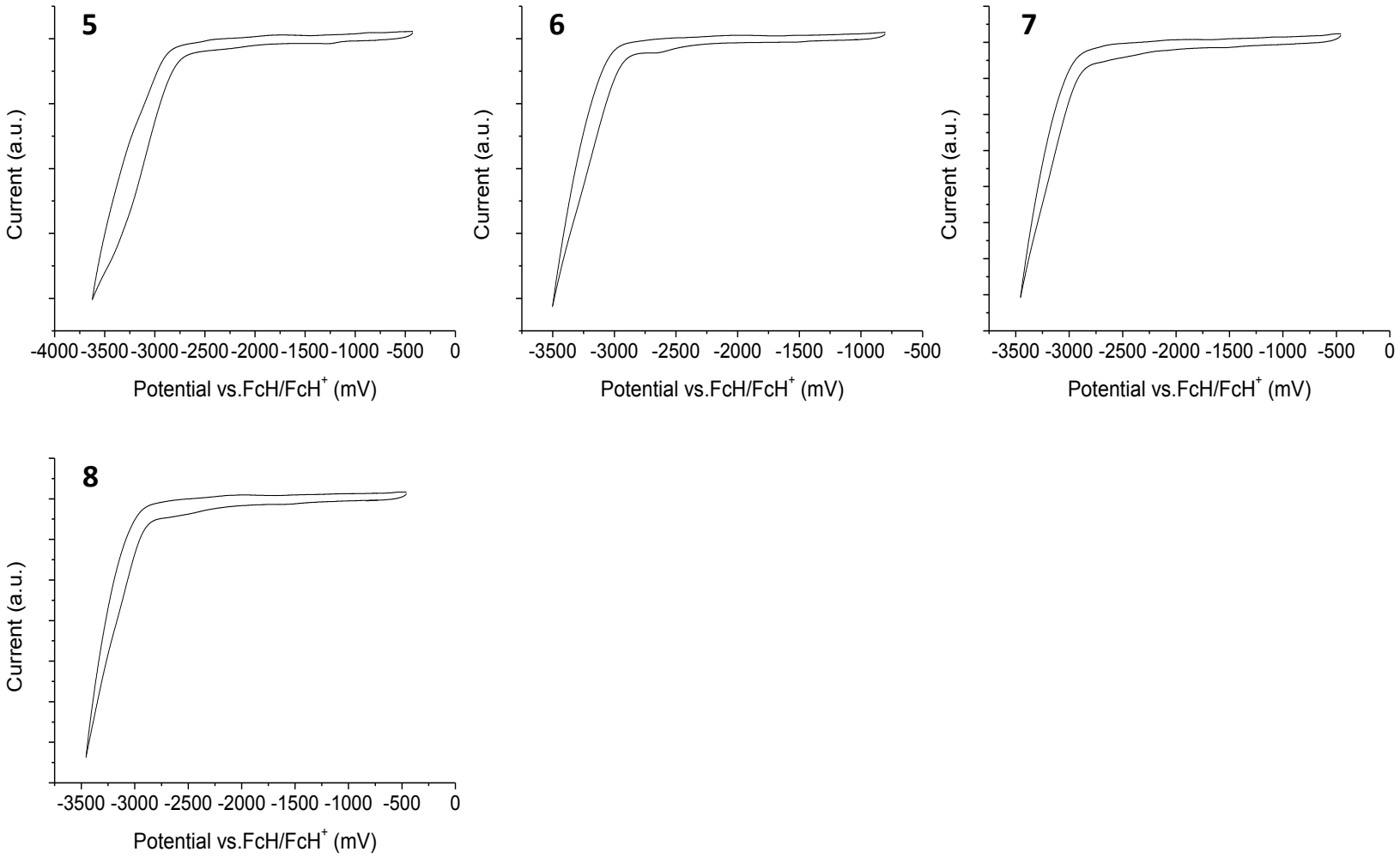

Figure S1. Cyclic voltammograms in 0.1 M *n*-Bu_4PF_6/ THF showing the reduction process for complexes **5**–**8.**

Photophysics

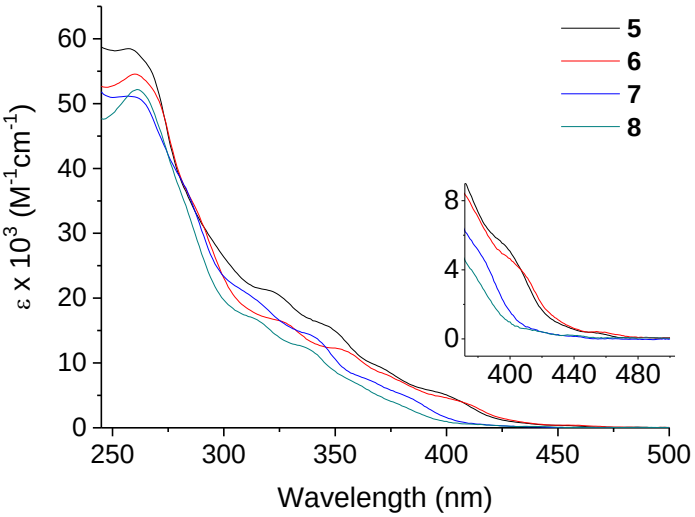

Figure S2. Absorption spectra for complexes **5**–**8** recorded in aerated DCM at room temperature.

Table S1. Tabulated absorption data for complexes **5**–**8** recorded in aerated DCM at room temperature.

Complex	λ_{abs} /nm ($\varepsilon \times 10^3$ / $M^{-1}cm^{-1}$)
5	258 (59), 288sh (34), 323 (21), 349 (16), 372 (9), 402 (5), 457 (0.3)
6	260 (55), 287sh (34), 327 (16), 355 (12), 378sh (7.6), 459 (0.4)
7	260 (51), 284sh (36), 315sh (20), 340 (14), 365sh (7.6), 384 (4.6), 442 (0.1)
8	261 (52), 283sh (33), 315 (17), 338 (12), 360sh (6.9), 379sh (3.4), 443 (0.2)

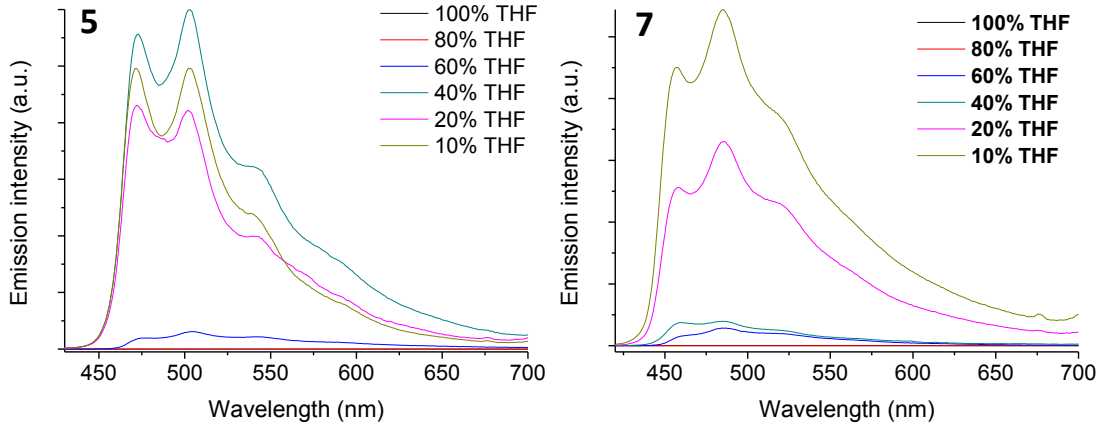

Figure S3. Emission spectra for THF solutions of complexes **5** and **7** upon incremental titration of water to induce precipitation (λ_{exc} 355 nm). THF fraction is percentage volume.

Computations

Table S2. Summary of the orbital contributions for complexes **5**–**7**.

Complex	Isomer	Orbital	Ir	Bridge centre	Ph[a]	Im[b]	Complex	Isomer	Orbital	Ir	Bridge centre	Bridge aryl	Ph[a]	Im[b]	Complex	Isomer	Orbital	Ir	Bridge centre	Bridge aryl	Ph[a]	Im[b]
5	*meso*	LUMO+5	3%	7%	35%	36%	**6**	*meso*	LUMO+5	1%	0%	10%	11%	13%	**7**	*meso*	LUMO+5	2%	1%	16%	26%	27%
		LUMO+4	0%	4%	4%	6%			LUMO+4	2%	1%	4%	29%	28%			LUMO+4	2%	1%	5%	36%	36%
		LUMO+3	1%	5%	4%	6%			LUMO+3	3%	3%	30%	34%	27%			LUMO+3	1%	1%	13%	45%	38%
		LUMO+2	3%	17%	28%	28%			LUMO+2	1%	1%	18%	42%	36%			LUMO+2	3%	2%	22%	38%	32%
		LUMO+1	3%	4%	43%	42%			LUMO+1	4%	2%	57%	19%	17%			LUMO+1	4%	3%	68%	13%	12%
		LUMO	3%	1%	49%	44%			LUMO	2%	7%	58%	17%	16%			LUMO	1%	9%	67%	11%	11%
		HOMO	45%	14%	33%	8%			HOMO	44%	41%	1%	7%	7%			HOMO	43%	43%	1%	6%	7%
		HOMO-1	47%	2%	40%	10%			HOMO-1	47%	7%	0%	37%	8%			HOMO-1	46%	5%	0%	38%	10%
		HOMO-2	48%	31%	13%	8%			HOMO-2	47%	2%	1%	40%	10%			HOMO-2	45%	2%	1%	38%	14%
		HOMO-3	63%	6%	18%	13%			HOMO-3	65%	7%	0%	14%	14%			HOMO-3	50%	4%	1%	23%	22%
		HOMO-4	45%	4%	28%	23%			HOMO-4	45%	4%	1%	25%	25%			HOMO-4	48%	5%	1%	27%	19%
		HOMO-5	43%	3%	29%	25%			HOMO-5	60%	5%	1%	16%	19%			HOMO-5	55%	5%	1%	20%	19%
	rac	LUMO+5	1%	0%	6%	94%		*rac*	LUMO+5	2%	2%	16%	25%	54%		*rac*	LUMO+5	3%	1%	5%	39%	36%
		LUMO+4	1%	1%	6%	93%			LUMO+4	2%	0%	6%	32%	59%			LUMO+4	2%	2%	9%	36%	35%
		LUMO+3	1%	0%	8%	92%			LUMO+3	2%	3%	40%	28%	26%			LUMO+3	3%	2%	24%	37%	31%
		LUMO+2	1%	1%	14%	84%			LUMO+2	3%	3%	74%	10%	11%			LUMO+2	2%	2%	4%	47%	41%
		LUMO+1	3%	1%	44%	52%			LUMO+1	2%	1%	1%	49%	46%			LUMO+1	3%	4%	78%	8%	7%
		LUMO	2%	1%	43%	53%			LUMO	2%	3%	50%	23%	22%			LUMO	1%	4%	67%	14%	13%
		HOMO	46%	34%	13%	7%			HOMO	44%	40%	1%	8%	7%			HOMO	43%	42%	1%	7%	7%
		HOMO-1	49%	4%	40%	8%			HOMO-1	50%	3%	0%	38%	8%			HOMO-1	48%	3%	0%	37%	11%
		HOMO-2	42%	13%	35%	10%			HOMO-2	44%	8%	0%	38%	10%			HOMO-2	41%	6%	0%	385	14%
		HOMO-3	64%	8%	14%	14%			HOMO-3	64%	9%	0%	13%	14%			HOMO-3	60%	8%	0%	16%	15%
		HOMO-4	40%	2%	31%	27%			HOMO-4	42%	2%	1%	28%	27%			HOMO-4	33%	2%	1%	35%	28%
		HOMO-5	61%	3%	19%	17%			HOMO-5	63%	2%	0%	17%	17%			HOMO-5	53%	2%	1%	26%	18%

[a]Phenyl moieties of the cyclometalating ligands. [b]Imidazole moieties of the cyclometalating ligands.

Table S3. Summary of the orbital contributions for complex **8**.

Complex	Isomer	Orbital	Ir	Bridge centre	Bridge aryl	Ph[a]	Im[b]
8	*meso*	LUMO+5	3%	1%	25%	36%	33%
		LUMO+4	4%	1%	1%	48%	44%
		LUMO+3	3%	3%	31%	34%	28%
		LUMO+2	1%	1%	18%	42%	36%
		LUMO+1	4%	2%	53%	21%	19%
		LUMO	2%	8%	56%	17%	17%
		HOMO	42%	45%	1%	5%	8%
		HOMO-1	47%	4%	0%	37%	11%
		HOMO-2	47%	3%	1%	35%	15%
		HOMO-3	47%	4%	1%	25%	24%
		HOMO-4	47%	5%	1%	27%	19%
		HOMO-5	49%	4%	1%	26%	20%
	rac	LUMO+5	3%	3%	22%	37%	33%
		LUMO+4	4%	1%	10%	45%	38%
		LUMO+3	4%	2%	14%	41%	37%
		LUMO+2	3%	2%	2%	48%	43%
		LUMO+1	3%	2%	70%	13%	12%
		LUMO	1%	4%	71%	12%	11%
		HOMO	43%	44%	1%	6%	6%
		HOMO-1	50%	3%	0%	35%	12%
		HOMO-2	41%	5%	1%	37%	17%
		HOMO-3	56%	8%	0%	21%	14%
		HOMO-4	33%	2%	1%	32%	32%
		HOMO-5	50%	2%	1%	31%	16%

[a]Phenyl moieties of the cyclometalating ligands. [b]Imidazole moieties of the cyclometalating ligands.

Table S4. Summary of the TD-DFT data for complexes **5** and **7**.

Transition	**5**				**7**			
	meso		*rac*		*meso*		*rac*	
	Main orbital contribution	**λ/ nm (ƒ)**	**Main orbital contribution**	**λ/ nm (ƒ)**	**Main orbital contribution**	**λ/ nm (ƒ)**	**Main orbital contribution**	**λ/ nm (ƒ)**
$S_0 \rightarrow T_1$	HOMO-2 → LUMO+6, HOMO-2 → LUMO+8	458	HOMO → LUMO+8	460	HOMO → LUMO	424	HOMO-1 → LUMO+3, HOMO → LUMO+2	415
$S_0 \rightarrow T_2$	HOMO → LUMO+1	425	HOMO-1 → LUMO+1, HOMO → LUMO	425	HOMO → LUMO+1, HOMO-2 → LUMO+2	415	HOMO-1 → LUMO+2, HOMO → LUMO+3	415
$S_0 \rightarrow T_3$	HOMO-1 → LUMO	422	HOMO-1 → LUMO, HOMO → LUMO+1	425	HOMO-2 → LUMO+3, HOMO → LUMO+2	404	HOMO → LUMO+1, HOMO → LUMO+16	411
$S_0 \rightarrow T_4$	HOMO → LUMO+5, HOMO → LUMO+8	417	HOMO-1 → LUMO+2	416	HOMO-2 → LUMO+3, HOMO-1 → LUMO+4	406	HOMO-1 → LUMO+2, HOMO-1 → LUMO+4	407
$S_0 \rightarrow T_5$	HOMO-1 → LUMO+2	414	HOMO-2 → LUMO+2, HOMO-1 → LUMO+7	416	HOMO-2 → LUMO+4, HOMO-1 → LUMO+3	406	HOMO-2 → LUMO+2, HOMO-1 → LUMO+5	407

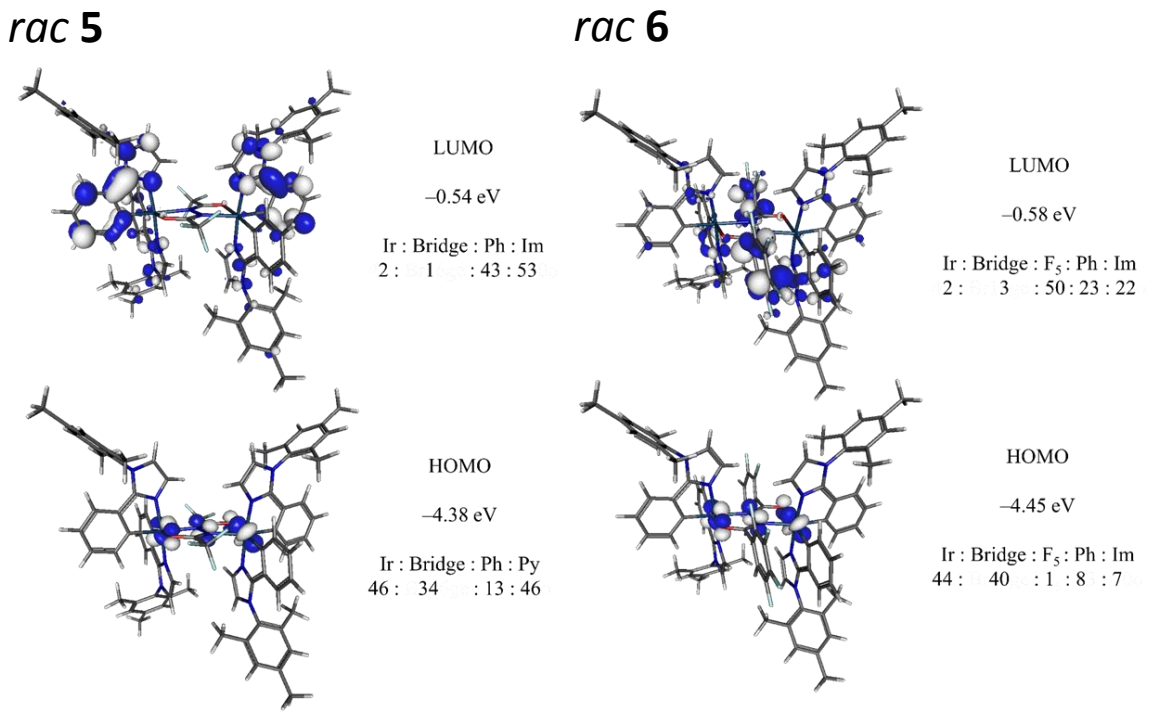

Figure S4. Frontier molecular orbitals for the most stable minima of *rac* **5** and *rac* **6**.

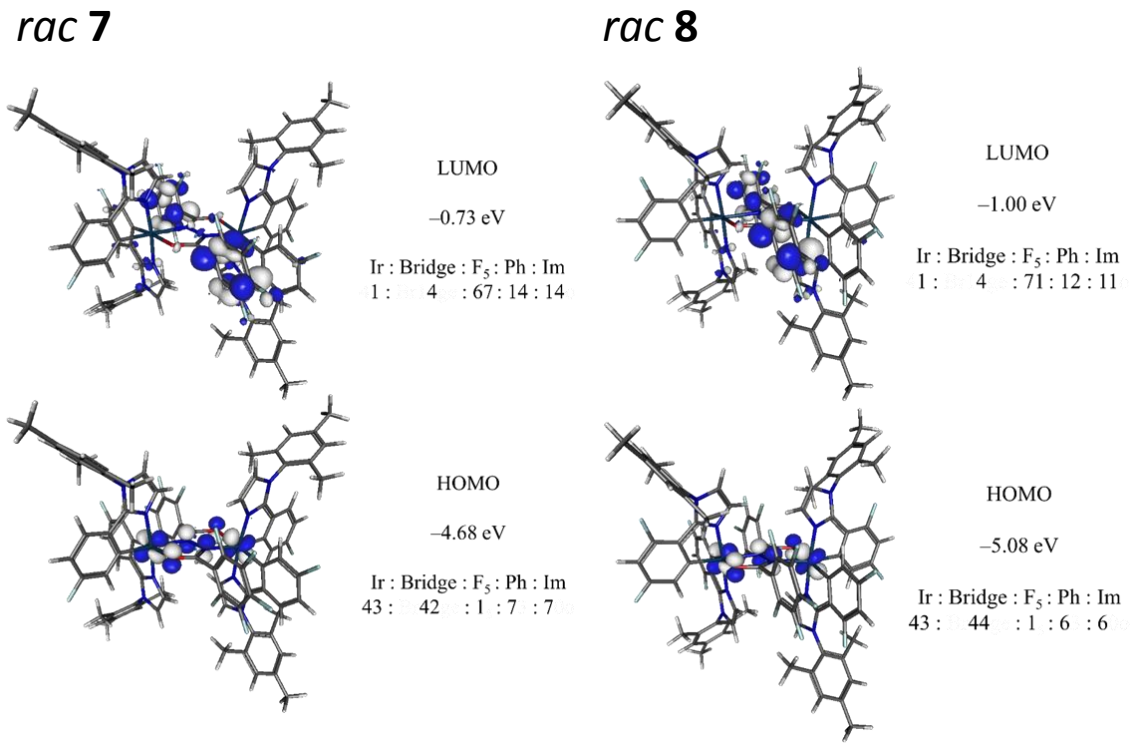

Figure S5. Frontier molecular orbitals for the most stable minima of *rac* **7** and *rac* **8**

Thermal Analysis

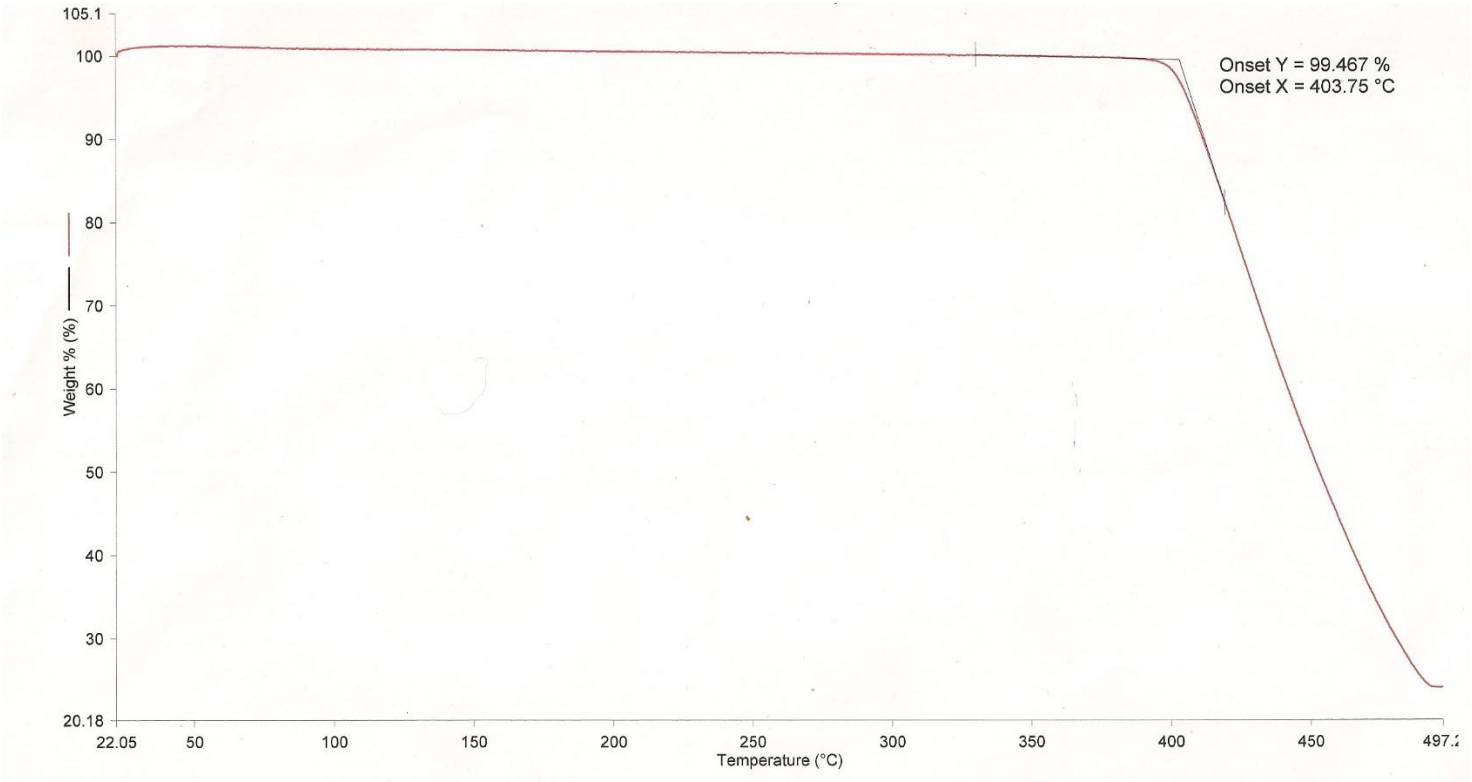

Figure S6.TGA trace for complex **5**. Onset = 404 °C

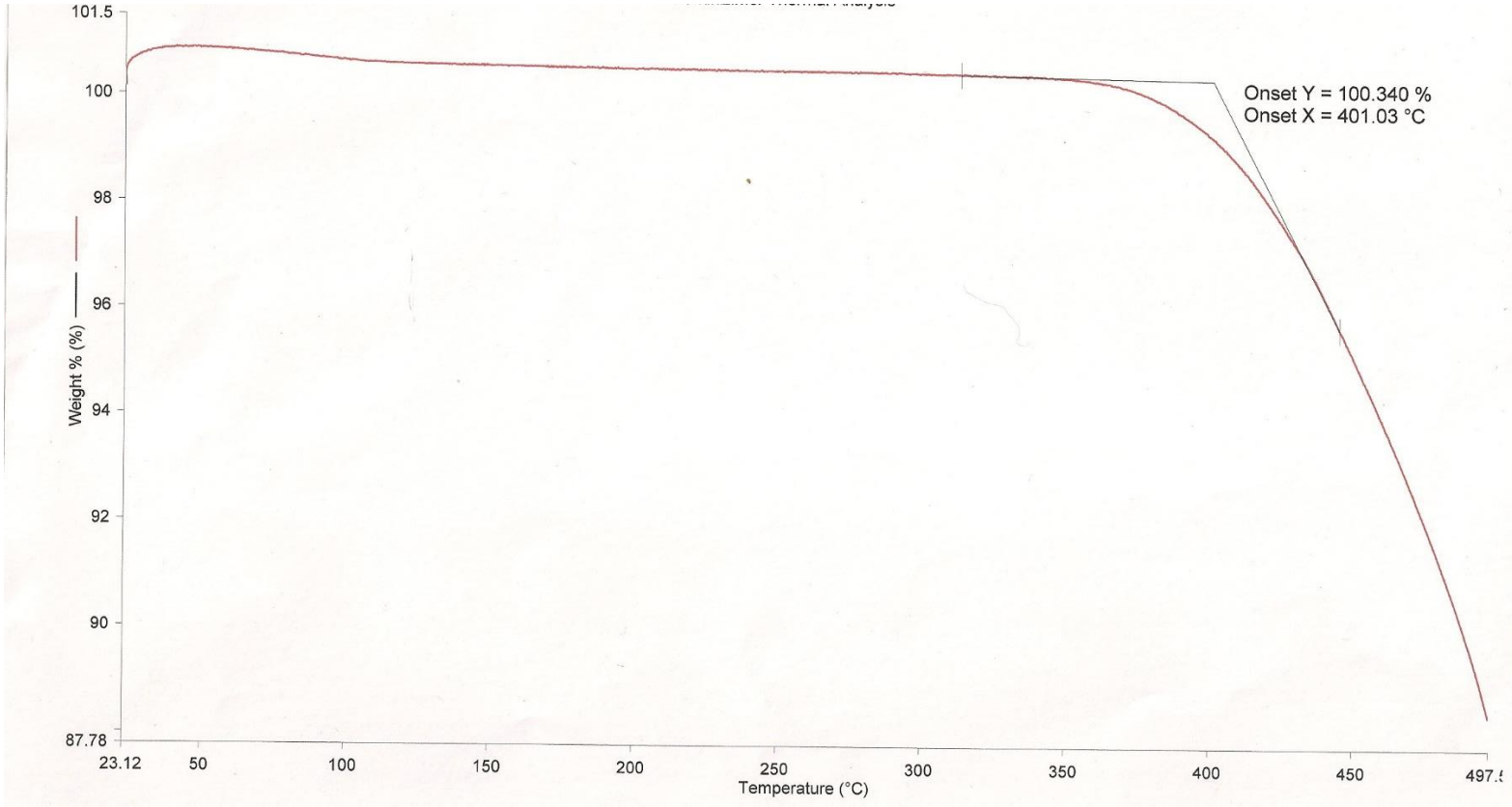

Figure S7.TGA trace for complex **6**. Onset = 401 °C

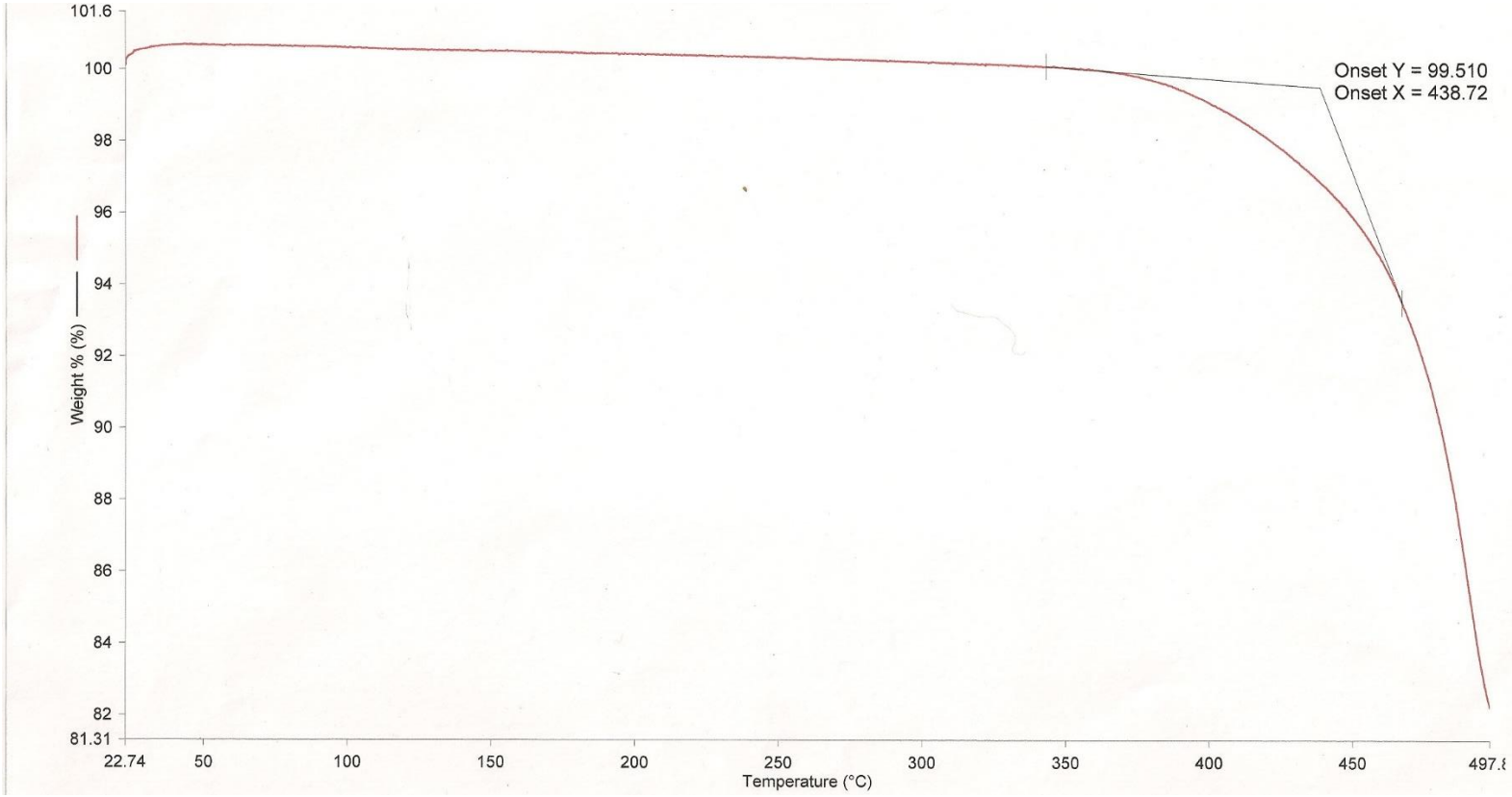

Figure S8.TGA trace for complex **7**. Onset = 439 °C

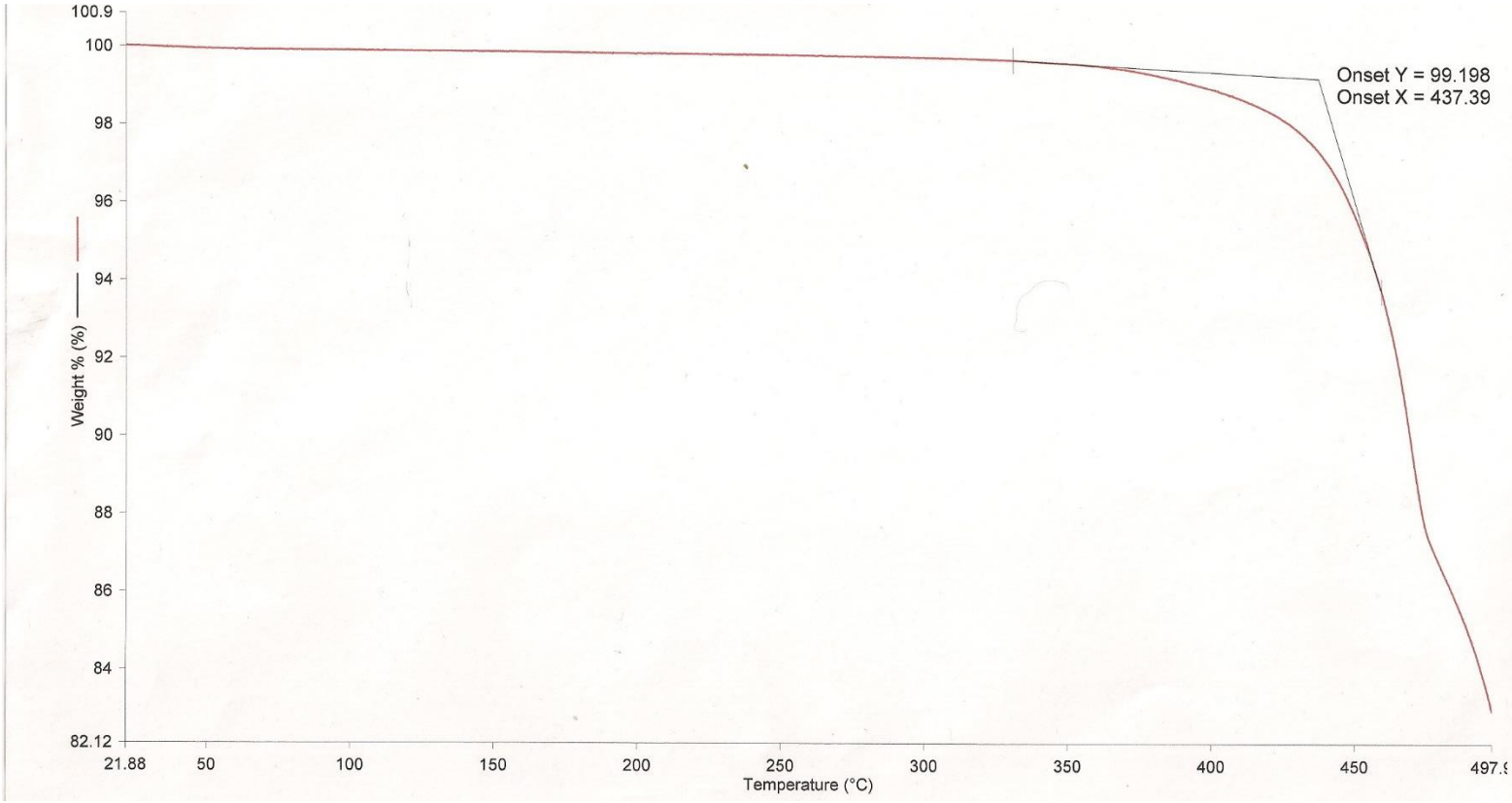

Figure S9.TGA trace for complex **8**. Onset = 437 °C.

X-ray crystallography

Table S5. Crystal data

Compound	*meso*-**7**	*meso*-**8**
CCDC dep. no.	1871136	1871137
Formula	$C_{86}H_{64}F_{14}Ir_2N_{10}O_2 \cdot 6CH_2Cl_2$	$C_{86}H_{60}F_{18}Ir_2N_{10}O_2 \cdot 2MeOH$
$D_{calc.}$/ g cm^{-3}	1.706	1.687
μ/mm^{-1}	3.232	3.385
Formula Weight	2429.42	2055.92
Size/mm^3	0.25×0.07×0.06	0.44×0.25×0.12
T/K	120	120
Crystal System	monoclinic	orthorhombic
Space Group	*C*2/*c* (no. 15)	*Pbca* (no. 61)
a/Å	24.2045(10)	20.0605(10)
b/Å	14.8901(6)	13.1557(6)
c/Å	27.9788(12)	30.6755(15)
β/°	110.265(2)	90
V/Å^3	9459.6(7)	8095.6(7)
Z	4	4
Θ_{max}/°	30.000	32.575
Measured reflections	101919	175372
Unique reflections	13754	14709
Reflections with $I > 2\sigma(I)$	11072	11317
R_{int}	0.0520	0.0536
Parameters	616	576
Residual Δρ, eÅ^{-3}	3.04, -1.45	3.66, -1.60
R_1,wR_2 [$I > 2\sigma(I)$]	0.0424, 0.1035	0.0378, 0.0738
R_1, wR_2 (all data)	0.0612, 0.1125	0.0610, 0.0813
Goodness of fit	1.079	1.077

References

1 A. Fürstner, M. Alcarazo, V. César and C. W. Lehmann, *Chem. Commun.*, 2006, 2176–2178.
2 D. G. Congrave, Y.-T. Hsu, A. S. Batsanov, A. Beeby and M. R. Bryce, *Dalton Trans.*, 2018, **47**, 2086–2098.
3 Gaussian 09, Revision A.02, M. J. Frisch, G. W. Trucks, H. B. Schlegel, G. E. Scuseria, M. A. Robb, J. R. Cheeseman, G. Scalmani, V. Barone, B. Mennucci, G. A. Petersson, H. Nakatsuji, M. Caricato, X. Li, H. P. Hratchian, A. F. Izmaylov, J. Bloino, G. Zheng, J. L. Sonnenberg, M. Hada, M. Ehara, K. Toyota, R. Fukuda, J. Hasegawa, M. Ishida, T. Nakajima, Y. Honda, O. Kitao, H. Nakai, T. Vreven, J. A. Montgomery, Jr., J. E. Peralta, F. Ogliaro, M. Bearpark, J. J. Heyd, E. Brothers, K. N. Kudin, V. N. Staroverov, R. Kobayashi, J. Normand, K. Raghavachari, A. Rendell, J. C. Burant, S. S. Iyengar, J. Tomasi, M. Cossi, N. Rega, J. M. Millam, M. Klene, J. E. Knox, J. B. Cross, V. Bakken, C. Adamo, J. Jaramillo, R. Gomperts, R. E. Stratmann, O. Yazyev, A. J. Austin, R. Cammi, C. Pomelli, J. W. Ochterski, R. L. Martin, K. Morokuma, V. G. Zakrzewski, G. A. Voth, P. Salvador, J. J. Dannenberg, S. Dapprich, A. D. Daniels, O. Farkas, J. B. Foresman, J. V. Ortiz, J. Cioslowski, D. J. Fox, Gaussian, Inc., Wallingford CT, 2009.
4 A. D. Becke, *J. Chem. Phys.*, 1993, **98**, 5648.
5 C. Lee, W. Yang and R. G. Parr, *Phys. Rev. B*, 1988, **37**, 785–789.
6 P. J. Hay and W. R. Wadt, *J. Chem. Phys.*, 1985, **82**, 270–283.
7 W. R. Wadt and P. J. Hay, *J. Chem. Phys.*, 1985, **82**, 284–298.
8 P. J. Hay and W. R. Wadt, *J. Chem. Phys.*, 1985, **82**, 293–310.
9 G. A. Petersson, A. Bennett, T. G. Tensfeldt, M. A. Al-Laham, W. A. Shirley and J. Mantzaris, *J. Chem. Phys.*, 1991, **94**, 6081–6090.
10 J. Melorose, R. Perroy and S. Careas, *J. Chem. Phys.*, 1988, **89**, 2193–2218.
11 A.-R. Allouche, *J. Comput. Chem.*, 2011, **32**, 174–182.
12 N. M. O'Boyle, A. L. Tenderholt and K. M. Langner, *J. Comput. Chem.*, 2008, **29**, 839–845.
13 L. Krause, R. Herbst-Irmer, G. M. Sheldrick and D. Stalke, *J. Appl. Crystallogr.*, 2015, **48**, 3–10.
14 G. M. Sheldrick, *Acta Crystallogr. A*, 2008, **A64**, 112–122.
15 G. M. Sheldrick, *Acta Crystallogr. C*, 2015, **71**, 3–8.
16 L. J. Bourhis, O. V Dolomanov, R. J. Gildea, J. A. K. Howard and H. Puschmann, *Acta Crystallogr.*, 2015, **A71**, 7–13.
17 H. Benjamin, Y. Zheng, A. S. Batsanov, M. A. Fox, H. A. Al-Attar, A. P. Monkman and M. R. Bryce, *Inorg. Chem.*, 2016, **55**, 8612–8627.
18 R. Davidson, Y.-T. Hsu, T. Batchelor, D. Yufit and A. Beeby, *Dalton Trans.*, 2016, **45**, 11496–11507.
19 L-O. Pålsson and A. P. Monkman, *Adv. Mater.*, 2002, **14**, 757–758.
20 M. Micksch, M. Tenne and T. Strassner, *Eur. J. Org. Chem.*, 2013, 6137–6145.